A Synchrotron for Polar Molecules

by
Peter Christian Zieger

A Synchrotron for Polar Molecules

Proefschrift

ter verkrijging van de graad van doctor
aan de Radboud Universiteit Nijmegen,
op gezag van de rector magnificus prof. mr. S.C.J.J. Kortmann,
volgens besluit van het college van decanen
in het openbaar te verdedigen
op vrijdag 7 december 2012
om 13:30 uur precies

door

Peter Christian Zieger

geboren op 4 april 1982
te Leipzig, Duitsland

A Synchrotron for Polar Molecules

Doctoral Thesis

to obtain the degree of doctor
from Radboud University Nijmegen
on the authority of the rector Magnificus
prof. dr. S.C.J.J. Kortmann,
according to the decision of the Council of Deans
to be defended in public
on Friday, 7 December, 2012
at 13:30 hours

by

Peter Christian Zieger

born on 4 April 1982
in Leipzig, Germany

Contents

Chapter 1

Introduction

The aim of systematic scientific research within the field of physics is to understand the fundamental nature of matter. Since the days of Antoine Lavoisier, who proclaimed that during the combustion of a substance it associates with oxygen, it is accepted that matter consists of molecules and that a molecule itself consists of an arrangement of atoms. Lavoisier can be seen as the discoverer and founder of modern molecular physics. Since those days, the field of modern chemistry/molecular physics has steadily progressed. Scientific problems are raised, studied and solved, while a deeper understanding is gained. New knowledge often results in useful applications, but even more often raises new questions that draw the attention of scientists. The Austrian author and scientist Adolf Pichler describes the complexity of research at the end of the 19$^{\text{th}}$ century with the famous quote "Die Forschung ist immer auf dem Wege, nie am Ziel" (Research is always on its way; never at the end). This thesis describes a synchrotron for polar molecules. It demonstrates the level of control that can nowadays be achieved over molecules; multiple packets of neutral molecules are made to revolve clockwise and anti-clockwise for more than 1000 times in a tabletop storage ring, thereby traveling a distance of over one mile. In the spirit of Pichler, this achievement opens a new area of research; the study of collisions between counter-propagating packets of molecules at extremely low and well-defined collision energies.

Detailed knowledge concerning the structure of molecules has been obtained by (i) studying the interaction between molecules and light (spectroscopy) and (ii) by studying collisions of molecules with atoms or other molecules. Gas phase molecules offer an unique opportunity: Because the relative distance to the next particle is large, the molecule can be treated as an isolated system. The resolution that can be achieved in an experiment is directly related to how well the experimental conditions – *i.e.*, the position, velocity and internal state of the molecule – are controlled. As the range of velocities in an ensemble of molecules is described by their temperature, minimizing the relative motion of molecules is equivalent to lowering the temperature of the molecules. In the studies conducted for this thesis, the packets of molecules have a temperature of a few milliKelvin.

Over the last decades astonishing results were achieved in the field of cold atoms. Using laser cooling, atomic clouds with temperatures below $100\,\mu\text{K}$ are routinely achieved in many labs throughout the world. Laser cooling requires a relatively simple energy structure allowing one to cycle a transition many times. In this process, the momentum of the absorbed light is used to cool the atoms. Unfortunately, the complex energy structure

of molecules, with their additional vibrational and rotational degrees of freedom, makes it (almost [1]) impossible to implement laser cooling of molecules. Since the mid-1990s two different methods to produce cold molecules have been established. In the first (indirect) method, cold molecules are produced by associating two ultra cold atoms. In the second (direct) method, preexisting molecules are cooled using either cryogenic methods [2] or by making a supersonic expansion and subsequently decelerating these molecules using electric, magnetic or electromagnetic fields [3]. In this thesis cold molecular beams are generated using the latter technique.

A supersonic expansion is formed by releasing a high pressure gas of molecules into vacuum. In this process, heat is converted into forward velocity of the molecules, *i.e.*, the mean velocity of the molecules increases but the velocity spread becomes smaller, as does the rotational and vibrational energy of the molecules. The lower temperature threshold of the beam is limited by the onset of clustering. By seeding the molecule of interest in a noble gas, however, translational temperatures below 1 K have been achieved, while the rotational and vibrational temperatures are typically around 5 and 50 K, respectively. The cooling of all degrees of freedom of molecules in supersonic expansions has greatly reduced the complexity in molecular spectra and has thereby revolutionized molecular spectroscopy [4].

Although the molecules in a supersonic beam are cold in the moving frame, their forward velocity is typically within the range of 300-2000 m/s. During the last decade, time-dependent electric, magnetic or radiative fields have been used to lower the forward velocity of molecules in beams. The technique of deceleration with time-dependent electric fields was first demonstrated by Bethlem *et al.* in 1999. They showed that neutral polar CO molecules with a velocity of 225 m/s could be decelerated to 98 m/s by utilization of the Stark effect [5]. Hence, this deceleration technique is called 'Stark deceleration'. In 2000, Stark deceleration was used to bring ammonia molecules to a standstill and to subsequently trap them in a electrostatic trap [6]. Similarly, atoms and molecules with a magnetic dipole moment can be manipulated using magnetic fields. Zeeman deceleration was first demonstrated on a beam of H-atoms by Vanhaecke *et al.* [7] and applied to a beam of oxygen molecules by Narevicius *et al.* [8]. Other techniques to decelerate molecular beams have been and are still being developed. For a review of these techniques see for instance [9, 10].

As mentioned earlier, the ability to control the motion and internal state of molecules is advantageous for a number of fundamental studies. Spectroscopic studies are ultimately limited by the interaction time of the molecule of interest with the light used to probe the molecule. In conventional molecular beam experiments, this interaction time is typically below one hundred microseconds. Slow (or potentially trapped) molecules can significantly increase the possible interaction time, allowing higher precision measurements to be conducted. Stark-decelerated molecular beams were used to perform high-resolution microwave spectroscopy on ammonia [11] and OH [12]. Currently, a number of groups are working on using cold molecules for testing the time-variation of the proton-to-electron mass ratio [13] and for measuring the electric dipole moment of the electron [14].

The ability to control the energy and energy spread of a molecular beam with electric

and magnetic fields enables scattering experiments to be conducted that probe molecular interaction potentials in great detail. A holy grail of this research is to be able to observe resonances within the collision cross section as a function of collision energy. These resonances occur when kinetic energy is converted into rotational energy as a result of the anisotropy of the potential energy surface (PES) of the two collision partners; the width of the resonances is determined by the lifetime of this collision complex. For instance, theoretical calculations have predicted strong and sharp resonances for CO colliding with He [15]. The velocity spread of a Stark-decelerated beam is in principle sufficiently small to resolve this resonant structure. Another motivation for research into cold collisions is the fact that at low temperatures the collision process becomes sensitive to externally applied electric or magnetic fields. This gives a handle to control and steer the outcome of a chemical reaction [16, 17]. In 2006, Gilijamse *et al.* performed the first scattering experiment using a Stark-decelerated molecular beam [18]. In this experiment, OH radicals were scattered with a conventional beam of Xe atoms in a crossed molecular beam geometry. The total collision energy is changed by varying the velocity of the OH radicals, while the velocity of the rare gas beam is kept fixed. Subsequently, collisions of OH radicals with other rare gas atoms have been studied extensively, determining accurately the threshold behaviors of the state-to-state inelastic scattering cross sections [19, 20]. Recently, experiments have been conducted using collisions between Stark-decelerated OH molecules and a state-selected beam of NO molecules [21]. Ultimately, one would like to study collisions between two velocity controlled molecular beams to resolve these resonances. In order to achieve this, one aims for molecular beams that are fully controlled, *i.e.*, in a single quantum state and with a controlled absolute velocity and velocity spread. Thus far, the densities achieved have been insufficient for such experiments.

This thesis describes the demonstration and characterization of a synchrotron for polar molecules. Although this synchrotron is useful for many studies, this thesis will mainly focus on its use for studying collisions between counter-propagating packets of cold molecules. The obvious advantage of a ring structure is that a stored packet of molecules revolving around the ring will repeatedly encounter counter-propagating packets. By storing many packets over an extended time, the sensitivity for detecting collisions increases by orders of magnitude compared to an experiment where the collision partners encounter each other only once. In Chapter 7 measurements will be presented demonstrating the simultaneous trapping of 13 packets revolving in both directions. A packet that has completed $64\frac{1}{4}$ round trips (see Figure 7.3) will have had 1670 encounters with packets revolving in the opposite direction.

Confining Molecules in a Storage Ring   The molecular storage ring described in this thesis is the third generation storage ring for polar molecules built in our laboratory. The first and second generation storage rings are schematically shown in Figure 1.1. The top left Panel of Figure 1.1 shows a storage ring that is obtained by bending a linear hexapole focuser into the shape of a torus, as demonstrated by F. M. H. Crompvoets and coworkers [24]. In this prototype storage ring, the molecules are transversely confined

A Storage Ring for Neutral Molecules · · · A Molecular Synchrotron
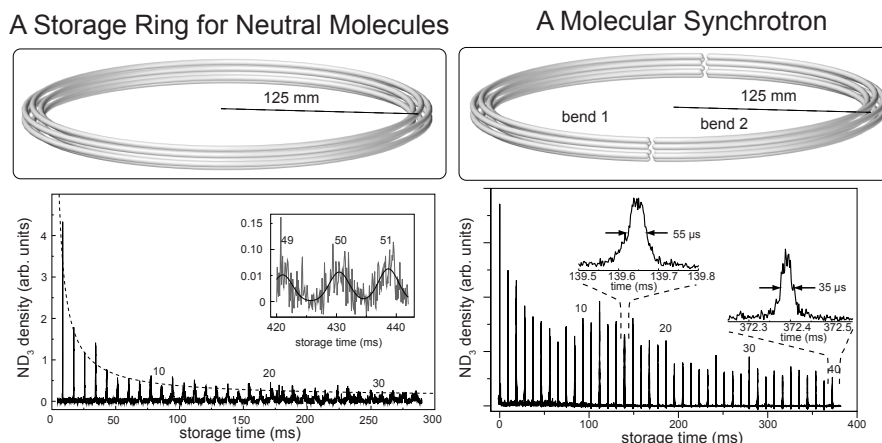
Figure 1.1: The two predecessors of the present molecular synchrotron. The top left Panel shows a photo realistic image of the first prototype of a storage ring for neutral molecules. It consists of a hexapole guide bent into a circle. The radius is 125 mm. Underneath the ND_3 intensity is shown at the loading position as a function of storage time (reproduced from [22]). To guide the eye, the dashed line indicates a $1/e$ decay. The inset shows the ammonia intensity for the 49th to the 51st round trips. The molecular packet is confined in the transversal direction but due to the lack of longitudinal confinement the packet spreads out in the forward direction.
The top right Panel shows the second generation of a molecular storage ring: the prototype molecular synchrotron. The hexapole torus has the same dimension but this time it consists of two hexapole half rings. The two gaps are 2 mm wide. The measurement underneath shows the ND_3 intensity as a function of storage time (reproduced from [23]). Here, due to the applied switching scheme, the molecular packet is confined as a tight bunch in an effective three dimensional potential well.

but are essentially free along the longitudinal direction, *i.e.*, along the circle. The lower left Panel of Figure 1.1 shows a measurement of the ND_3 density at the detection point in the ring as a function of storage time. For long storage times the spatial width of the packet gradually increases until, eventually, the molecules fill the entire ring.

After the successful implementation of this first storage ring, C. E. Heiner and coworkers demonstrated a sectioned storage ring consisting of two hexapoles bent into a semicircle with a radius of 125 mm, separated by a 2 mm gap [23]. By switching the electric field synchronously with the motion of the molecules, the electric fields in the gap are used to keep the molecular packet confined in the longitudinal direction. A photo realistic image of this molecular synchrotron is shown in the top right Panel of Figure 1.1. The lower right Panel of Figure 1.1 again shows a measurement of the ND_3 density as a function of storage time at the detection point. By switching the electric fields, the width of the packet after 40 round trips was confined to only 3 mm. In later measurements, Heiner and coworkers demonstrated that a packet of molecules was kept in a tight bunch even after completing 100 round trips, corresponding to a flight distance of 80 m [25]. The same group also showed the successful demonstration of the simultaneous confinement

of two molecular packets, trailing each other by about 200 mm [23].

This thesis describes the third generation of a molecular storage ring consisting of forty straight hexapoles. The increased number of segments has several advantages: (i) the transverse acceptance of the synchrotron increases when the symmetry of the synchrotron increases. Small imperfections in the construction of the ring inevitably lead to parametric amplification of the amplitude of the motion inside the ring. These losses are avoided if the periodicity of the ring is much smaller than the typical length scale of the oscillatory motion. (ii) The depth of the longitudinal well scales with the inverse of the length of a single segment. Compared to the synchrotron that consisted of two half rings, the longitudinal well is expected to increase by a factor $\sqrt{10}$. Actually, in this thesis a different bunching scheme is implemented that is a factor of three less efficient but much less demanding for the high voltage electronics. As a result the longitudinal well is about the same as that of Heiner *et al.*; however, we have come to realize that the previously used bunching scheme led to additional losses from the ring due to instabilities of the molecular trajectories and nonadiabatic transitions to nontrapped states. In the new bunching scheme these losses are absent. (iii) To operate the synchrotron as a low-energy collider, the number of simultaneously stored packets – and thus the number of ring segments – as well as the number of completed round trips need to be made as large as possible. Let us consider n packets of molecules revolving clockwise and n packets revolving anticlockwise, all with the same speed; this would require a structure consisting of n segments. After m round trips, each packet of molecules would have interacted $2 \cdot n \cdot m$ times with counter-propagating packets.

Outline of this Thesis   In Chapter 2 the production of a molecular beam with a tunable velocity is described. All elements that manipulate the motion of polar molecules using electric fields are described in detail. The two beam lines that are employed to inject counter-propagating packets into the molecular synchrotron are presented in Chapter 3. Chapter 4 derives the theoretical background necessary to describe and understand the motion of the molecules inside the molecular synchrotron. The trap frequencies that characterize the motion of the molecules inside the moving potential well are derived. The technique to longitudinally confine a packet of molecules using the electric field in the region between two hexapole segments is explained. The equations presented in Chapter 4 are partially reproduced from the theses of F. M. H. Crompvoets [22] and C. E. Heiner [26]. Chapter 5 presents experiments that demonstrate that the motion of the packet of state-selected molecules in a molecular storage ring is under full control. A decelerated molecular packet is confined for over 13 s; at this time it has traveled further than a mile and has passed through 41,000 gaps. The distance of one mile testifies to the intrinsic stability of the molecular trajectories. A number of other measurements that characterize the synchrotron are also presented in this Chapter. Chapter 6 describes the experimental technique of resonant excitation of the molecular motion. An additional small sinusoidal distortion is applied to the potential well confining the molecules. The amplitude of the motion of the molecules increases if the excitation frequency matches, or is a combination of the eigenfrequencies, of the trap. As a result of this, the molecules

are expelled from the synchrotron. This frequency-dependent depletion pattern offers direct insight into the potential well of the molecular synchrotron. Chapter 7 shows the simultaneous confinement of counter-propagating packets. The currently achievable densities of the trapped molecules are not yet sufficient to detect the desired bi-molecular collisions. Finally, in Chapter 8 a possible route for designing a next generation molecular synchrotron is discussed.

Chapter 2

From Gas in the Bottle to State-Selected Molecules with Tunable Velocities

2.1 Introduction

Full control over the internal and external degrees of freedom of molecules is desirable for molecular collision studies. If one investigates, for example, the collision of two molecules, one aims to understand, validate and extend the existing theoretical model of the investigated system. To this end, it is essential to know the internal (electronic, vibrational and rotational) and external (position and velocity in three dimensions) state of the reactants and collision products.

This Chapter explains how such control over polar molecules can be achieved. In order to understand the principle of so-called 'Stark deceleration', the ammonia molecule together with its Stark effect will first be described in detail. This will be followed by an explanation of the supersonic expansion, which is an essential prerequisite for the realization of cold molecules. Afterwards, the Stark decelerator that manipulates the motion of polar molecules will be described. At the end of this Chapter a hexapole and a buncher will be described that are used to focus the molecules transversally and longitudinally, respectively.

2.2 The Ammonia Molecule

The origin of the name 'ammonia' lies in ancient Egypt where ammonia was derived in the form of ammonium carbonate near the oasis Ammon (today Siwa) [27]. Ammonia is primarily used as fertilizer, but it is also relevant as the chemical precursor for the production of a variety of nitrogen compounds. The industrial mass production of ammonia (NH_3) was made possible by the Haber-Bosch process, which was one of the biggest chemical breakthroughs of the last century. The binding of the nitrogen molecules from air with hydrogen ($N_2 + 3\,H_2 \rightarrow 2NH_3$) in the mass production of ammonia was meant to counter act the global threat of starvation. Since then there has been a strong correlation between world population and ammonia production [27]. Also not negligible is the use of ammonia in the production of explosives, leading to the prolonged wars.

The NH_3 molecule is a classic textbook example of a pyramid/shaped symmetric/top molecule [28]. The three hydrogen atoms (or in the case of its deuterated form ND_3 the three deuterium atoms) build the ground plane of the pyramid while the nitrogen atom
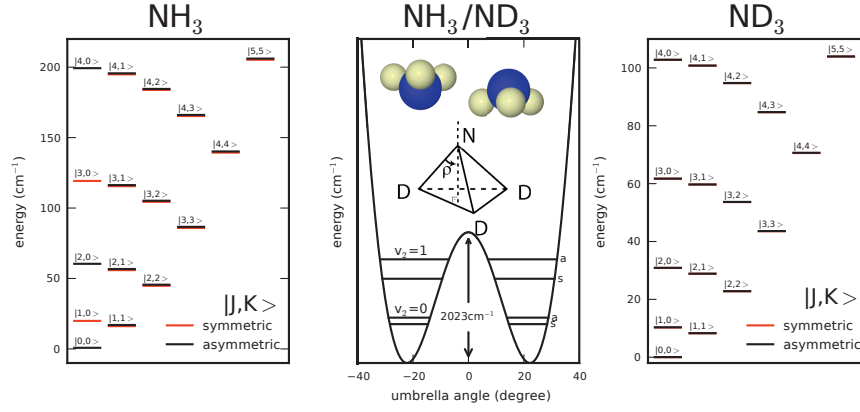
Figure 2.1: The energy level structure of two ammonia isotopologues. On the left side, the rotational energy level scheme in the vibronic ground state for NH_3 is shown. On the right side the energy level scheme is shown for ND_3. The inversion splitting is almost not visible on this scale. The middle part shows a schematic of the vibrational structure of ammonia. Due to the tunneling of the nitrogen atom through the plane spanned by the three hydrogen or deuterium atoms and the resulting umbrella motion, the (J,K)-rotational states are split into inversion doublets. For clarity the inversion splitting is exaggerated.

sits at its apex (see schematic drawing in Figure 2.1). The symmetry axis is shown as a dashed line. The two moments of inertia perpendicular to the symmetry axis are equal ($I_A=I_B$) and smaller than I_C so that ammonia is an oblate symmetric/top molecule. ND_3 is used instead of NH_3 molecules in this thesis as ND_3 has a more favorable Stark shift (to be discussed in the next Section). Assuming that the kinetic energy of the electrons inside a molecule is much higher than the kinetic energy of the nuclei, the total energy of the molecule (E_{total}) can be approximated by the sum of three main individual parts: The electronic, the vibrational and a rotational part (Born-Oppenheimer approximation).

$$E_{\text{total}} = E_{\text{el}} + E_{\text{vib}} + E_{\text{rot}}. \tag{2.1}$$

Rotational Structure The rotational structure of NH_3 and ND_3 is best described by two principal quantum numbers J and K, which are the total angular momentum and its projection onto the molecular axis, respectively. For a rigid oblate symmetric-top rotor the rotational energy can be expressed, in wavenumbers [29], as

$$F_{J,K} = BJ(J+1) + (C-B)K^2 \tag{2.2}$$

$$\text{with} \quad A = B = \frac{\hbar}{4\pi c I_{A,B}}; \quad C = \frac{\hbar}{4\pi c I_C}. \tag{2.3}$$

Here, $I_{A,B}$ are the moments of inertia perpendicular and I_C the moment of inertia parallel to the symmetry axis. Due to centrifugal distortion each energy level is shifted

(J- and K-dependent). Š. Urban *et al.* and L. Fusina describe in full detail the rotational energy of the electronic/vibronic ground state of NH_3 and ND_3, respectively. Using the rotational constants for NH_3/ND_3 [30, 31] the energies of the first four rotational states were calculated, and are shown on the left and right side of Figure 2.1, respectively. For a given J value, the rotational energies decrease with increasing K due to the oblate structure of ammonia. The inversion splitting (see next paragraph) is not visible on the energy scale.

Inversion Splitting Both ammonia isotopologues undergo vibrational motions. During the so-called 'umbrella'-motion the nitrogen atom can tunnel through the plane of the hydrogen/deuterium atoms (or vice versa) which results in a potential barrier inside the potential energy curve (see middle part of Figure 2.1). The tunneling is known to be fast, due to the light mass of the hydrogen atoms and the weak interaction of the hydrogen atoms with the nitrogen. The horizontal lines show schematically the two umbrella vibrations ($v_2 = 0$ and $v_2 = 1$ mode) which are below the barrier. At the two potential minima the umbrella angle is $\pm 22°$. Since the 1930's, a number of different approaches have been used to describe the potential function for the inversion of ammonia with an analytic formula (*e.g.* [32, 33, 34]). It was found that the vibrational potential well depth for ND_3 and NH_3 is about 2023 cm^{-1}. Due to the inversion, each level splits up into symmetric and antisymmetric levels, which is schematically shown in Figure 2.1 (splitting is enlarged). An oblate pyramid-shaped symmetric-top molecule would have a C_{3v} symmetry, but due to the tunneling inversion symmetry, a D_{3h} point group symmetry is used to describe the ro-vibrational energy. For NH_3, where the spin of the identical nuclei is $1/2$, only A_2 and E levels can occur [28]. If $K = 0$ and J is even/odd only the asymmetric/symmetric doubling components occur. For historical reasons all levels with E symmetry are called para-levels. The rotational ground state of para-ammonia is then the $|J, K\rangle = |1, 1\rangle$ state and has E symmetry. For ND_3 all rotational states (A_1, A_2 and E) are allowed. In the $|J, K\rangle = |1, 1\rangle$ state, relevant for Stark deceleration, the inversion splitting is 0.79 cm^{-1} [30] and 0.053 cm^{-1} [31] for NH_3 and ND_3, respectively.

2.3 The Stark Effect of Ammonia

Due to the uneven charge distribution over the molecule, both ammonia isotopologues have a permanent electric dipole moment. For the ground state of NH_3 the dipole moment has a value of 1.47 Debye [35] and for ND_3 1.50 Debye [36]. The Stark shifts are given by the eigenvalues of $H_0 + H_{\text{Stark}}$, relative to the eigenvalues of the field-free hamiltonian H_0

$$\widehat{H}_{\text{Stark}} = -\boldsymbol{\mu} \cdot \boldsymbol{E}. \tag{2.4}$$

It is convenient to use rigid rotor wave function $|J, K, M, p\rangle$ as the Eigenfunction of the rotational state, with M the projection of the total angular momentum on the space-fixed axis, $\boldsymbol{\mu}$ is the electric dipole moment and $\boldsymbol{E}$ the electric field, while p indicates the parity. The primed indices indicate a different state, because the Stark effect for the same state
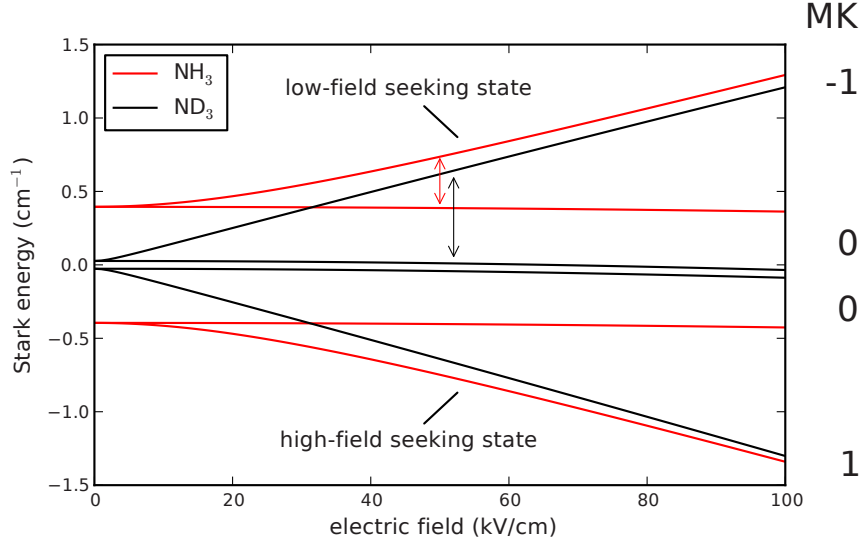
Figure 2.2: The Stark energy of the $|J, K\rangle = |1, 1\rangle$ state of NH_3 and ND_3 as a function of the electric field. The red and the black arrow indicate the change in Stark energy at an electric field strength of $50 \, kV/cm$ for ammonia and its deuterated isotopologue, respectively.

is zero. Since the upper and lower inversion doublet of ammonia have opposite parity, these two states are coupled by the Stark Hamiltonian in first order. Assuming that the energy difference between different rotational states is large, the resulting Stark energy of the interacting inversion doublet levels is in the first approximation given by [36]

$$E_{\text{Stark}} = \pm \sqrt{\left(\frac{W_{\text{inv}}}{2}\right)^2 + \left(\mu E \frac{MK}{J(J+1)}\right)^2} \mp \left(\frac{W_{\text{inv}}}{2}\right), \qquad (2.5)$$

with W_{inv} being the above mentioned inversion splitting of ammonia.

In Figure 2.2 the energy of the ground state of para-ammonia is plotted as a function of the electric field. The product of M and K, which is referred to in the following as MK, is 0 or $+1$ in the symmetric state, and 0 or -1 in the antisymmetric state. In the presence of an electric field some energy levels shift with increasing electric field. For $MK = +1$ the Stark energy decreases with increasing electric field strength, while for $MK = -1$ the Stark energy increases. Molecules in the $MK = -1$ state are called low-field-seeking states because they lower their interaction energy with the electric field by moving to the lowest field. Vice versa, molecules in the $MK = +1$ state are high-field-seeking. In first order approximation, the $MK = 0$ states are not affected by the electric field.

The main reason why the experiments in this thesis were done using ND_3 and not NH_3 is due to the different Stark effect of both isotopologues. As indicated by the

10

red and black arrows in Figure 2.2, the relative change in Stark energy of a low-field-seeking molecule in a given electric field is smaller for NH_3 than for ND_3. In other words, a deuterated ammonia molecule which flies into an inhomogeneous electric field will gain more Stark energy than its non deuterated isotopologue. It will therefore lose more kinetic energy which is advantageous for the process of Stark deceleration (see Section 2.5). A second benefit of ND_3 is the linearity of the Stark shift. Compared with NH_3, ND_3 has a small inversion splitting and is thus more sensitive to low electric fields ($0 - 50\,kV/cm$).

2.4 The Supersonic Expansion

Nowadays the supersonic beam method is a well established technique to investigate atomic and molecular properties. The expansion of atoms and/or molecules into a low pressure region results in an arrangement of co-moving particles (beam), which are ideally suited for fundamental physical and chemical investigations [37]. The main benefits are (a) the collision-free environment, (b) the well-defined geometrical and energetic conditions and (c) the cooling effect of the internal state distribution without condensation of atoms and/or molecules.

Atomic and molecular beams date back to the early 1920s, starting with the seminal experiment by Stern and Gerlach [38] who demonstrated the magnetic quantization of silver atoms. Another example was the focusing of an ammonia beam with a hexapole which led to the famous experiment of Gordon, Zeiger and Townes [39, 40]. They showed that an inverted population of ammonia molecules emits coherent microwave radiation. The so-called MASER (*Microwave Amplification by Stimulated Emission of Radiation*) was the precursor of the laser. Currently many other physical and chemical experiments use molecular beams and in particular, supersonic expansions. For example supersonic beams are used in cluster physics, scattering studies, *etc.* [37].

This paragraph serves as a brief summary of the main concepts of pulsed supersonic expansions, a detailed description can be found for instance in [37] and [41]. Subsequently, the concept of phase-space density is introduced, with which the cooling of the supersonic expansion is described. The phase-space density is defined as the number of particles per space interval and velocity interval (in six dimensions) and determines how far an ensemble of particles is away from quantum degeneracy [42].

The energy E of a mole of gas is given generally as

$$E = U + p \cdot V + \frac{1}{2}Mv^2. \tag{2.6}$$

Here, U is the internal energy, p the pressure, V the volume and $1/2Mv^2$ the kinetic energy. In a gas reservoir with temperature T_0 and a pressure p_0 all particles follow a Maxwell-Boltzmann velocity distribution centered around $0\,m/s$ (see lower left side of Figure 2.3). If particles expand through a small orifice into a vacuum ($p_1 \approx 0$) along the z-axis, the internal energy decreases and the particles cool down adiabatically. The conservation of energy demands that the mean velocity of the particles increases to
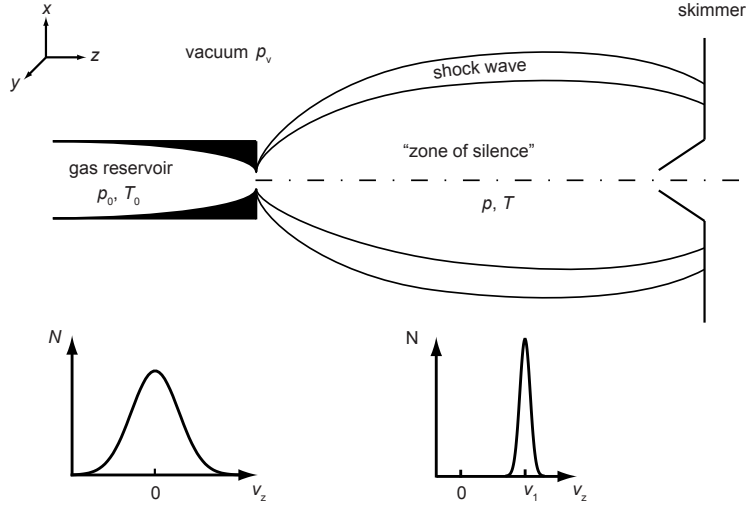
Figure 2.3: Top: Schematic view of a supersonic expansion. A thermalized gas of molecules or atoms contained in a reservoir at a temperature T_0 and pressure p_0 expands into vacuum. A few centimeters behind the valve, a skimmer selects only a part of the beam which is then translationally fast, but has a small velocity spread in both transversal and longitudinal directions. Lower part: velocity distribution inside the reservoir (left) and after the expansion in the forward direction (right).

compensate for this:

$$U_0 + p_0 \cdot V_0 = U_1 + \frac{1}{2}Mv_1^2. \tag{2.7}$$

If the orifice is smaller than the mean free path, particles do not collide while leaving the reservoir. Hence, the relative velocity distribution in the beam is the same as in the reservoir. This is called an effusive beam. If, on the other hand, the orifice is much larger than the distance that a particle travels before colliding with another particle, many collisions occur during the expansion. The collisions in the expansion cause a change in the velocity distribution. The particles now have a non-zero forward mean velocity v_1, and in the moving frame a narrower velocity distribution compared with inside the reservoir (see lower right side of Figure 2.3). As the velocity in the beam exceeds the local speed of sound, this expansion is called 'supersonic'. This has the important consequence that disturbances that occur in the trailing edge of the pulse cannot influence the leading edge.

For an ideal gas the specific heat capacity c_p at a constant pressure is defined as

$$c_p = \frac{\gamma}{\gamma - 1}\frac{R}{M} \tag{2.8}$$

with the adiabatic index γ and the universal gas constant R. For a mono-atomic gas like helium γ is 1.67, for ammonia γ is 1.29 at room temperature. If the expansion is

assumed to be isentropic, *i.e.*, the change in entropy is negligible, the relation between density n and temperature T before and after the expansion is

$$\frac{n_1}{n_0} = \left(\frac{T_1}{T_0}\right)^{(\gamma-1)^{-1}}. \tag{2.9}$$

With the thermal de Broglie wavelength

$$\Lambda = \sqrt{\frac{2\pi\hbar}{mkT}}, \tag{2.10}$$

one can determine the phase-space density, a dimensionless parameter,

$$D = n\Lambda^3, \tag{2.11}$$

which is also called the degeneracy parameter. At ambient temperatures, Λ is very small compared to the distance between particles and a classical description of the particles is sufficient. If the temperature is decreased the thermal wavelength grows, and one can reach the point where the thermal de Broglie wave overlaps with surrounding particles and quantum effects occur. This happens when $n\Lambda^3 > 1$.

Ammonia not only has translational but also rotational and vibrational energy. During the expansion, the molecules collide and exchange energy. The collision cross section σ for elastic scattering that merely results in translational energy transfer is larger than the inelastic cross section that results in rotational or vibrational energy transfer. As a result the energy and the corresponding temperature is smaller for translational motion than for rotation and vibration after the expansion;

$$\sigma(E_{\text{trans}} \leftrightarrow E_{\text{trans}}) > \sigma(E_{\text{rot}} \leftrightarrow E_{\text{trans}}) > \sigma(E_{\text{vib}} \leftrightarrow E_{\text{trans}}) \tag{2.12}$$

$$T_{\text{trans}} < T_{\text{rot}} < T_{\text{vib}}. \tag{2.13}$$

The translational temperature of a molecular packet in the experiment described in this thesis is typically about a Kelvin, the rotational temperature is between 1 and 10 K and the vibrational temperature is roughly 50 K. By seeding ammonia with a noble gas, more of the internal energy of ammonia is transferred to translational energy. In this thesis a cold mixture ($T = -70°\,C$) of ammonia with xenon (ratio 1:20) is used. A backing pressure of $p = 2\,\text{bar}$ results in a density of $n = 3.6 \cdot 10^{18}$ molecules per cm^3 ($p = nkT$). Inside the reservoir $\Lambda = 0.28\,\text{Å}$ and D (integrated over all states) is $7.2 \cdot 10^{-8}$. Only 0.4 % of the ammonia molecules are in the $|J = 1, KM = -1\rangle$ state [43]. The phase-space density for this state is thus $5.4 \cdot 10^{-10}$ – so the gas is far from degeneracy. After the expansion, the translational energy is 1 K. Using Equation (2.9) and $\gamma \approx 1.65$ results in $1.1 \cdot 10^{15}$ molecules per cm^3 and $\Lambda = 3.9\text{Å}$. Principally only the rotational ground state will be populated, and roughly 20 % are in the low-field seeking $|J = 1, KM = -1\rangle$ state implying a phase-space density of $6 \cdot 10^{-8}$. Please note that experimentally the number of density after a supersonic expansion is much smaller than follows from this theory.

If a continuous supersonic beam with a relatively high backing pressure were used, large turbo pumps would be necessary to maintain a good vacuum. One can reduce the flow of gas significantly by using pulsed valves. In the experiments described in the following Chapters the valve is being opened only for a very short time (about 100 μs) and is synchronized with the pulsed laser at a repetition rate of 10 Hz.

2.5 The Stark Decelerator

Stark deceleration relies on the interaction of the electric dipole moment of a molecule with time-dependent electric fields. The electric field must be controlled such that molecules move repeatedly towards a high inhomogeneous electric field. By this process low-field seeking molecules continuously lose kinetic energy at the cost of Stark energy and are decelerated. The process is state selective because the Stark shift differs from state to state. The Stark decelerator is described in detail in [44, 45].

Longitudinal Motion Figure 2.4 shows schematically the concept of a Stark decelerator. It consists of p pairs of electrodes each separated by a distance L and aligned on one axis. Opposite electrodes have different polarities and are connected to a fast high voltage switch. Two switching configurations are used to apply the voltage to the Stark decelerator:

1. Every odd pair is on a positive or negative high voltage $\pm V_0$; every even pair on ground (upper left side in Figure 2.4)

2. Every even pair is on a positive or negative high voltage $\pm V_0$; every odd pair on ground (lower left side in Figure 2.4)

A low-field seeking molecule which flies into an inhomogeneous field that is produced by the two electrodes with different polarity gains Stark energy. To conserve the total energy, the kinetic energy is decreased. The molecule becomes slower. If the fields are not switched it will regain its original velocity as it passes the maximum in the electric field. If the electric field is switched to the second configuration before the molecule leaves the high field, the molecule loses kinetic energy permanently. This molecule then flies once more into a region of high electric field and this deceleration process can be repeated $(p-1)$ times. For deuterated ammonia and the voltages used in the experiments described in the following Chapters, about one wavenumber of kinetic energy can be removed per stage. In order to bring ND_3 molecules from a supersonic beam (initial velocity about 300 m/s) to standstill, roughly 100 of these stages are needed.

Let us now derive the equations of motion in the longitudinal direction: The electric field has a periodicity of $2L$ and the motion of the molecules is described in a reduced $z\pi/L$-system. The longitudinal Stark energy as a function of position z is described as
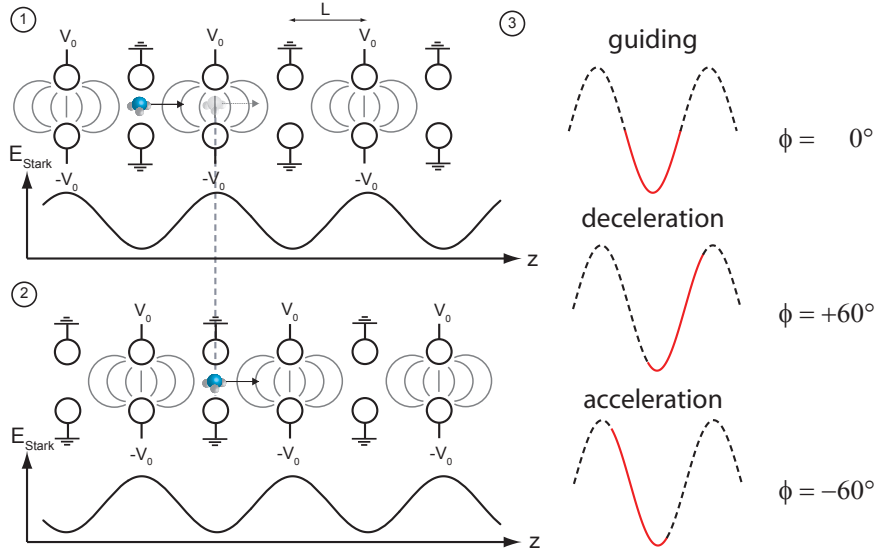
Figure 2.4: Schematic of the Stark decelerator principle. Top left: A molecule flies along the molecular beam axis (z-axis) through an array of electrode pairs. Every odd pair is on high voltage $\pm V_0$, every even pair is grounded. A low-field seeking molecule experiences a position dependent Stark energy E_{Stark} as sketched below. This molecule will gain Stark energy at the cost of kinetic energy and will slow down. If it passes the electric field maximum, which corresponds to the position of the high voltage electrodes, it will regain the kinetic energy at the cost of Stark energy. If the electric field is switched to configuration 2 (lower left Panel - every even pair is on high voltage and every odd pair is grounded) before the molecule passed the electric field maximum, the molecule loses the kinetic energy permanently. The energy by which the molecule is decelerated corresponds to the Stark energy it gained by flying into the inhomogeneous electric field. This deceleration process is repeated several times by switching between configuration 1 and 2 as the molecule travels through the array of deceleration stages. The amount of energy lost at each stage is best parametrized by the phase angle ϕ. ϕ is the position of the molecule with respect to the next electrodes that are at high voltage at the time when the electric fields are switched. If ϕ is $0°$ (see top part of Panel (3)), the molecule will not change its total velocity because it is accelerated and decelerated by the same amount. If, *e.g.*, ϕ is $+60°$ the molecule is decelerated and if ϕ is $-60°$ the molecule is accelerated, as can be seen in the mid and lower part of section (3), respectively.
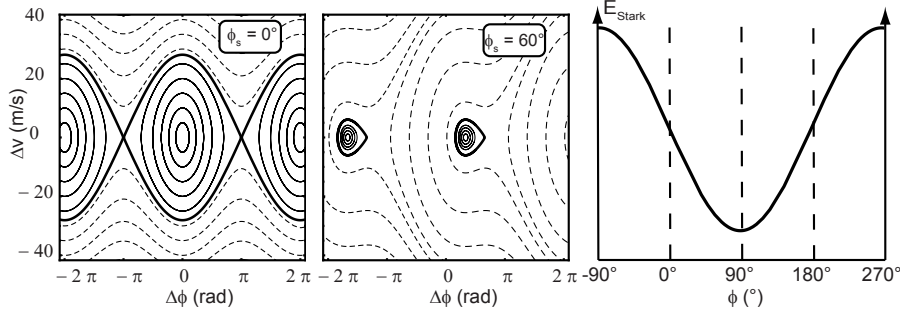
Figure 2.5: Two phase-space stability diagrams for ND_3 molecules in the $|J, MK\rangle = |1, -1\rangle$ state for $\phi = 0°$ (left figure) and $\phi = 60°$ (center figure). The separatrix is shown as a thick line. Molecules inside this separatrix are longitudinally confined in a stable fashion. 2π corresponds to 11 mm, which is twice the distance between two electrode pairs. The right figure shows the E_{Stark} immediately after the switching process to determine the phase angle ϕ.

a Fourier series [46].

$$
\begin{aligned}
W(z\pi/L) &= \frac{a_0}{2} + \sum_{n=1}^{\infty} a_n \cos\left(n(z\pi/L + \pi/2)\right) \\
&= \frac{a_0}{2} - a_1 \sin z\pi/L - a_2 \cos 2z\pi/L + a_3 \sin 3z\pi/L + \dots \quad (2.14)
\end{aligned}
$$

The kinetic energy ΔE_{kin} that a molecule loses during a switching process depends on its relative positions at the start and end of one switching configuration. In analogy to particle accelerators, it is described with the phase angle ϕ, which corresponds to the position of the molecule with respect to the next pair of electrodes that is at high voltage at the time when the electric fields are switched. If, *e.g.*, $\phi = 90°$ the molecule is between two adjacent high voltage electrodes when the field is switched. If $\phi = 0°$ the molecule is between two electrode pairs when the fields are switched. It is first accelerated and then decelerated by the same amount before the field is switched again (see right part of Figure 2.5).

To describe a molecular packet inside a Stark decelerator the concept of a synchronous particle is used. A synchronous molecule has phase ϕ_s that stays constant during the deceleration process. This molecule loses the same amount of kinetic energy $\Delta E_{\text{kin}}(\phi_s)$ every time the fields are switched.

$$
\Delta E_{\text{kin}}(\phi_s) = W(\phi_s + \pi) - W(\phi_s) = 2a_1 \sin \phi_s + 2a_3 \sin 3\phi_s + \dots \quad (2.15)
$$

Molecules in an ensemble are best described relative to the motion of the synchronous molecule. Under the assumption that a molecule experiences an averaged force $\overline{F}$ between two switching cycles, the first-order non-linear equation of motion is

$$
\frac{mL}{\pi} \frac{d^2\Delta\phi}{dt^2} + \frac{2a_1}{L} \left[\sin\left(\Delta\phi + \phi_s\right) - \sin\phi_s\right] = 0. \quad (2.16)
$$

16
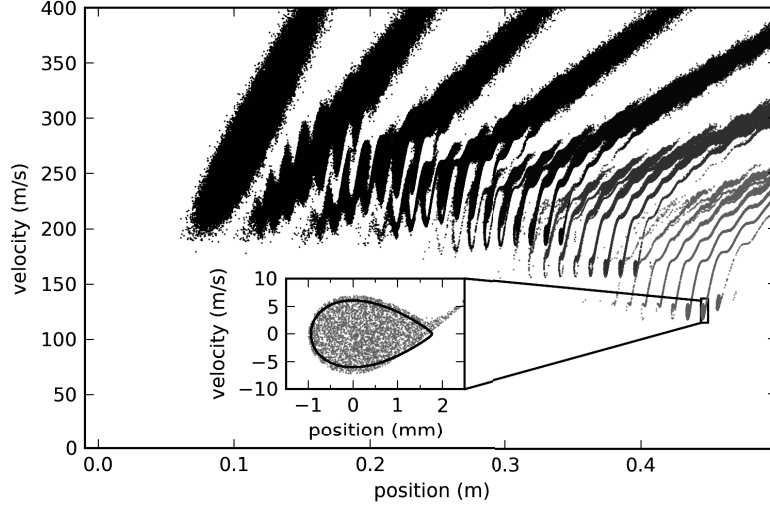
Figure 2.6: Numerically calculated one dimensional phase-space distribution of a packet of ammonia molecules in the $|J, MK\rangle = |1, -1\rangle$ state at seven different timings flying through a Stark decelerator with 62 stages. From black to gray, or respectively from left to right, the distribution are shown before the decelerator is switched, after 10, 20, 30, 40, 50 and 62 switching stages. The inset shows the phase-space acceptance of the decelerated packet relative to the synchronous molecule which is at the origin of the plot in the inset. The black curve shows the calculated separatrix using Equation (2.16).

Here, $\Delta\phi = \phi - \phi_s$ is the difference in phase to the synchronous molecule. In Figure 2.5 two phase-space diagrams for deuterated ammonia in the $|J, MK\rangle = |1, -1\rangle$ state are shown for different phase angles. Each line represents a trajectory of a molecule. Solid lines correspond to molecules which are decelerated in a stable fashion. They move in phase-space around the synchronous molecule. Dashed lines are trajectories which are not stable. The area of stable trajectories is surrounded by the separatrix (thick line). For $\phi_s = 0°$ the acceptance area, the so-called 'phase fish', has a maximum area but molecules are neither accelerated nor decelerated. This sequence is called *guiding* (top right part of Figure 2.4). If ϕ_s is between $0°$ and $90°$, molecules are decelerated, whereas when ϕ_s is between $0°$ and $-90°$ molecules are accelerated. The higher the phase angle, the stronger the change in kinetic energy per stage but the smaller the phase-fish. In this case fewer molecules can be stably confined.

The final velocity of the molecular packet is determined only by the time sequence of the high voltage pulses. The more the molecules are decelerated, the longer the duration time inside a deceleration stage and the longer the time duration between switching cycles.

Figure 2.6 shows a one dimensional numerical calculation with 200,000 molecules. The decelerated deuterated ammonia molecules are separated in time and space from

the main molecular beam pulse. In this simulation a packet of molecules is decelerated from 281 m/s to 124.3 m/s using a phase angle of 60°. Shown are seven different phase-space distributions in the longitudinal direction at different times. From left to right (from black to gray) the molecular packet is shown before the first switching of the electric fields and after 10, 20, 30, 50, and 62 switching cycles. The overall tilt in the forward direction is caused by the free-flight of molecules. The majority of the molecules maintain their forward velocity and are only slightly affected by the switching of the electric field. Three packets of molecules are seen to stay together in compact bunches and are decelerated. The middle packet contains the synchronous molecule with the final velocity of 124.3 m/s. The inset shows the phase-space distribution of this packet relative to the synchronous molecule. The position spread is 2.5 mm and the velocity spread is 12 m/s. The distance of the packet in front of the synchronous molecule is 11 mm, corresponding to the decelerator periodicity of $2L$. The molecules in this packet were in the third decelerator stage when the electric field was switched for the first time. This packet only experienced 60 deceleration stages resulting in a final velocity of 132 m/s. The packet behind the synchronous molecule is also 11 mm away. Molecules in this bunch are in the first deceleration stage when the synchronous molecule is $2L$ ahead. These molecules are accepted with a velocity centered around 277 m/s when the electric field is switched the third time, and are decelerated to 124.3 m/s.

Transverse Motion   The goal of a Stark decelerator is to slow down molecules in the z direction. But it is crucial that during the deceleration process the motion in the transverse direction (x,y) is also stable. The transverse motion in a Stark decelerator is described in detail in [47]. By orienting successive electrode pairs at 90° to each other, transverse focusing can be achieved. The transverse focusing force is strongly dependent on the phase angle. For a phase angle close to 0°, this force is small so that molecules close to the synchronous molecule are only transported when they have a small transverse velocity. Furthermore, the variation of the focusing force as a function of phase causes parametric amplification of the transverse motion. In this work the Stark decelerator is operated with a phase angle of 60° such that the molecular packet experiences a sufficient transverse focusing force [47].

There are different approaches to improve the transversal confinement. If the decelerator is not switched every stage, but every third, a transverse focusing can be achieved for all phase angles. A consequence of this operation is that more stages are needed to reach a given final velocity [48]. A second, totally different, approach is to use ring electrodes and to apply a traveling electric potential well. The decelerated molecules experience a permanent transverse confining field. This was successfully demonstrated by Osterwalder and coworkers [49].

2.6 The Buncher

While a Stark decelerator produces a tight molecular packet in phase-space, a buncher is needed to focus this packet longitudinally into the molecular synchrotron [50]. Molecules
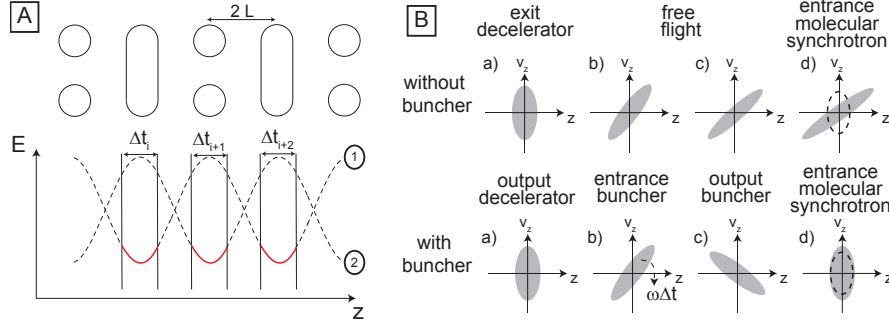
Figure 2.7: A: The upper part shows a schematic drawing of a buncher together with the resulting electric fields generated by configurations 1 and 2. Compared to a Stark decelerator all dimensions are scaled up by a factor of two. The molecules only experience the electric fields during the time intervals Δt_i (red line), positioned symmetrically around the electric field minimum. The mean velocity of the packet is not changed.
B: Schematic phase-space distribution of a molecular packet without and with bunching. A molecular packet at the end of a Stark decelerator has a position and velocity distribution. Without a buncher, the packet 'smears' out and only a part of the distribution falls within the phase-space acceptance of the molecular synchrotron (dashed curve). A buncher in between this free flight region rotates this phase space distribution by an angle of $\omega\Delta t$, such that the packet overlaps with the phase-space acceptance of the molecular synchrotron.

leave the decelerator with a phase-space distribution that is almost symmetric around the synchronous molecule, as sketched in the upper right part of Figure 2.7. In the free-flight region between the exit of the decelerator and the molecular synchrotron, the packet 'smears' out because the faster molecules will move ahead of the slower ones. The buncher is used to refocus the molecular packet in the longitudinal direction.

The buncher consists of q electrode pairs, similar to a Stark decelerator, but with all dimensions scaled up by a factor of two. Consequently the distance between two electrode pairs is $2L = 22\,\mathrm{mm}$. The scaling up is not essential, but a larger buncher can more easily accept a molecular packet that spread out due to the free flight between decelerator and buncher. The high voltage is switched between two configurations with $\phi = 0°$, such that the synchronous molecule is not accelerated or decelerated longitudinally. The left side of Figure 2.7 shows that the synchronous molecule only experiences the symmetric part of the electric field for a time duration Δt_i. A molecule that is behind the synchronous molecule will experience a net acceleration and will be pushed towards the synchronous molecule. Conversely, molecules in front of the synchronous particle will experience a force backwards to the synchronous molecule. The packet will be 'bunched'. If the buncher has q electrode pairs, the electric field is switched $(q-2)$ times. The molecular packet undergoes a phase-space rotation of $\omega\Delta t$ with Δt being the sum over the individual time-intervals Δt_i and ω being the angular frequency of the rotation of the distribution in phase-space.

If the distance between the end of the decelerator and the buncher is L_1 and L_2 is

the distance from the buncher to the molecular synchrotron, a spatial focus is achieved if the buncher is switched on for a total time of

$$\Delta t = v_s \frac{L_1 + L_2}{\omega^2 L_1 L_2 - v_s^2} \tag{2.17}$$

where v_s is the velocity of the synchronous molecule [50].

Δt can also be chosen such that the molecular packet experiences a velocity focus. The phase-space distribution would then be rotated such that the velocity distribution is minimal. In this way molecules are longitudinally cooled.

2.7 The Hexapole

The molecules spread out in the longitudinal direction but also in the transverse direction. A linear restoring force is needed to focus the molecules back onto the molecular beam axis. In the early 50's of the last century, Gordon, Zeiger and Townes [39] and independently Bennewitz, Paul and Schlier [51] demonstrated a way to focus polar molecules with electric fields. Depending on the type of Stark effect of the molecule, the electric field needs to have a specific shape to create the above mentioned restoring force $\boldsymbol{F}(\boldsymbol{r})$. In an electric field a polar molecule experiences a force

$$\boldsymbol{F}(\boldsymbol{r}) = -\nabla E_{\text{Stark}}(\boldsymbol{r}). \tag{2.18}$$

One can rewrite this equation in a form similar to that of the force acting on a charged particle in an electric field ($F = qE$)

$$\boldsymbol{F}(\boldsymbol{r}) = \mu_{\text{eff}} \nabla |\boldsymbol{E}(\boldsymbol{r})|, \tag{2.19}$$

where μ_{eff} is the effective electric dipole moment which is equal to the negative derivative of the Stark energy with respect to the electric field strength.

As deuterated ammonia experiences a linear Stark effect, an electric field is needed that scales quadratically from the molecular beam axis in order to produce a linear restoring force. To achieve a perfect hexapole field the electrode geometry needs to be hyperbolic [37]. However, in this case the distance between neighboring electrodes with different polarity would become very small and it would not be feasible to apply high voltage. Using a finite element program R.W. Anderson found that a rod radius of $R = 0.565\, r_0$ is a slightly better approximation [52] to the ideal hexapole field than the $R = 0.5\, r_0$ that Reuss proposes [37]. A hexapole consisting of six parallel rods can create such a field (see left side of Figure 2.8). V_0 is the voltage difference between neighboring rods and r_0 is the inner radius of the hexapole. Here the cylindrical electrodes have a diameter that is equal to r_0 following the approach of Reuss [37]. The electric potential for an ideal hexapole in polar coordinates (r,φ) is [53]

$$V(r, \varphi) = \frac{V_0}{2} \left(\frac{r}{r_0} \right)^3 \cos 3\varphi. \tag{2.20}$$
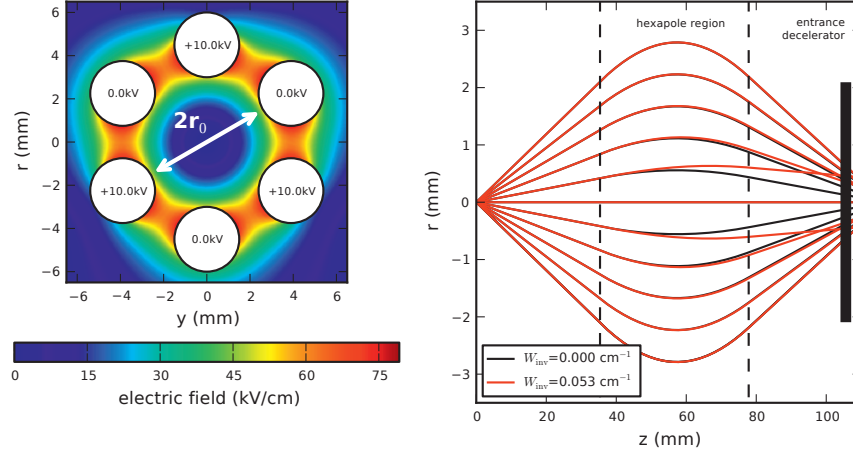
Figure 2.8: Left: The electric field generated by a hexapole with an inner radius of $r_0 = 3\,\text{mm}$ and a voltage difference $V_0 = 10\,\text{kV}$ is shown. A molecule with a linear Stark shift experiences a stronger force towards the molecular beam axis the further it is off from the hexapole center.
Right: As an example of a hexapole, the trajectories of ND_3 molecules in the $|J, MK\rangle = |1, -1\rangle$ state are shown that leave the valve (approximated as a point source) with different angles but are refocused to the molecular beam axis with a hexapole. The $10\,\text{kV}$ voltage difference is applied for a time duration of $160\,\mu\text{s}$ and the molecules have a longitudinal velocity of $281\,\text{m/s}$. If the inversion splitting is zero, molecules experience a perfectly linear restoring force (black lines). With the actual inversion splitting of $0.053\,\text{cm}^{-1}$ the molecules are not be focused back into a single point but onto a circle (red lines).

The absolute value of the electric field is

$$|\boldsymbol{E}(\boldsymbol{r})| = 3\frac{V_0}{2}\left(\frac{r^2}{r_0^3}\right). \tag{2.21}$$

Combining Equation (2.21) with Equation (2.5), the Stark energy of ammonia can be written as

$$E_{\text{Stark}} = \pm\sqrt{\left(\frac{W_{\text{inv}}}{2}\right)^2 + \left(\mu\frac{3V_0}{2}\frac{r^2}{r_0^3}\frac{MK}{J(J+1)}\right)^2} \mp \frac{W_{\text{inv}}}{2} \tag{2.22}$$

$$= \pm\sqrt{\left(\frac{W_{\text{inv}}}{2}\right)^2 + \left(\frac{kr^2}{2}\right)^2} \mp \frac{W_{\text{inv}}}{2}, \tag{2.23}$$

with

$$k = \mu\frac{3V_0}{2r_0^3}\frac{|MK|}{J(J+1)} \tag{2.24}$$

being the harmonic force constant. The plus and minus sign denote the low-field and high-field seeking molecules, respectively. From Equation (2.18) the resulting force is

then [22]

$$\boldsymbol{F}(\boldsymbol{r}) = \mp \frac{kr}{\sqrt{1 + \left(\frac{W_{\text{inv}}}{kr^2}\right)}} \hat{\boldsymbol{r}}. \tag{2.25}$$

If the inversion splitting in ammonia would be zero, the restoring force would be perfectly linear. On the right side of Figure 2.8 trajectories show how deuterated ammonia molecules are focused using a hexapole that is located just between the valve and the Stark decelerator. A divergent beam of ammonia molecules is leaving the valve (assumed to be a point source) with a forward velocity of $v_z = 281\,\text{m/s}$. A voltage difference of $10\,\text{kV}$ is applied on the hexapole for a time duration of $160\,\mu\text{s}$ (dashed lines). If the inversion splitting is zero (black lines) the molecules are focused into a single point just inside the Stark decelerator. With a non-zero inversion the molecules experience a non-linear force and are not focused on a single point but onto a circle (red lines).

Chapter 3

Two Stark Decelerator Beam Lines

3.1 Introduction

As discussed in Chapter 1, the primary goal of a molecular synchrotron is to investigate the energy dependence of the scattering cross section for collisions of state-selected polar molecules. In order to inject two different types of molecules into a molecular synchrotron simultaneously, two Stark decelerator beam lines are needed. While the previous Chapter describes the different elements used to manipulate the motion of polar molecules, this Chapter will focus on the experimentally employed beam lines and explain in detail their characteristics and usage. First the setup of both beam lines is described. Characterization measurements demonstrate the level of control that can be achieved over a molecular packet of ND_3 molecules. The last Section will address variation of the collision energy. Changing the phase angle of the Stark decelerator tunes the final velocity of the beam. Focusing elements such as hexapoles and bunchers need to be tuned together with the phase angle to maintain a tight packet of ND_3 molecules.

3.2 Beam Lines 1 and 2

Two different decelerator beam lines are used in the experiments described in this thesis. One of them has an impressive track record of decelerating molecules (beam line 1). It was the first decelerator to slow down polar molecules [5] and led to the first trapping experiments of deuterated ammonia [6]. In 2001 the first demonstration of a storage ring for polar molecules was shown, again using a part of this beam line [24]. The molecular synchrotron consisting of two hexapole half rings, which is the direct predecessor of the molecular synchrotron described in this thesis, also successfully used beam line 1 [23]. The second decelerator beam line (beam line 2) was built after the demonstration of a packet of ammonia molecules flying a flight length of one mile within the molecular synchrotron [54]. Compared to beam line 1, beam line 2 is similar but some features were changed in order to improve the setup.

3.2.1 Experimental Setup

Both decelerator beam lines are positioned inside a vacuum chamber. The two source chambers and the two differentially pumped deceleration chambers are each pumped with a $500\,l/s$ and a $700\,l/s$ turbomolecular pump for beam line 1 and 2, respectively.
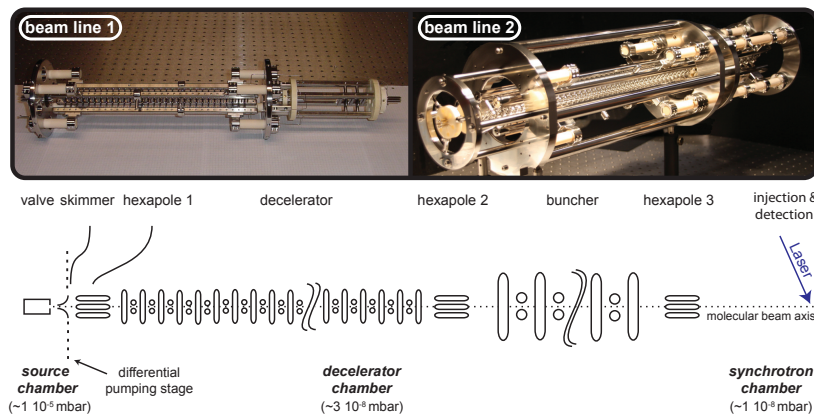
Figure 3.1: Top: Photos of the two individual Stark decelerator beam lines are shown (beam line 1 on the left and beam line 2 on the right). Below is a schematic of the molecular beam line. ND_3 molecules expand together with xenon as a carrier gas into the source chamber at a repetition rate of approximately 10 Hz. After passing the skimmer the low-field seeking molecules are focused into the Stark decelerator. To ensure a good phase-space overlap of the emittance of the decelerator and the acceptance of the molecular synchrotron, two hexapoles (hexapole 2 and 3) and a buncher are used to focus the decelerated beam into the synchrotron.

A photograph of each assembled beam line together with a schematic is shown in Figure 3.1. Characteristic dimensions and voltages for each beam line are given in Table 3.2. A 5 % gas mixture of ND_3 molecules in xenon at a backing pressure of 2 bar expands into the vacuum at a repetition rate of 10 Hz. Beam line 1 uses a General Valve Series 99 at $-70°$ C and beam line 2 a Jordan Valve at room temperature. During the expansion molecules collide with the carrier gas and cool translationally, rotationally and vibrationally (see Section 2.4). Afterwards, about 20 % of all ND_3 molecules are in the low-field seeking rovibrational ground state of para-ammonia ($|J, MK\rangle = |1, -1\rangle$) [46] and enter the deceleration chamber by passing a skimmer with a diameter of 1.5 mm. During operation the pressure in both source chambers is $1 \cdot 10^{-5}$ mbar and in the deceleration chambers the pressure is $3 \cdot 10^{-8}$ mbar.

The molecular packet is focused with a pulsed hexapole into the first stage of the Stark decelerator (hexapole 1). The Stark decelerator is made of 63 or 81 electrode pairs resulting in 62 or 80 deceleration stages for beam line 1 and 2, respectively. Each electrode pair consists of two parallel highly polished stainless steel cylindrical rods with a diameter of 3 mm, at a center-to-center distance of 5 mm. Before use, each electrode has been carefully inspected for mechanical defects. Successive electrode pairs are separated by $L = 5.5$ mm. To provide a transverse focusing force, alternating electrode pairs are rotated by $90°$. This produces a 2 x 2 mm^2 gap with the molecular beam axis in its center. A maximum electric field of 90 kV/cm between two electrodes is generated by applying $+10$ kV on one and -10 kV on the other electrode and grounding the two neighboring

#	name	Stark decelerator beam line 1				Stark decelerator beam line 2			
		position	length	voltage	features	position	length	voltage	features
1	valve	−20 mm	-	-	General Valve Series 99; cooled to −70° C	−20 mm	-	-	Jordan Valve C-211
2	skimmer	0 mm	-	-	skimmer radius 1.5 mm	0 mm	-	-	skimmer radius 1.5 mm
3	hexapole 1	26 mm	60 mm	10 kV	3 mm inner radius; 3 mm rod diameter	26 mm	60 mm	10 kV	3 mm inner radius; 3 mm rod diameter
4	decelerator	106 mm	341 mm	±10 kV	63 electrode pairs (62 stages); 2 mm gap; 3 mm rod diameter	106 mm	440 mm	±10 kV	81 electrode pairs (80 stages); 2 mm gap; 3 mm rod diameter
5	hexapole 2	480 mm	60 mm	10 kV	4 mm inner radius; 4 mm rod diameter	570 mm	60 mm	10 kV	4 mm inner radius; 4 mm rod diameter
6	buncher	615 mm	44 mm	±10 kV	5 electrode pairs (3 stages); 4 mm gap; 6 mm rod diameter	645 mm	110 mm	±10 kV	11 electrode pairs (9 stages); 4 mm gap; 6 mm rod diameter
7	hexapole 3	730 mm	60 mm	10 kV	6 mm inner radius; 6 mm rod diameter	920 mm	60 mm	8 kV	6 mm inner radius; 6 mm rod diameter
8	injection point	961 mm	-	-	-	1163 mm	-	-	-

Table 3.2: Dimensions and voltages of the two Stark decelerator beam lines. The position of the skimmer is set to zero. For the Stark decelerator, the buncher and the hexapole, the position corresponds to the beginning of each element.
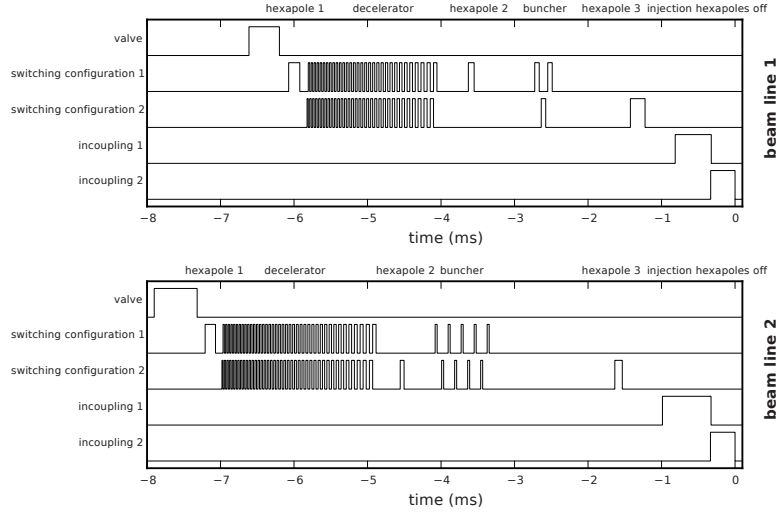
Figure 3.2: For the two beam lines typical pulse-versus-time sequences are shown for the deceleration of ND_3 molecules from about 300 m/s to 124.3 m/s. Both sequences are timed such that the synchronous molecule is injected at 0 ms into the synchrotron. The valve for beam line 1 and 2 is opened 6.6 ms and 7.9 ms before the injection, respectively. Afterwards, hexapole 1 is turned on by switching on configuration 1 for *ca.* 150 μs. When the molecules reach the first decelerator stage the electric field changes between configuration 1 and 2. The duration time of the switching process increases as the molecule needs a longer time to pass a decelerating stage. After the decelerator, hexapole 2, the buncher and hexapole 3 are turned on. To inject a molecular packet into the molecular synchrotron the injection hexapoles (incoupling 1) and the detection hexapoles (incoupling 2) need to be turned off (see Section 5.2.3). The pulse-time sequence is different for both beam lines because they have different dimensions. The first beam line is 0.98 m long, while the second beam line is 1.18 m.

electrode pairs. For the two switching configurations (see Section 2.5) two positive and two negative high voltage switches are needed.

After the Stark deceleration the molecules pass a second pulsed hexapole, which focuses the molecular packet transversely into the buncher. In the buncher all dimensions are scaled up by a factor of two compared to the Stark decelerator. Beam line 1 has five electrode pairs resulting in three bunching stages while beam line 2 has eleven electrode pairs resulting in nine bunching stages. After the buncher, a third hexapole (hexapole 3) focuses the molecules transversely into the molecular synchrotron. The injection point of both beam lines is at the same point where molecules are later ionized (see Section 3.2.2). The third hexapole can be moved transversely in order to vary the radial position where the molecules are injected in the synchrotron.

The electronic connection used for both beam lines is made such that the fewest possible high voltage switches are needed. Due to the wiring, the three hexapoles and the buncher are switched together with the decelerator. This can be seen in Figure 3.2

where for configuration 1 every even bunching stage experiences a voltage difference of $20\,\text{kV}$. At the same time a $10\,\text{kV}$ voltage difference is applied on hexapole 1 and 2 of the first beam line and on hexapole 1 of the second beam line. In the beam line the electric field is switched between a small bias voltage of $\pm 200\,\text{V}$ and $\pm 10\,\text{kV}$. The small voltage ensures that the electric field never drops below $300\,\text{V/m}$ anywhere in the decelerator. It prevents the molecules from undergoing a spin-flip transition (Majorana transition) to the upper component of the inversion doublet with $K = 0$ which is not low field seeking [55, 56]. Electrical discharges from the high voltage electrodes to the grounded chamber are avoided by using Aluminum oxide ceramics (Al_2O_3) as isolation. The third hexapole of the second beam line is connected externally to a separate switch and high voltage power supply. To prevent electronic discharges a maximum voltage difference of only $8\,\text{kV}$ is applied.

To decelerate a molecular packet from $300\,\text{m/s}$ to $124.3\,\text{m/s}$ a deceleration sequence, also called 'burst', is used that takes about $6.5\,\text{ms}$ ($8.0\,\text{ms}$) for the first (second) beam line. Both sequences are generated by calculating the trajectory of the synchronous molecule through the deceleration beam line. The trigger to the burst sequence is chosen such that both packets are injected at the same time. The trigger pulses for the high voltage switches are made by a programmable delay generator. The heat load on the switches, and the laser detection itself, limit the experiment to a repetition rate of about $10\,\text{Hz}$. The data acquisition, scans and the bursts are controlled by the program KouDA [57].

3.2.2 Detecting Ammonia Molecules with (2+1) REMPI

Both beam lines are aligned perpendicular to each other and molecular packets are injected tangentially into the synchrotron at two different injection/detection points (see left side of Figure 3.3). The two packets from the two Stark decelerator beam lines are detected simultaneously using the same laser beam. In order to detect the molecules in the detection region, which corresponds to the gap between two hexapoles inside the molecular synchrotron, the molecular synchrotron needs to be turned off partially ('injection hexapoles off' in Figure 3.2). The setup is further described in the next Chapter. In this thesis deuterated ammonia is detected via $(2+1)$ resonantly enhanced multi-photon ionization (REMPI) [58]. The left side of Figure 3.3 shows schematically how the laser light is generated and the position at which the molecules are detected. A pulsed dye laser (PDL) manufactured by Sirah (PrecisionScan Dye Laser) pumped by a pulsed Nd:YAG laser (Spectra Physics [59]) produces a laser pulse around $634\,\text{nm}$ with *ca.* $90\,\text{mJ/pulse}$. The frequency of the laser pulse is doubled with a BBO crystal to $317\,\text{nm}$ with *ca.* $15\,\text{mJ/pulse}$. The ammonia molecules in the rovibrational ground state are ionized via the planar electronic $\tilde{B}^1 E''$ state in the vibrational $v_2 = 5$ mode with the resulting laser light:

$$|X^1 A'_1, v_2 = 1, J = 1, K = 1\rangle \rightarrow |\tilde{B}^1 E'', v'_2 = 5, J' = 3\rangle \rightarrow \text{ND}_3^+.$$

A lens with a focal length of $f = 500\,\text{mm}$ provides a sufficiently high power density for the two photon absorption at the detection point for beam line 1. To detect both beam lines simultaneously, the laser beam is reflected and refocused ($f = 125\,\text{mm}$) into the
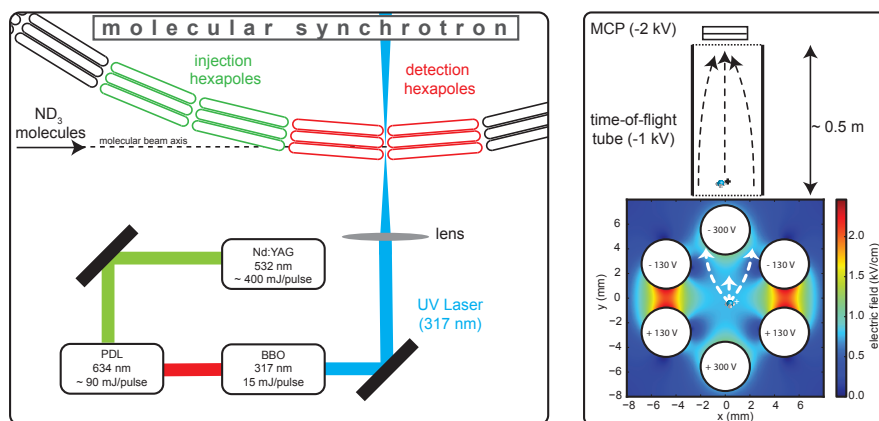
Figure 3.3: Detection Scheme. Left: A high power UV laser pulse (15 mJ/pulse – 5 ns duration) is generated by pumping a dye laser with a Nd:YAG laser at 532 nm and doubling the resulting frequency with a BBO crystal. The laser beam is focused in between two hexapoles of the synchrotron using a lens. The molecules are ionized by a $(2+1)$ REMPI scheme. In this way molecules can be detected at the injection point every time after they have completed one round trip.

Right: During the REMPI process extraction voltages are applied on the detection hexapoles. Positive ions experience an upward force and enter the time-of-flight tube. In the tube different masses drift apart and can be measured selectively by a multi channel plate (MCP) detector.

center of the synchrotron at the detection point for beam line 2. The ionized molecules are extracted by applying an appropriate voltage on the detection hexapoles such that ions drift upwards between two hexapole segments (right side of Figure 3.3). In a 50 cm long time-of-flight tube, kept on a potential of $-1\,\text{kV}$, ions with different mass drift apart such that the deuterated ammonia molecules are separated from ions of different mass [60]. These ions are detected on a micro channel plate (MCP). The measured ion signal is proportional to the molecular density at the detection point.

3.2.3 Injecting ND$_3$ Molecules into the Stark Decelerator

Figure 3.4 shows the ND$_3$ signal as a function of time delay between the opening of the valve and the switching sequence for both decelerator beam lines. The ion intensity is measured at the end of the beam line between the two detection hexapoles. In order to detect the molecules simultaneously with one laser pulse, beam line 2 is switched on earlier than beam line 1. Both decelerators operate with a phase angle of 60° and decelerate a packet of molecules from 281 m/s and 316 m/s to 124.3 m/s for beam line 1 and 2, respectively. The 60 mm long first hexapole is on high voltage for a flight distance of 42 mm such that the molecular packet is focused into the first stage of the Stark decelerator (see theoretical trajectories in Figure 2.8). As the valves used in the two beam lines are different (beam line 1 uses a solenoid-type General Valve [61], beam line
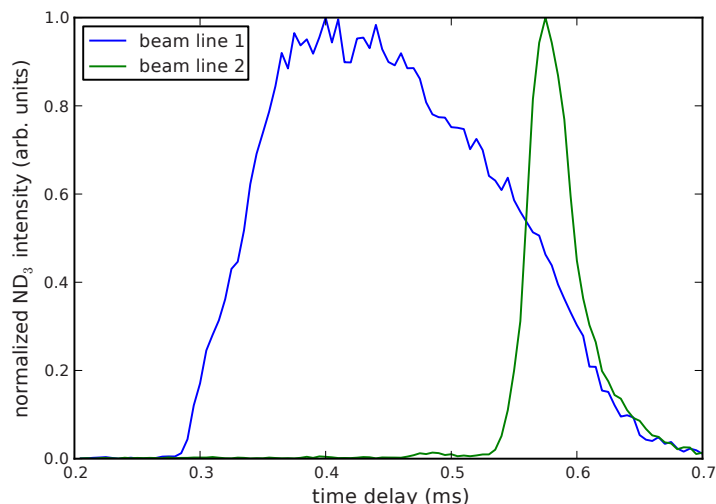
Figure 3.4: The normalized density of ND_3 molecules at the detection point as a function of time delay between the triggering of the valve and the start of the deceleration process. This measurement represents the density of molecules with the selected velocity at the entrance of the decelerator as a function of time. Beam line 1 (blue curve) uses a General Valve Series 99 which produces a long pulse of ND_3 molecules. Beam line 2 (green curve) uses a Jordan Valve which produces a short pulse of molecules. Compared to the General Valve the time when the decelerator is switched is more critical for the Jordan Valve. While the final velocity in both measurements is $124.3\,\mathrm{m/s}$ the initial velocity is $281\,\mathrm{m/s}$ and $316\,\mathrm{m/s}$ for the first and second beam line, respectively.

2 a Gentry-type Jordan Valve [62]) the spatial and velocity distribution differs: while the General Valve produces a spatially broad beam with a relatively narrow velocity distribution, the Jordan valve produces a spatially narrow packet with a wider velocity distribution [63]. At a constant phase angle ϕ only a narrow velocity distribution is accepted. By changing the time delay of the switching of the decelerator beam line relative to the gas ejection, the position spread of the molecular beam at the entrance of the decelerator (for the specific velocity accepted by the decelerator) is mapped out. The velocity spread can be measured in a time-of-flight experiment as described in the next Section (see Figure 3.5). The measurements shown in Figure 3.4 are normalized. The actual peak intensity of beam line 1 is about 15% higher than that arising from beam line 2.

3.2.4 Deceleration

Figure 3.5 shows a typical time-of-flight (TOF) measurement for the two decelerator beam lines. $t = 0\,\mathrm{ms}$ corresponds to the time when the synchronous molecule is decel-
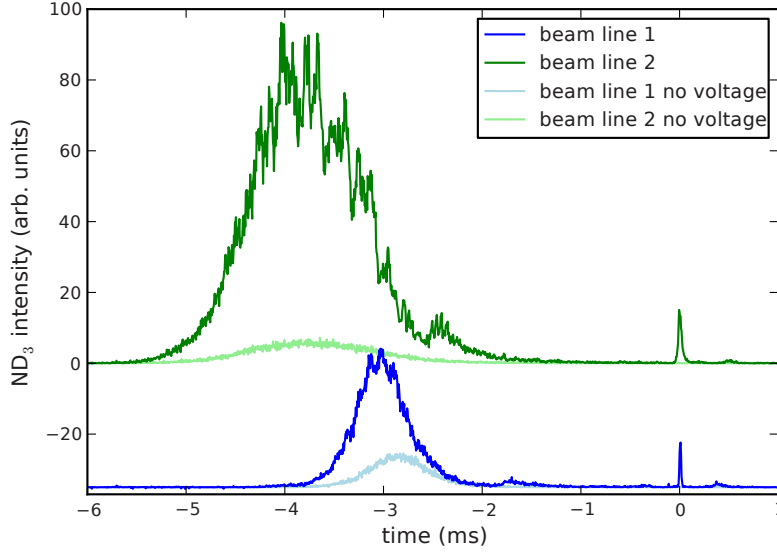
Figure 3.5: A time-of-flight (TOF) profile of ND_3 molecules in the detection region when both decelerator beam lines are operated such that the final velocity of the synchronous molecule is 124.3 m/s. Time $t = 0$ ms corresponds to the time when the synchronous molecule reaches the detection point. Beam line 1 (blue curve) is shorter than beam line 2 (green curve). After the release of the gas pulse the undecelerated molecules from beam line 1 reach the detection region earlier than for beam line 2. The light blue and the light green curve is the same measurement when no voltages are applied to beam line 1 and 2, respectively. All four individual measurements are on the same vertical scale.

erated to 124.3 m/s and reaches the detection point. The synchronous molecule has a velocity of 281 m/s and 316 m/s after the valve is triggered for beam line 1 (blue curve) and 2 (green curve), respectively. The two curves in light colors corresponds to the same measurement where no voltages were applied on both beam lines. With no electric fields present the divergent molecular beam of ND_3 molecules in the $|J, K\rangle = |1, 1\rangle$ state is almost not detectable (light green and light blue curve). The width of the peak is to a first approximation determined by the velocity spread after the expansion. When the electric fields are switched (dark lines) molecules in the low-field seeking $|J, MK\rangle = |1, -1\rangle$ state are decelerated, if they are inside the phase-space acceptance of the Stark decelerator. If they are outside of the acceptance, low-field seeking molecules experience only a transversal focusing force in the Stark decelerator and the focusing elements but on average they are neither accelerated nor decelerated. The undecelerated beam arrives in the detection region 3 ms and 4 ms earlier than the decelerated packet for beam line 1 and 2, respectively. This can be seen in Figure 3.5 as an increase in intensity of the undecelerated

part of the beam. Molecules in the high-field seeking state are deflected in the Stark decelerator and do not reach the detection zone. The packet of decelerated molecules is a pure sample of ND_3 molecules in the $|J,K\rangle = |1,1\rangle$ state, and has a width of 3 mm (4 mm) and a velocity distribution of few m/s in the longitudinal direction for beam line 1 (2).

3.2.5 Focusing Elements

Once the packet of molecules is decelerated, the three focusing elements (hexapole 2, buncher and hexapole 3) map the phase-space distribution of the molecular packet from the exit of the decelerator onto the acceptance of the molecular synchrotron. The exact time when each focusing element is switched on and off is critical. The switching of the focusing elements is not calculated in terms of time but rather in terms of effective distances and positions. For example, a hexapole is turned on for a time of Δt which corresponds to an effective length $\Delta z = \Delta t \cdot v_f$, positioned symmetrically around the effective position z. z is the distance from the skimmer, which is itself set to 0. This has the advantage that the velocity can be easily adjusted. All measurements in this Section show decelerated ammonia molecules that have a final velocity of $v_f = 124.3$ m/s.

Hexapole

Figure 3.6 presents the density of ND_3 molecules as a function of the effective length of hexapoles two and three. In this experiment the effective position of both hexapoles is kept constant. The variation of the effective length changes the position of the focal point. The optimal effective length for hexapole 2 is 10 mm and 8 mm for the first and second beam line, respectively. The third hexapole at both beam lines is on for 130 μs, corresponding to an effective length of 17 mm.

It is also possible to change the effective position of the transverse focusing lens by changing the time duration of the applied electric field. For the third hexapole this is shown in Figure 3.7. The 60 mm long third hexapole ends at 790 mm (beam line 1) and 990 mm (beam line 2 – see Table 3.2). The highest ND_3 intensity is measured when the effective position of the third hexapole is near the end of the hexapole. If the effective position is beyond the actual end of the hexapole, the effective length of the hexapole needs to be increased in order to focus the molecules into the detection region. This explains the observed curvature in the Figure.

Buncher

Figure 3.8 exemplifies the functionality of the buncher. The horizontal axis gives the time relative to the time at which the synchronous molecule is at the detection point. The vertical axis corresponds to the effective length of each buncher stage, which cannot be larger than the actual spatial length of a buncher stage (11 mm). To focus the beam longitudinally, each stage needs an effective length of 7.6 mm and 4.3 mm for beam line 1 and 2, respectively. Knowing the distances between the end of the decelerator and the buncher (L_1) and the distance between buncher and detection zone (L_2), one can
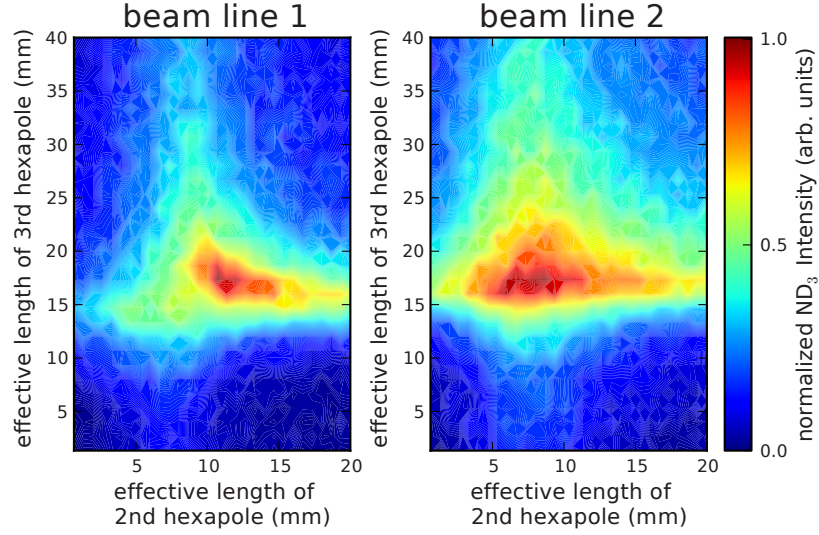
Figure 3.6: Experimentally measured ammonia density at the detection zone for both decelerator beam lines as a function of the effective focusing lengths of hexapole 2 and 3. After leaving the decelerator ND_3 molecules with a velocity of $124.3\,\mathrm{m/s}$ are focused with hexapole 2 at the entrance of the buncher. Hexapole 3 focuses the molecules at the detection region.

calculate the effective length of the buncher using Equation (2.17). In the buncher an ND_3 molecule experiences an averaged angular frequency ω, that is dependent on the effective length of the buncher. The averaged angular frequency ω is $(2\pi \cdot 370)\,\mathrm{rad/s}$ and $(2\pi \cdot 340)\,\mathrm{rad/s}$ for beam line 1 and 2, respectively. L_1 is $190\,\mathrm{mm}$ and $154\,\mathrm{mm}$, L_2 is $324\,\mathrm{mm}$ and $463\,\mathrm{mm}$ resulting in an effective time duration of $200\,\mu\mathrm{s}$ and $241\,\mu\mathrm{s}$, respectively for the first and second beam line. The predicted effective length of beam line 1 with three bunching stages is $8.2\,\mathrm{mm}$ per stage. For beam line 2 with nine bunching stages it is $3.4\,\mathrm{mm}$. For the first beam line the calculated value agrees well with the experimental data, while for beam line 2 the value differs slightly. We attribute this to the fact that the $110\,\mathrm{mm}$ long buncher can no longer be approximated as a thin lens.

In the experiments described in this thesis, the upper limit for the final velocity of a beam line is limited by the number of buncher stages. Currently the first beam line can only decelerate, bunch and focus molecules up to a velocity of $124.3\,\mathrm{m/s}$. By adding extra bunching stages to beam line 1 one can shift this limit to higher velocities. With nine stages the second beam line operates up to $225\,\mathrm{m/s}$.

The velocity of the molecular packet is determined by the exact switching sequence of the decelerator. The buncher is supposed to be switched symmetrically around the synchronous molecule such that the mean velocity of the packet is not changed (see
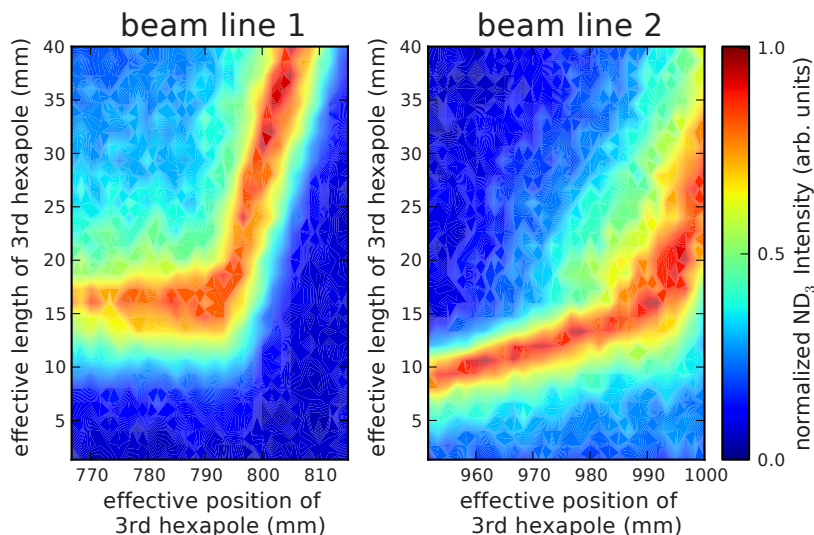
Figure 3.7: Experimentally measured ND_3 density at the detection point dependent on the effective length and position of the third hexapole. The burst sequence program can control how long the electric field is switched on (vertical axis) and the effective position of the third hexapole lens on the molecular beam axis (horizontal axis).

Section 2.6). For instance, if the effective position of the buncher is too small and the buncher is turned on too early, the molecular packet would be accelerated and arrive in the detection region earlier. Conversely, if the effective position is too large, the molecular packet would be decelerated and arrive later in the detection region. In Chapter 5 the molecular synchrotron itself will be used to determine the correct effective buncher and detection position.

3.3 Changing the Velocity of the Molecular Beam

The Stark decelerator, the buncher and the hexapole are elements used in the work presented in this thesis to create a state-selected beam of molecules which can be injected into the molecular synchrotron. An important goal of our work is to be able to scan the velocity of the beams. By changing the phase angle of the Stark decelerator, the final velocity of the molecular beam can be tuned. In order to focus molecules at this velocity at the injection point, the strength of the focusing elements needs to be adjusted.

A buncher, a hexapole and also the molecular synchrotron (see Section 4.4) have a characteristic focusing strength. If in a first approximation the force is linear, this
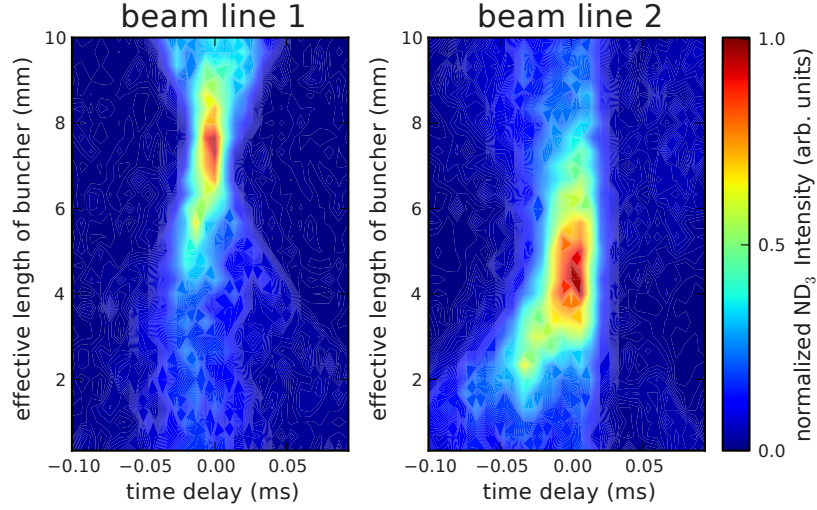
Figure 3.8: ND$_3$ density as a function of time and how long the buncher is switched on symmetrically around the synchronous molecule. 0 ms corresponds to the time when the synchronous molecule is detected. The effective length of the buncher cannot be longer than 11 mm because the spatial dimension of a buncher stage is exactly 11 mm.

strength is best described with the angular frequency ω (see Chapter 2).

$$\omega = \sqrt{\frac{k}{m}}, \tag{3.1}$$

where k is the harmonic force constant and m the mass. For a perfect hexapole, k is given by Equation (2.24). To keep the focusing effect of a molecular lens as general as possible, the lens focus is assumed to be in the $p-$direction. For a hexapole p is the radial direction, r, and for the buncher p is the longitudinal direction, z. For a fixed velocity v' the time duration $\Delta t'$ of each focusing element is found experimentally. If the distances of the beam before and after the focus are known (L_1 and L_2, respectively) one can calculate the angular frequency required to compensate the drift of the phase-space rotation [50].

$$\omega_p^2 = \frac{v'}{\Delta t'} \frac{L_1 + L_2}{L_1 L_2} \tag{3.2}$$

If a new velocity v is used, the new time duration Δt of this element is then

$$\Delta t = \frac{v}{\omega_p^2} \frac{L_1 + L_2}{L_1 L_2}. \tag{3.3}$$

focusing element	beam line 1	beam line 2	theoretical
hexapole 1	1350(30)	1480(30)	1420
hexapole 2	920(30)	1190(50)	920
buncher	380(30)	290(30)	380
hexapole 3	530(20)	460(20)	510/460
synchrotron	840		880

Table 3.3: Typical values for $\omega/(2\pi)$ in Hz for both decelerator beam lines. The experimental values for both beam lines (column 2 and 3) were obtained experimentally by measuring the effective length of the focusing elements and using Equations (3.2) and (4.4). The theoretical values were derived using Equation (2.5). The individual electric field were calculated with the finite element program Simion [64]. The theoretical frequency of hexapole 3 has two different values since the two hexapoles are operated with two different voltages (see Section 3.2.1). 530 Hz corresponds to beam line 1 and 460 Hz to beam line 2. For the molecular synchrotron the voltage difference was 6 kV. The error for the experimental data is given in the brackets.

Note that, if the velocity changes and the voltage applied to the synchrotron is kept constant, the equilibrium orbit inside the synchrotron changes. This will be discussed in Chapter 4. For different focusing elements the values for $\omega/(2\pi)$ are specified in Table 3.3. Next to the experimental values for beam line 1 and 2 theoretical values are listed. The electric field was determined using the finite element program Simion [64]. Using Equation (2.5) the Stark energy, the force and the resulting angular frequency were calculated. In Table 3.3 the averaged values are given.

In Figure 3.9 the final velocity of the molecular packet is tuned from 90 to 140 m/s for both decelerator beam lines simultaneously. The final velocity is changed by selecting a
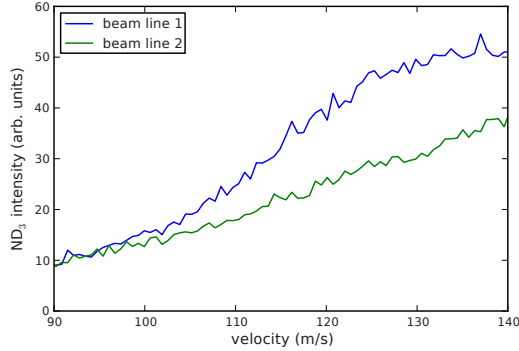
Figure 3.9: ND_3 density at the detection point as a function of final velocity for beam line 1 and 2. For each point in this measurement a burst sequence was calculated in which the Stark decelerator had a different final velocity and for which the effective focusing strength of hexapole and buncher was adjusted accordingly.

different starting velocity in front of the Stark decelerator and leaving the phase angle of $\phi = 60°$ constant. Experimentally it was found that the decelerator works best for this particular phase angle which is also in agreement with numerical calculations from van de Meerakker *et al.* [47]. All three focusing elements behind the decelerator are scaled according to Equations (3.2) and (3.3). Each point in this measurement corresponds to an appropriate burst sequence in which the correct switching sequence was applied and where the signal was averaged over 50 shots. The ND_3 intensity becomes smaller for slower velocities because of two effects: Firstly, the molecular spread (transverse and longitudinal) is inversely proportional to the forward velocity [50]; for lower speeds a smaller part of the beam falls inside the aperture and is refocused. Secondly, the number of molecules in the molecular beam that is injected in the decelerator decreases with lower starting velocity.

Chapter 4

Confining Neutral Molecules in a Synchrotron

4.1 Introduction

The previous Chapter described in detail the operation of the experimental apparatus to produce a pure molecular beam of quantum state selected ND_3 molecules with a tunable velocity. This Chapter focuses on the molecular synchrotron itself. While the experimental setup is described in detail in Chapter 5, the equations of motion for molecules inside the molecular synchrotron are derived in this Chapter. Two Stark decelerator beam lines inject packets of molecules tangentially into the molecular synchrotron. The molecular synchrotron serves to confine multiple packets of molecules transversely and longitudinally in tight bunches. The first Section explains the characteristic frequencies in the molecular synchrotron. The second and the third Sections describe the *moving* potential well in the transverse and longitudinal direction, respectively. The synchrotron developed in our laboratory and described in this thesis consists of forty straight hexapole segments. The fourth Section will described why forty hexapole segments were chosen and to which extend the deviation from a circle influences the molecular trajectories. At the end of this Chapter the trajectory calculation of the molecular synchrotron is described in detail.

Figure 4.1 shows a schematic of the molecular synchrotron. It consists of forty small straight hexapoles which are aligned on a circle with a diameter of half a meter. Neighboring hexapoles are separated by a $2\,\mathrm{mm}$ gap. Each hexapole segment has an inner radius of $r_0 = 3.54\,\mathrm{mm}$. The electrodes have a radius of $R_{\mathrm{hex}} = 2\,\mathrm{mm}$, such that the ratio of R_{hex}/r_0 is 0.565, which is (according to Anderson) a good approximation to an ideal hexapole field using cylindrical rods [52]. In order to maintain a constant gap of $2\,\mathrm{mm}$ between two neighboring hexapole segments, electrodes in each hexapole segment are longer on the outside and shorter on the inside. The position of the molecule, $\boldsymbol{r}$, is best described with the three coordinates ϕ, r' and y'. ϕ is the angle of the molecule in the x-z-plane relative to the detection point of the first beam line (between the two red hexapole segments of the first beam line on the top Panel of Figure 4.1). r' is the radial coordinate and y' the vertical coordinate with respective to the center of the hexapole.
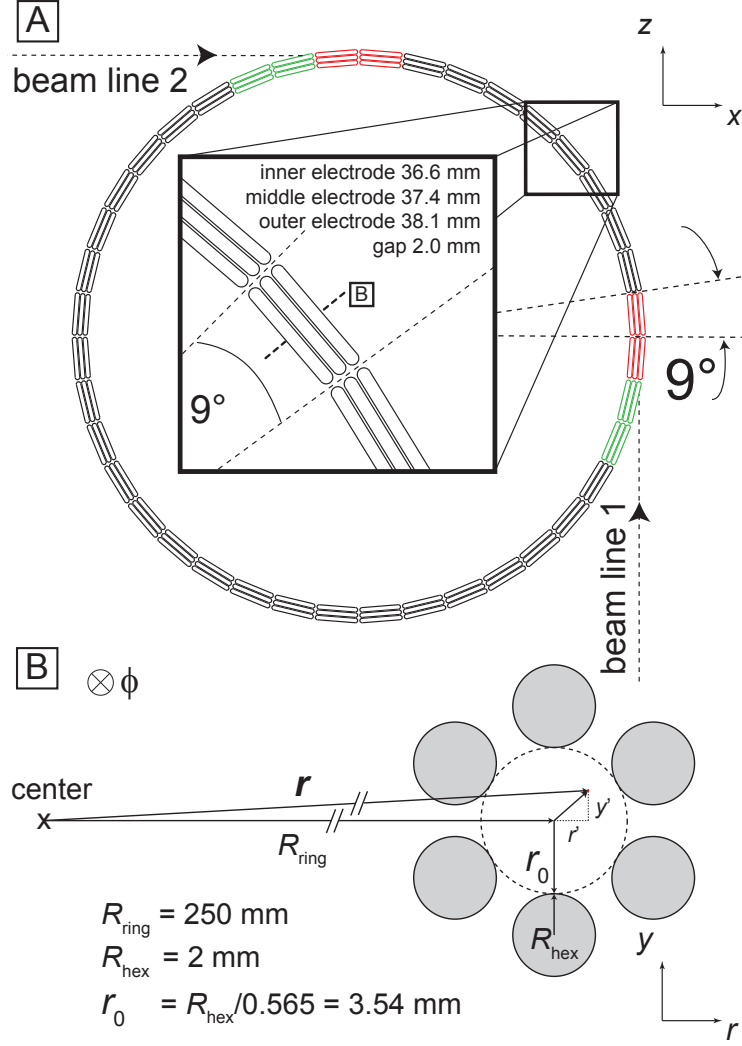
Figure 4.1: A schematic of the molecular synchrotron. The top Panel (A) shows a top view of the forty straight hexapoles aligned onto a circle with a radius of 250 mm. Two Stark decelerator beam lines inject packet of molecules tangentially at two positions in the synchrotron. For this purpose, each beam line needs to turn off two incoupling (green) and two detection (red) hexapoles (see Section 5.7). The angle between each hexapole is 9°. The inset shows a detailed view of a hexapole segment. To assure a constant gap of 2 mm the electrode rods have different lengths. The lower Panel (B) shows the cross section inside a hexapole segment. Following Anderson [52], the ratio between the rod radius R_{hex} and the inner radius of the hexapole r_0 is given as 0.565.
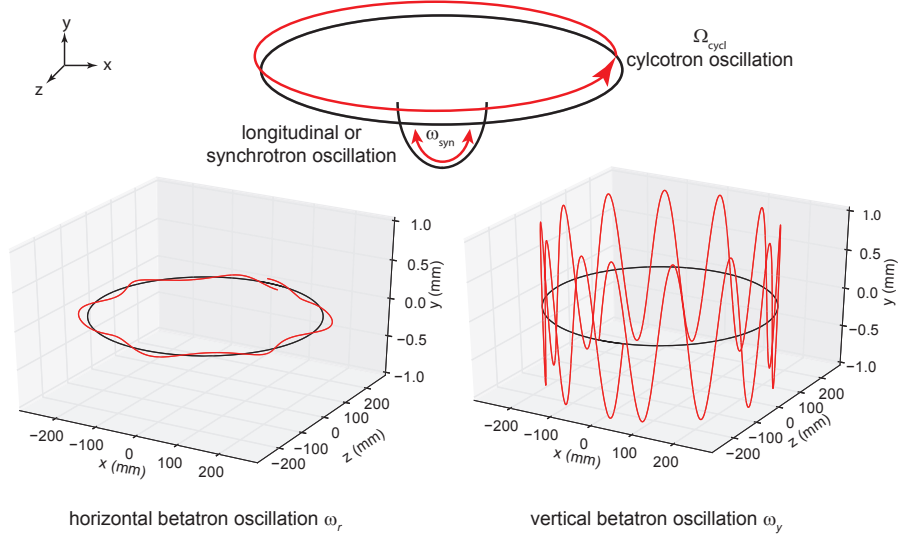
Figure 4.2: A simplified schematic of the different oscillation types that a molecule experiences in the molecular synchrotron. The black curve represents the trajectory of the synchronous molecule (equilibrium orbit). The red curve is a trajectory of a molecule with an exemplary oscillation. The upper part shows the cyclotron frequency Ω_{cycl}, which is 2π over the time that the synchronous molecules needs to complete one full round trip. The synchrotron frequency ω_{syn} is the oscillation frequency in the longitudinal direction. The lower Panel shows the two transverse oscillations. On the left is the horizontal betatron oscillation ω_r and on the right the vertical betatron oscillation ω_y.

4.2 Characteristic Frequencies

In a synchrotron, the motion of the molecular packet is best described by four characteristic frequencies which are sketched schematically in Figure 4.2. The black trajectory shows the synchronous molecule, which is by definition on a closed orbit. In red the possible oscillations are shown. The cyclotron frequency f_{cycl} is the inverse of the time that the molecule needs to complete one full round trip (round trip time). The angular cyclotron frequency is

$$\Omega_{\mathrm{cycl}} = \frac{2\pi}{t_{\mathrm{rt}}}. \tag{4.1}$$

With an equilibrium orbit of $2\,\mathrm{mm}$ (to be derived in next the Section) and a forward velocity of $124.3\,\mathrm{m/s}$, $\Omega_{\mathrm{cycl}}/(2\pi)$ is $78\,\mathrm{Hz}$.

While the cyclotron frequency describes the velocity of the traveling potential well, molecules will oscillate in all three directions within this moving frame. In the longitudinal direction the oscillation is referred to as the synchrotron oscillation with an angular frequency of ω_{syn} (sketched in the upper Panel). In the transverse direction the two types are called betatron oscillations; in the horizontal plane the angular frequency is referred

as ω_r (lower left Panel) and in the vertical plane it is ω_y (lower right Panel). Characteristic frequencies are derived in the following Sections and are summarized in Table 4.1 for a fixed velocity and confining voltage difference. Experimentally the characteristic frequencies are measured in Chapters 5 and 6. To avoid confusion the characteristic frequency is always given as a frequency, and not as an angular frequency.

type	angular frequency	frequency
cyclotron frequency Ω_{cycl}	493 rad/s	78 Hz
synchrotron frequency ω_{syn}	364 rad/s	58 Hz
horizontal betatron frequency ω_r	5523 rad/s	879 Hz
vertical betatron frequency ω_y	5390 rad/s	858 Hz

Table 4.1: Characteristic frequencies for the molecular synchrotron with a forward velocity of 124.3 m/s and a confining voltage difference of 6 kV, obtained in Section 4.3 and Section 4.4.

4.3 Transversal Confinement

In a perfect hexapole that is bent into a torus – like the first storage ring for neutral molecules [65] – the centrifugal force is balanced by the radial component of the hexapole field (see Equation (2.25))

$$\frac{mv_\phi^2}{R_{\mathrm{ring}} + r'} = \frac{kr'}{\sqrt{1 + \left(\frac{W_{\mathrm{inv}}}{k(r'^2+y'^2)}\right)^2}}. \tag{4.2}$$

Here, v_ϕ is the longitudinal velocity of the molecule in the synchrotron. The position where the two forces cancel each other is referred to as the radial equilibrium orbit, r'_{equi}. In the vertical direction the force of gravity needs to be compensated.

$$-mg = \frac{ky'}{\sqrt{1 + \left(\frac{W_{\mathrm{inv}}}{k(r'^2+y'^2)}\right)^2}}. \tag{4.3}$$

In analogy to the radial equilibrium orbit, there is also a vertical equilibrium orbit, y'_{equi}. The inversion splitting in deuterated ammonia is small compared to $k\left(r'^2 + y'^2\right)$ such that Equations (4.2) and (4.3) can be rewritten as

$$r'_{\mathrm{equi}} = \frac{R_{\mathrm{ring}}}{2}\left[\sqrt{1 + \left(\frac{2v_\phi}{R_{\mathrm{ring}}\omega}\right)^2} - 1\right] \approx \frac{v_\phi^2}{R_{\mathrm{ring}}\omega^2} \tag{4.4}$$

and

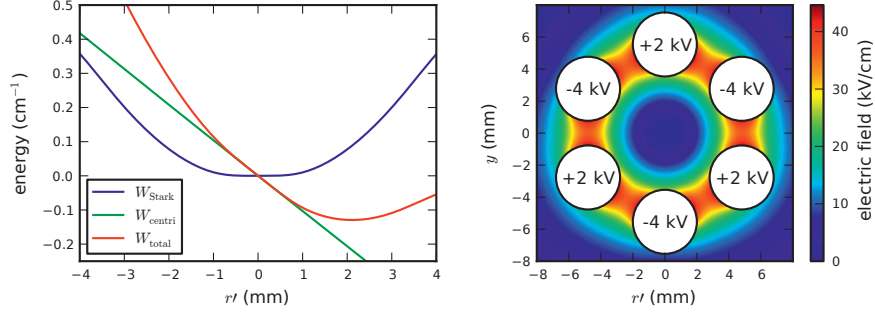$$y'_{\mathrm{equi}} \approx -\frac{g}{\omega^2} \tag{4.5}$$

Figure 4.3: Left Panel: The Stark energy W_{Stark} is shown for an ND$_3$ molecule in the low-field seeking $|J, MK\rangle = |1, -1\rangle$ state as a function of displacement from the hexapole center (blue curve) ($y' = 0$ mm). With a forward velocity of 124.3 m/s the molecule finds itself inside the molecular synchrotron in a centrifugal pseudo-potential W_{centri} (green curve). The sum of the two energies is the effective potential energy W_{total} (red curve) that the molecules experience transversally ($W_{\text{total}} = W_{\text{Stark}} + W_{\text{centri}}$). Right Panel: Electric field configuration together with the cross section of one hexapole segment.

with an angular frequency given by

$$\omega = \sqrt{\frac{k}{m}}. \tag{4.6}$$

The last approximation in Equation (4.4) is valid if $2v_\phi \ll R_{\text{ring}}\omega$.

In the molecular synchrotron the angular frequency $\omega/(2\pi)$ of deuterated ammonia in the low-field seeking $|J, K\rangle = |1, 1\rangle$ state is 880 Hz, if the applied voltage difference is 6 kV and the inversion splitting is neglected. The electric field configuration can be seen in the right hand Panel of Figure 4.3. With a forward velocity of 124.3 m/s the radial equilibrium orbit is $r'_{\text{equi}} = 2.0$ mm and the vertical equilibrium orbit is $y'_{\text{equi}} = 0.32\,\mu$m. The small gravitational distortion justifies the neglect of the effect of gravity hereafter. If the anharmonicity of the electric field and the inversion splitting is taken into account, the radial equilibrium orbit changes to 2.1 mm. The change in the vertical equilibrium orbit is negligible.

The synchrotron is best described in the form of its phase-space acceptance in all three dimensions: longitudinal, radial, and vertical. Let us first consider the radial direction.

Radial Direction The effective potential energy W_{total} that a molecule experiences in the molecular synchrotron is the sum of the potential Stark energy W_{Stark} and the pseudo-potential energy of the centrifugal force, W_{centri}. By integrating the left side of Equation (4.2) over dr', the pseudo-potential can be written as

$$W_{\text{centri}} = -mv_\phi^2 \ln\left|1 + \frac{r'}{R_{\text{ring}}}\right|. \tag{4.7}$$

Neglecting the inversion splitting, the resulting potential is

$$W_{\text{total}} = \frac{1}{2}kr'^2 - mv_\phi^2 \ln\left|1 + \frac{r'}{R_{\text{ring}}}\right|. \tag{4.8}$$

The left Panel of Figure 4.3 shows the resulting three potential energy curves (the anharmonicities of the electric field and the inversion splitting are included). The forward velocity is $124.3\,\text{m/s}$. If the velocity of the molecular packet is changed, the pseudo-potential energy of the centrifugal force changes (tilt of the green curve). With increasing velocity, the tilt of the pseudo-potential becomes steeper and the effective total potential energy (red curve) becomes shallower and has its minimum (equilibrium orbit) further from the hexapole center. To maintain an attractive potential well of constant depth and position, the angular frequency of the motion of the ND_3 molecules needs to be changed in accordance with the velocity of the molecular packet. The easiest way to achieve this is to adjust the voltage which is applied to the hexapole electrodes.

The maximum radial position r_{max} at which molecules are still confined in the synchrotron is [25]

$$r_{\text{max}} = r_0 - r'_{\text{equi}}. \tag{4.9}$$

Assuming a linear restoring force, the corresponding maximum transverse velocity v_r which is still accepted inside the synchrotron is

$$v_{r,\text{max}} = \omega r_{\text{max}} \approx \omega\left(r_0 - \frac{v_\phi^2}{R_{\text{ring}}\omega^2}\right). \tag{4.10}$$

With a forward velocity of $124.3\,\text{m/s}$ and a voltage difference of $6\,\text{kV}$ a maximum transverse velocity of $8.4\,\text{m/s}$ is accepted in the synchrotron. The right side of Figure 4.4 shows the maximum transverse velocity $v_{r,\text{max}}$ as a function of forward velocity v_ϕ. The red curve assumes a perfect hexapole and was calculated using Equation (4.10) at a constant frequency of $879\,\text{Hz}$. The potential energy of the molecule with and without the inversion splitting was derived using the electric field calculated using Simion [64], for the blue and the green curve respectively. The energy difference ΔW between the equilibrium position r_{equi} and the hexapole radius r_0 was used to determine the maximum transverse velocity $v_{r,\text{max}}$

$$v_{r,\text{max}} = \sqrt{\frac{2\Delta W}{m}} = \sqrt{\frac{2}{m}\left(W(r_0) - W(r'_{\text{equi}})\right)}. \tag{4.11}$$

The left Panel of Figure 4.4 shows the variation of the angular frequency ω_r as a function of the radial position. For comparison, the red curve shows that for an ideal hexapole with $W_{\text{inv}} = 0$ and a voltage difference of $6\,\text{kV}$, with the frequency held constant at $879\,\text{Hz}$. Using the electric field from Simion and neglecting the inversion splitting (green curve) the angular frequency decreases significantly at larger radii due to the non-linear effects close to the electrodes. With the inversion splitting present (blue curve), the angular frequency decreases towards the hexapole center. The linear term in the Stark effect becomes less dominant in the region of low electric fields and the non-linear
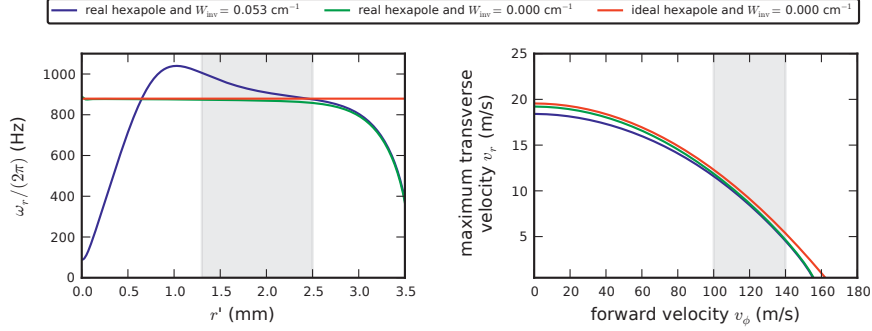
Figure 4.4: The left Panel shows the angular frequency ω_r as a function of radial position r for three different configurations: The blue curves correspond to calculations in which the inversion splitting was taken into account and the hexapole field was calculated with a finite-element program [64]. For the green curves the inversion splitting was set to zero. The red curves used the electric field of an ideal hexapole and neglected the inversion splitting $(\omega/(2\pi) = 879\,\mathrm{Hz})$. In the experiment $\omega/(2\pi)$ is of the order of $890 - 1000\,\mathrm{Hz}$. The right Panel shows the maximum transverse velocity a molecule can have and still be confined transversally in the synchrotron. The shaded region in the right Panel shows the velocity range normally used in the molecular synchrotron. In the left Panel the range of frequencies under operating conditions is shown $(100 - 140\,\mathrm{m/s}$ corresponding to a frequency of $890 - 1000\,\mathrm{Hz})$.

effects become stronger. It should be mentioned that if the potential is not harmonic ω is not well defined. In Figure 4.4 the gray shaded region corresponds to the velocity range that was used in this thesis. $100 - 140\,\mathrm{m/s}$ corresponds to a frequency of 890-$1000\,\mathrm{Hz}$, and a maximum radial position of $r_{\max} = 1.0 - 2.2\,\mathrm{mm}$. With $v_{r,\max} = r_{\max} \cdot \omega_r$ the maximum accepted transverse velocity is $12\,\mathrm{m/s}$ for $100\,\mathrm{m/s}$ and $7\,\mathrm{m/s}$ for $140\,\mathrm{m/s}$.

Vertical Direction The vertical oscillation frequency ω_y is determined in a similar fashion. The vertical potential energy is dependent on the equilibrium orbit and thus on the longitudinal velocity. Knowing the equilibrium orbit, the vertical potential energy can be fitted at r'_{equi} to an harmonic function. From the force constant k the angular frequency is calculated using Equation (4.6). At a velocity of $124.3\,\mathrm{m/s}$ ω_y is $860\,\mathrm{Hz}$. For a velocity of 100 and $140\,\mathrm{m/s}$ the frequency is 830 and $880\,\mathrm{Hz}$, respectively. In analogy with Equation (4.9) the maximum vertical position a molecule can have without being lost from the synchrotron is

$$y'_{\max} = \sqrt{r_0^2 - r'^2_{\mathrm{equi}}}. \tag{4.12}$$

For $124.3\,\mathrm{m/s}$ $y'_{\max}$ is $2.5\,\mathrm{mm}$. The maximum vertical velocity $v_{y,\max}$ is

$$v_{y,\max} = \sqrt{\frac{2}{m}\left(W(r'_{\mathrm{equi}}, y_{\max}) - W(r'_{\mathrm{equi}}, 0)\right)}. \tag{4.13}$$

For a longitudinal velocity of $124.3\,\mathrm{m/s}$ the maximum vertical velocity is $15.3\,\mathrm{m/s}$. This value can also be obtained by $v_{y,\max} = \omega_y \cdot y'_{\max}$.
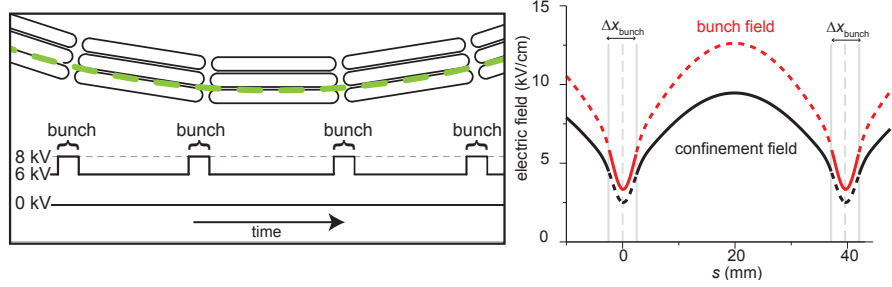
Figure 4.5: Left Panel: Scheme of the time dependence of the voltage difference between adjacent hexapole electrodes during operation of the synchrotron. By temporarily switching to a higher voltage difference whenever the packet passes through a gap, ammonia molecules are kept in a tight bunch while revolving. The green dashed curve indicates the equilibrium orbit with a forward velocity of $124.3\,\text{m/s}$. Right Panel: Electric field strength (both for confinement and bunching) as a function of position along the equilibrium orbit. The origin of the horizontal axis s is the midpoint between two hexapole segments.

All equations derived in this Section assume that the equilibrium orbit is on a perfect circle. However, due to the straight hexapole parts and the gap between two hexapole segments the exact equilibrium orbit varies. Nevertheless, numerical calculations show that the deviations because of this are small. See Section 4.5 for more detail.

4.4 Longitudinal Confinement

The previous Section shows that molecules are confined transversally (in the y- and r-direction) by applying a constant voltage on a hexapole torus. This Section discusses how to confine a molecular packet in the longitudinal direction in a tight bunch. The left side of Figure 4.5 shows a schematic of the time-dependent switching scheme. The electric field is switched synchronously with the revolving packet in the synchrotron between the confinement field and the so-called bunching field (the electric field is 4/3 times stronger). This time-dependent switching is the eponym of the molecular synchrotron. On the right side of Figure 4.5 the electric fields for the confinement and the bunching configuration are shown as a function of position along the equilibrium orbit (dashed green line on the left Panel) in black and red, respectively. For a time duration Δt_{bunch} the electric field is switched to the bunching configuration every time the synchronous molecule is in the gap region. As in Section 3.2.5, this time is described as an effective bunching length Δx_{bunch}, which is determined by the fixed final velocity v_f of the Stark decelerator beam line.

$$\Delta x_{\text{bunch}} = v_f \Delta t_{\text{bunch}}. \tag{4.14}$$

In Figure 4.6 the operation principle of the longitudinal bunching scheme is described in more detail. It is similar to that of the buncher in the decelerator beam line. The upper Panel shows the potential energy of the $|J, MK\rangle = |1, -1\rangle$ state as a function of
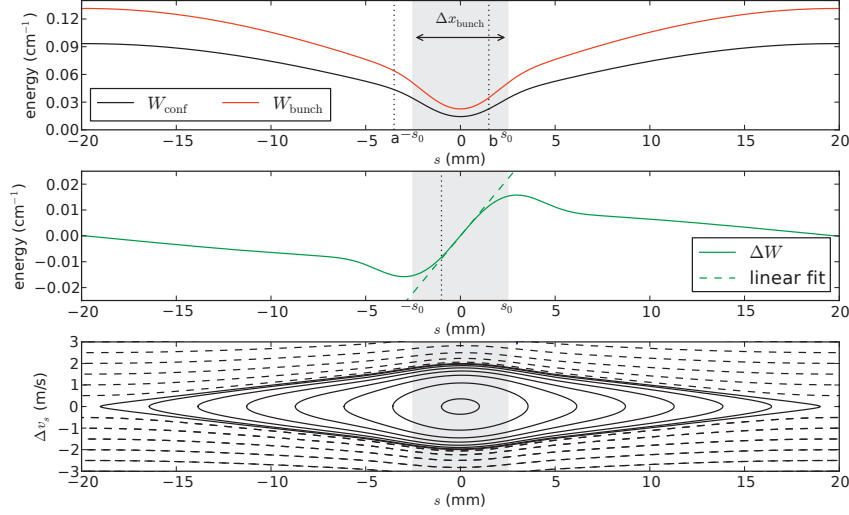
Figure 4.6: The upper Panel shows the potential energy of an ammonia molecule in the $|J, MK\rangle = |1, -1\rangle$ state as a function of longitudinal position along the equilibrium orbit. The potential of the confinement and bunching field is shown in black and red, respectively. The origin of the horizontal axis corresponds to the center of a gap between two hexapole segments. In the gray shaded region the synchronous molecule experiences the bunching field. The effective length Δx_{bunch} is 5 mm and is symmetric around the gap region. The middle Panel shows the change in potential energy as a function of position. A molecule that is behind the synchronous molecule (left dotted line) experiences a negative change in potential energy and will be pushed towards the synchronous molecule. The restoring force for a molecule is approximately linear for a length of 5.0 mm. Near the synchronous molecule the slope of ΔW is $8.8\,\text{cm}^{-1}/\text{m}$. The lower Panel shows the phase-space diagram in the longitudinal direction. The solid lines correspond to molecules that are stably bunched while trajectories in dashed lines are not stably bunched.

longitudinal position along the equilibrium orbit for the two switching configurations. The confinement field corresponds to the black and the bunching field to the red curve. Let us first consider the motion of the synchronous molecule along the equilibrium orbit in the confinement configuration. If the electric field is not switched, it will loose potential energy and gain kinetic energy as it moves along the electric fringe fields in the gap region. After passing the middle of the gap, the synchronous molecule will regain all the potential energy it lost and will have the same kinetic energy as before the gap. If now the electric field is switched from the confinement field to the bunching field for an effective length Δx_{bunch} symmetrically around the synchronous molecule (gray shaded region), the synchronous molecule will gain and lose a larger amount of kinetic energy. After the switching process the velocity of the synchronous molecule still remains unchanged.

The change in potential energy ΔW depends on the longitudinal position s of the molecule along the equilibrium orbit as the field is switched to the bunching configuration.

$$
\begin{aligned}
\Delta W(s) = {} & (W_{\text{bunch,a}}(s) - W_{\text{conf,a}}(s)) \\
& - (W_{\text{bunch,b}}(s + \Delta x_{\text{bunch}}) - W_{\text{conf,b}}(s + \Delta x_{\text{bunch}}))
\end{aligned}
\tag{4.15}
$$

If $\pm s_0$ is the position of the synchronous molecule when the field is switched to the bunching and confining configuration, respectively, the change in energy can be written with

$$
\Delta x_{\text{bunch}} = 2s_0
\tag{4.16}
$$

as

$$
\begin{aligned}
\Delta W(s) = {} & (W_{\text{bunch,a}}\left(-s_0 + \Delta s\right) - W_{\text{conf,a}}\left(-s_0 + \Delta s\right)) \\
& - (W_{\text{bunch,b}}\left(s_0 + \Delta s\right) - W_{\text{conf,b}}\left(s_0 + \Delta s\right))
\end{aligned}
\tag{4.17}
$$

with

$$
s = -s_0 + \Delta s.
\tag{4.18}
$$

For a fixed initial velocity, ΔW is shown in the middle Panel of Figure 4.6. The horizontal axis shows the position of a molecule. The synchronous molecule ($\Delta s = 0$) is in the center of the gray region and will not change its kinetic energy during the switching process. A molecule that is, *e.g.*, – in position – behind the synchronous molecule (dotted line) experiences a stronger acceleration than deceleration in the gap and will gain kinetic energy. Consequently, it will be pushed towards the synchronous molecule. Conversely, a molecule that was in front of the synchronous molecule will be decelerated and pushed back towards the synchronous molecule.

The average longitudinal force $\overline{F}$ that a molecule experiences while passing a hexapole segment of length ΔL can be expressed as

$$
\overline{F} = -\frac{\Delta W(s)}{\Delta L}.
\tag{4.19}
$$

For molecules close to the synchronous molecule (Δs is small), the restoring force is linear and the force can be written as

$$
\overline{F} = -\frac{\Delta W'(s)\Delta s}{\Delta L},
\tag{4.20}
$$

with $\Delta W'(s)$ being the slope of the potential difference. $\Delta W'(s)/\Delta L$ is the harmonic force constant k. The corresponding longitudinal angular frequency is

$$
\omega_{\text{syn}} = \sqrt{\frac{\Delta W'}{m\Delta L}}.
\tag{4.21}
$$

The green dashed line in the middle Panel of Figure 4.6 shows a linear fit of the potential difference ΔW. The slope is $8.8\,\text{cm}^{-1}/\text{m}$. The length of an hexapole segment $\Delta L = 2\pi(R_{\text{ring}} + r_{\text{equi}})/40$ is $39.6\,\text{mm}$ and results in $\omega_{\text{syn}}/(2\pi) = 58\,\text{Hz}$.

With an effective bunching length of $5\,\mathrm{mm}$, a velocity range of $\Delta v = 1.8\,\mathrm{m/s}$ can be stably confined. The phase-space plot in the lower Panel of Figure 4.6 is calculated using the potential in the longitudinal direction (middle Panel) and the resulting average force. In the harmonic part of the well (inner solid circle) the synchrotron frequency is $60\,\mathrm{Hz}$.

4.5 Transverse Stability

The circular structure of the molecular synchrotron is approximated by forty linear hexapoles. The question might arise why forty hexapoles and not more or less.[1] To justify this number the process of motional resonances needs to be explained. Imperfections in a perfect circular structure lead to transverse loss processes as the molecules experience a periodic deviation in the restoring force. This phenomenon is well known in particle accelerators [66] and was already investigated for polar molecules in the previous molecular synchrotron [67]. These motional resonances occur if the number of transverse oscillations per round trip is either a half integer or whole integer value. The betatron tune ν is defined as the number of transverse oscillations per round trip, and has a radial and vertical component.

$$\nu_r = \frac{\omega_r}{\Omega_{\mathrm{cycl}}} \quad \text{and} \quad \nu_y = \frac{\omega_y}{\Omega_{\mathrm{cycl}}}. \tag{4.22}$$

Primarily, Ω_{cycl} depends on the velocity of the molecular packet and $\omega_{r,y}$ on the applied voltage. The betatron tune leads to a velocity- and voltage-dependent characteristic region for the molecular synchrotron in which the molecules are not stably transversely confined. In keeping with the terminology used in particle physics the unstable regions are called 'stop bands' [66]. Under the assumption that the molecule experiences only a linear Stark effect inside a perfect hexapole field, the betatron tune in the radial and vertical direction is given by

$$\nu_{r,y} = \frac{\sqrt{k_{r,y}/m}}{2\pi v_f / (R_{\mathrm{ring}} + r_{\mathrm{equi}})} = \frac{R_{\mathrm{ring}} + r_{\mathrm{equi}}}{v_f} \sqrt{\frac{3\mu_{\mathrm{eff}}V}{mr_0^3}}. \tag{4.23}$$

Forty Segments Make Almost a Good Circle   The efficiency of a molecular synchrotron is best described by its phase-space acceptance A. It corresponds to the volume in phase-space in which molecules are stably confined. It is again convenient to use the three relative coordinates r, y and s. In the horizontal direction the 2D-area is

$$A_r = \pi r_{\mathrm{max}} v_{r,\mathrm{max}} = \pi\omega \left(r_0 - r_{\mathrm{equi}}\right)^2. \tag{4.24}$$

For an ideal hexapole this can be written as

$$A_r = \pi\omega \left(r_0 - \frac{v_f^2}{R_{\mathrm{ring}}\omega^2}\right). \tag{4.25}$$

---

[1]This question was addressed in the thesis of C. E. Heiner [26]. Her analysis is partly reproduced here.
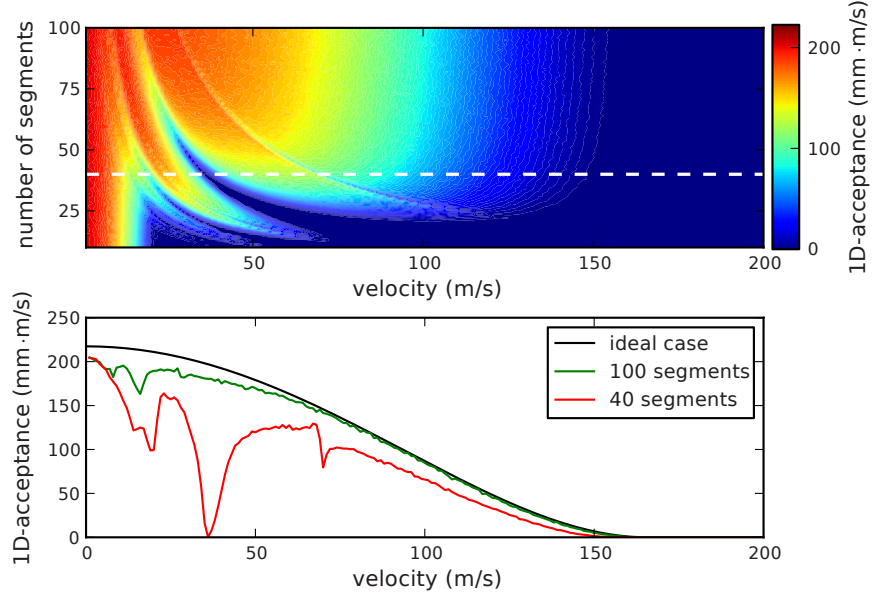
Figure 4.7: Upper Panel: The numerically calculated phase-space acceptance of a molecular synchrotron as a function of forward velocity and number of straight segments. The frequency was set to 879 Hz and only the horizontal betatron motion was considered. Forty hexapole segments are marked with a horizontal dashed white line. Lower Panel: The phase-space acceptance for a selected number of segments. In red a synchrotron consisting of forty hexapoles is shown, in green for 100 segments. The ideal case (black curve) is calculated using Equation (4.25).

The upper Panel in Figure 4.7 shows the result of a trajectory calculation, in which 20,000 molecules flew in a molecular synchrotron for 200 ms with a tunable velocity, changing the number of linear segments. The radius of the molecular synchrotron is half a meter and each hexapole segment is linear and has an inner radius r_0 of 3.54 mm. The force on a molecule inside a hexapole segment n is assumed to be perfectly linear with a fixed frequency of 879 Hz and a force constant of

$$k = m\omega^2. \tag{4.26}$$

The position of a molecule inside the molecular synchrotron in the x-z-plane is described with the angle ϕ which necessitates a coordinate transformation to the laboratory frame (see Figure 4.1)

$$\sin\phi = \frac{z}{r} = \frac{z}{\sqrt{x^2 + z^2}}. \tag{4.27}$$

A molecule is in the straight hexapole segment n, if the following condition is fulfilled

$$\frac{n-1/2}{n_{\mathrm{seg}}} < \frac{\phi}{2\pi} < \frac{n+1/2}{n_{\mathrm{seg}}}, \tag{4.28}$$

in which n_{seg} is the number of total segments. This model assumes that there are no gaps between individual straight parts. A molecule is transversely lost, if the molecule is outside of the inner radius of the hexapole

$$r_0 < \sqrt{y'^2 + r'^2}. \tag{4.29}$$

The fraction of molecules that remain inside the molecular synchrotron after $200\,\mathrm{ms}$ is divided by the initial phase-space distribution to obtain the phase-space acceptance A. To ensure that the packet is larger than the acceptance, the initial position spread of the random packet is chosen to be $8\,\mathrm{mm}$ and the initial velocity spread is $40\,\mathrm{m/s}$. Each point in the upper Panel of Figure 4.7 determines the one dimensional phase-space acceptance as a function of the number of segments and velocity. Clearly, the more straight segments are used to complete a circular molecular synchrotron, the less dominant are the motional resonances. In other words, the higher the symmetry of the synchrotron (number of straight segments) the fewer motional resonances occur. The black curve in the lower Panel of Figure 4.7 shows the acceptance for a perfect ring symmetry and was calculated using Equations (4.4) and (4.25). The green curve shows the simulated acceptance for 100 segments. Only for velocities below $50\,\mathrm{m/s}$ does it differ from the ideal case. The red curve shows the transverse stability for 40 segments. From this graph it was decided to build the current 40 segment molecular synchrotron that gives a compromise between transversal acceptance and construction efforts. The calculation in Figure 4.7 assumes that every hexapole is perfectly aligned and the same voltage difference is applied. In reality the geometry between different hexapole segments might differ or the voltage difference applied might not be identical. These effects would lead to a deviation in the restoring force, and hence more regions of instability. In the characterization of the molecular synchrotron these other stop bands will be analyzed.

4.6 Trajectory Simulation

In a trajectory calculation the motion of the molecules inside the molecular synchrotron is simulated. The benefit of these calculations is that experimental measurements can be reproduced and confirmed. The simulations also enable an unique way of understanding the motional behavior of molecules in regions where experimental techniques are difficult to apply. For example the velocity distribution inside the molecular synchrotron is difficult to determine by experiment but can be calculated easily in a simulation. A full working three dimensional trajectory calculation might even predict new interesting phenomena of molecules inside the molecular synchrotron which can then be verified experimentally. But before the simulations can be trusted their output has to reproduce all individual experiments that describe the functionality of the molecular synchrotron. In the next Chapter some of the experimental measurements are compared to simulations.
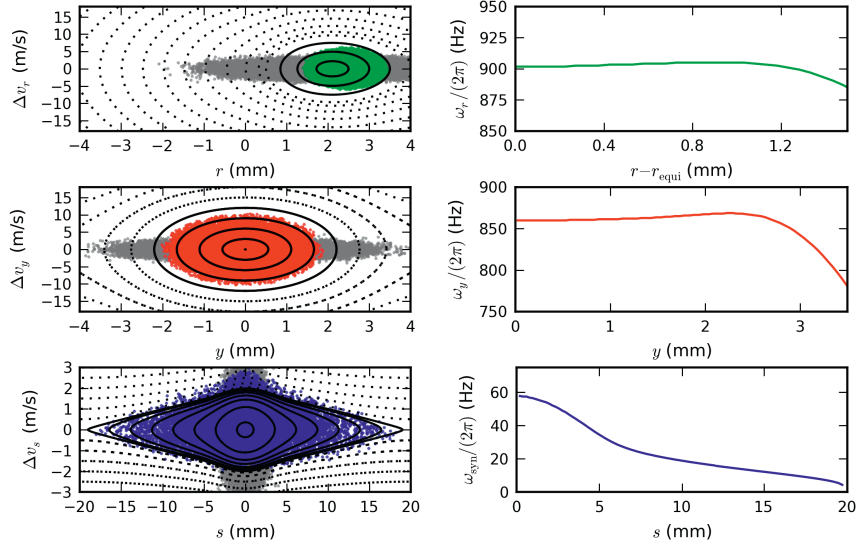
Figure 4.8: For the radial, vertical and longitudinal directions, a phase-space plot is shown in the left top, middle and bottom Panel, respectively. In this simulation 100,000 molecules with an initial Gaussian distribution flew in the molecular synchrotron for 100 round trips. The gray points indicate the initial molecular phase-space distribution; the colored points show the final simulated phase-space distribution. The right top, middle and bottom Panel shows the characteristic frequency as function of distance from the synchronous molecules from analytic models for the two transverse and longitudinal direction, respectively.

This was not done for all measurements because a calculation in which 100,000 molecules revolve in the molecular synchrotron for several seconds is time consuming and requires a large amount of computer resources (CPU and RAM). For example, in the simulation of Figure 5.8 (right Panel) the trajectory 100,000 molecules was calculated for 100,000 different voltage-velocity configurations with a Supercomputer using 100 CPUs. It took 4 1/2 days to finish the calculation. This makes it impractical to optimize the different initial conditions.

The symmetry of the molecular synchrotron implies that the electric potential of only one segment needs to be calculated precisely. The electric potentials for the other segments are determined via a transformation of coordinates from the initial segment. The electric potential of the first segment was calculated as a grid with Simion [64] using 20 grid points/mm. The force that a molecule experiences in this potential grid is determined by the second derivative of the potential field. In order to simulate a molecular beam that is injected into the molecular synchrotron from a Stark decelerator beam line, a packet of molecules with a Gaussian position and velocity spread is generated. The trajectory of each molecule is traced until a certain number of round trips have been

completed inside the synchrotron. If a molecule hits an electrode during its passage, or if it is outside of the hexapole, the calculation of that specific molecule is stopped and a new trajectory with new initial conditions is started. The number of detected molecules at the end of the simulation corresponds to the density of molecules in the experiment. The effect of misalignments is included in the simulation by changing the force that a molecule experiences inside each hexapole segment. For that, six random numbers are calculated for each segment. Three of the six number are used to shift the position in three dimensions of the hexapole by up to $20\,\mu$m while the other three are used to scale the electric field by up to 2%. These numbers are obtained such that the simulation shown in Chapters 5 and 6 reproduced the experimental data as good as possible.

The result of such a simulation is shown in the left three Panels of Figure 4.8, where 100,000 molecules flew 100 round trips. The top, middle and bottom Panel shows the phase-space distribution in the radial, vertical and longitudinal direction, respectively. The initial position and velocity distributions in all three dimensions were 2.5 mm and 2.5 m/s, respectively and are plotted as gray points in each Panel. The initial conditions should be an adequate approximation to simulate the output of each deceleration beam line. The phase-space acceptance (casually referred to as 'phase-fish') in the radial, vertical and longitudinal direction is displayed on top of each graph as a contour plot. The radial and vertical acceptances were derived from a two dimensional model (see Section 4.3), while the longitudinal phase-fish was derived from the three dimensional simulation potential. The final phase-space distribution is shown in green, red and blue for the radial, vertical and longitudinal direction, respectively. One immediately sees that the initial phase-space distribution is smeared out in all six dimensions and fills the individual phase-fishes. In the radial plot the final distribution (green points) is asymmetric compared to the phase-fish. It has higher equilibrium orbits than predicted by the two dimensional model (r'_{equi} is 2.5 instead of 2.1 mm). An explanation for this effect can be the form of the electrodes: the molecular synchrotron consists of straight hexapole segments and the equilibrium orbit is not well defined for all angles. The contour plot was derived in the middle of one segment. It would be more appropriate (but also more complicated) to use a time-averaged contour plot. In the vertical direction the distribution (red points) does not fill the entire phase-fish. The size of the vertical phase-fish is determined by the amplitude of the vertical motion and its equilibrium orbit (see loss condition in Equation (4.29) and substitute r' with r'_{equi}). The vertical phase-space acceptance inherits the inaccuracy in r'_{equi}. The longitudinal distribution (blue points) fills the entire phase-fish. The slight asymmetry in the longitudinal velocity is not yet understood.

The characteristic frequency for the radial, vertical and longitudinal directions as a function of distance to the synchronous particle is shown in the three right Panels of Figure 4.8. The characteristic frequency for the synchronous molecule is 902 Hz, 860 Hz and 58 Hz for the radial, vertical and longitudinal frequency, respectively. The values are similar or equal to the values listed in Table 4.1.
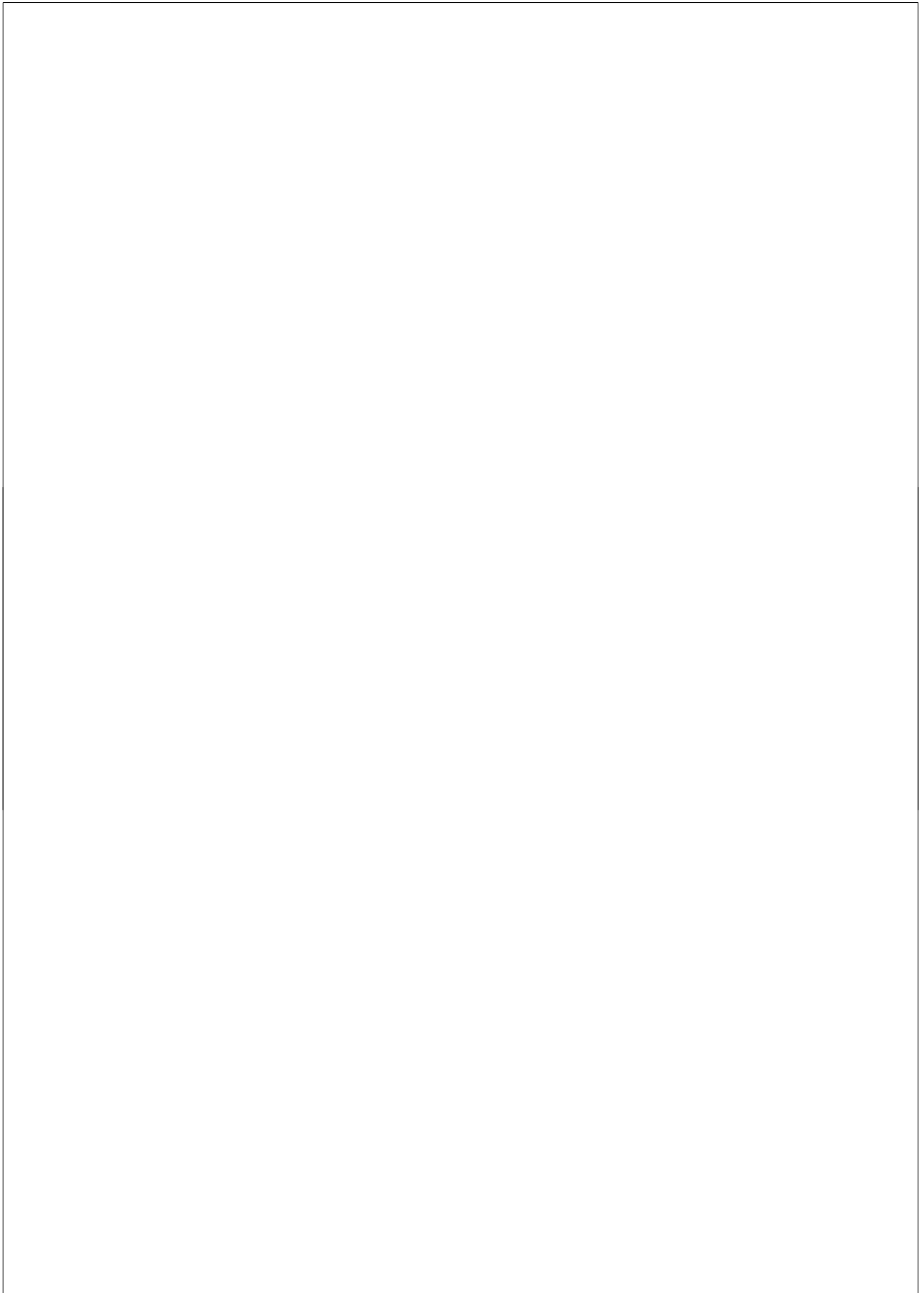
Chapter 5

Characterization of a Forty Segment Synchrotron

5.1 Introduction

In this Chapter the experimental setup is described and measurements that characterize the forty segment molecular synchrotron are shown. The first Section describes the setup together with the triggering scheme in detail. In the second Section measurements show a packet of ND_3 molecules that is stored inside the molecular synchrotron for a flight length of over one mile; highlighting the level of control that can be exerted over the motion of a molecular beam. In the third Section the triggering scheme of the current and the previous molecular synchrotron are compared. The results show a clear improvement in the longitudinal confinement scheme. A number of experiments highlight the overall control and understanding of the entire molecular beam machine and characterize the longitudinal and transverse potential wells. At the end of this Chapter, the process of injecting a molecular packet is studied and the simultaneous confinement of multiple packets in the synchrotron is demonstrated.

5.2 Experimental Setup

A photograph of the assembled molecular synchrotron is shown in Figure 5.1. The diameter of the ring is 500 mm. Each hexapole segment consists of six cylindrical highly polished electrodes with a rod diameter of 4 mm, rounded off at each end. To guarantee a constant gap of 2 mm between neighboring hexapole segments, the two inner electrodes are 36.6 mm, the two middle electrodes are 37.4 mm and the two outer electrodes are 38.1 mm long (see Figure 4.1). The electrodes are mounted on an aluminum oxide plate which also serves as an insulator. In the past, high voltage tests showed that discharges between electrodes tend to occur along the shortest pathway on the ceramic surface. A slit in the ceramic between two neighboring electrodes minimizes the chance of a discharge, by maximizing the path length along the ceramic. The ceramic plate together with the electrodes is then mounted with three screws and aligned onto a stainless steel holder. Using a special alignment tool, the center of the hexapole is aligned with respect to the holder with a precision of less than a tenth of a millimeter. These aligned holders are then placed separately with set pins onto an aluminum base plate under an angle
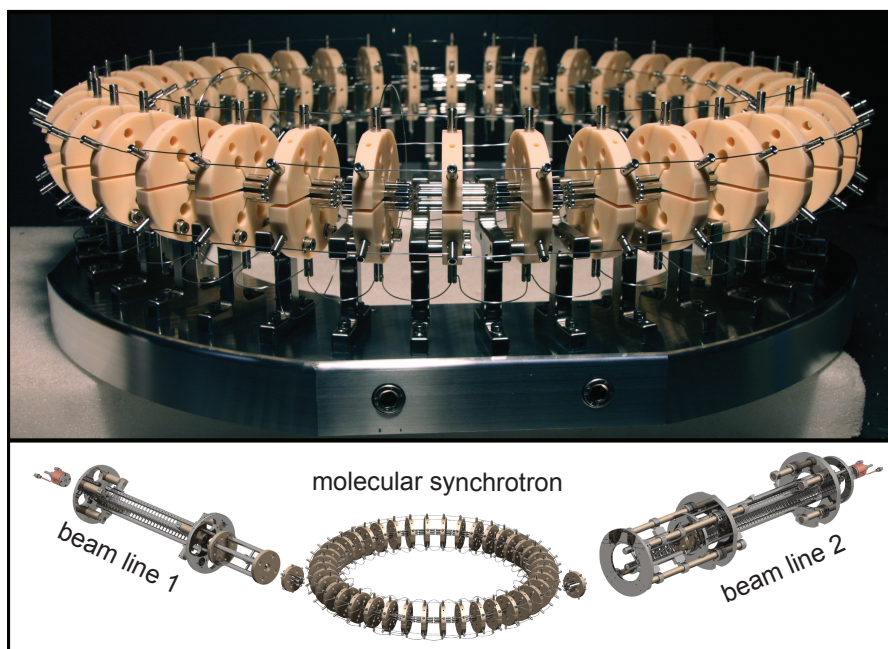
Figure 5.1: Upper Panel: A photograph of the molecular synchrotron consisting of 40 straight hexapoles separated with a 2 mm gap. Lower Panel: A photo-realistic image of the molecular synchrotron together with the two Stark decelerator beam lines.

of 9° with respect to each other. The resulting precision between neighboring hexapole segments is on the order of one tenth of a millimeter.

The molecular synchrotron consists of three different sections, which are internally connected:

- 32 hexapole segments switch the voltage between the confinement and bunching configuration continuously. The hexapoles are sketched black in Figure 4.1.

- For each beam line, the two hexapole segments that make up the first part of the injection section need to be turned off before a molecular packet can be injected into the molecular synchrotron. The relevant four hexapoles are sketched in green in Figure 4.1.

- For each beam line, two hexapole segments need to be switched off when a new packet is injected. They also need to switch to a separate voltage configuration to detect the molecules (see right Panel of Figure 3.3). These hexapoles make up the detection and the second part of the injection section. The relevant four hexapoles are sketched in red in Figure 4.1.
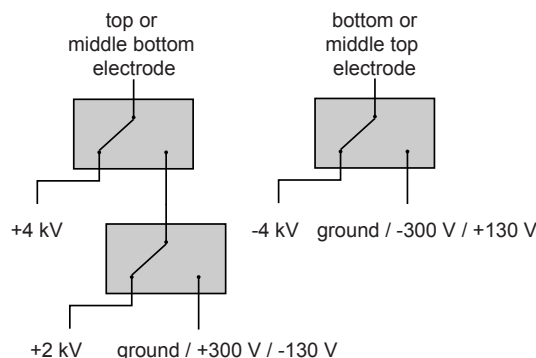
Figure 5.2: The schematic shows how the high voltage switches are connected. The positive (top and middle bottom) electrodes require two switches in series; The negative (bottom and middle top) electrodes require only one high voltage switch. The low voltage input varies depending on which section of the synchrotron and which electrode the switch is connected to.

5.2.1 High Voltage Switches

Seven high voltage power supplies are used for the two beam lines and the molecular synchrotron (manufactured by FUG (HCN 700-12500) and Spellman (SL15*1200)). The necessary thirty high voltage switches (four for the first beam line, five for the second beam line and twenty one for the molecular synchrotron) are manufactured by Behlke Electronic GmbH (HTS-151-03-GSM) and configured by the electronic workshop of the Fritz-Haber-Institut. The bias voltage is generated by eight power supplies (Delta Electronika BV (ES 0300-0.45)). Figure 5.2 shows a schematic setup of the high voltage switches. In this thesis the positive electrodes require two switches in series to switch between the confinement, the bunching and the detection/incoupling configuration. The negative electrodes switch between the confinement and detection/incoupling configuration. The lower voltage input varies depending on which electrode in which segment the switch is connected to. For the molecular synchrotron in total 21 high voltage switches are used:

- The main section needs one switch for the negative electrodes and two switches for the positive electrodes, which switch between ground and $-4\,$kV and between ground, $+2\,$kV and $+4\,$kV, respectively.

- For each beam line, the injection section needs one switch for the negative electrodes and two switches for the positive electrodes, which switch between ground and $-4\,$kV and between ground, $+2\,$kV and $+4\,$kV, respectively. For both beam lines six switches are necessary.

- For each beam line the detection section needs six switches. In addition to the confinement and bunching configuration an extraction field has to be applied when the

laser ionizes the molecules (see detection field in Figure 3.3) The top electrodes are switched between -300 V detection voltage, $+2$ kV confinement voltage and $+4$ kV bunching voltage (two switches). The middle top electrodes are switched between -130 V detection voltage and -4 kV confinement voltage (one switch). The middle bottom electrodes are switched between $+130$ V detection voltage, $+2$ kV confinement voltage and $+4$ kV bunching voltage (two switches). The bottom electrodes are switched between $+300$ V detection voltage and -4 kV confinement voltage (one switch). In total 12 switches are needed for this.

5.2.2 Number of Simultaneously Stored Packets

Theoretically a forty segment molecular synchrotron with forty gaps allows the simultaneous confinement of eighty molecular packets: forty packets traveling clockwise, and forty traveling anti-clockwise. The molecular synchrotron is loaded such that each stored packet is in a gap region when a new packet is injected. In reality the spacing between successive packets must be at least two segments, because the detection and injection hexapoles are connected in pairs of two. When a new packet is injected, the injection and detection hexapoles need to be turned off. With a spacing of one segment, a packet in the same section of the synchrotron will therefore be lost. If only one beam line is operating, up to 20 packets can be stored simultaneously. If both beam lines are operational, the upper limit of stored packets from one beam line is determined by the injection and detection of the *other* beam line. The procedure of injection and detection inside the synchrotron is synchronized such that the stored packets are not affected. With counter-propagating packets present this is best realized if all packets are located simultaneously inside the subring of the first section consisting of the 24 hexapoles (see Figure 4.1). The maximum number of simultaneously stored packets is

$$n_{\text{packets}} = 2 \cdot \left(\left\lfloor \frac{24}{n_{\text{spacing}}} \right\rfloor + 1 \right), \tag{5.1}$$

where n_{spacing} is the spacing between successive packets in units of segments. With a spacing of two hexapole segments, up to 26 packets can be confined simultaneously. In this thesis the spacing between successive packets is generally two or three segments. To illustrate the advantage of confining simultaneously multiple packets, let us consider a molecular packet with a velocity of 124.3 m/s. To measure a single packet after, *e.g.*, 1000 round trips and averaging each point 100 times it would take $100 \cdot 12.7$ s $= 21.2$ minutes. With 13 simultaneous revolving packets, each measuring point would take only 1.8 minutes.

5.2.3 Continuous and Pulsed Trigger Scheme

The detection laser and the deceleration beam lines require a repetition rate between 9 and 11 Hz [59, 68]. The time delay between the injection of successive packets, which is referred to t_{100ms}, needs to be found such that

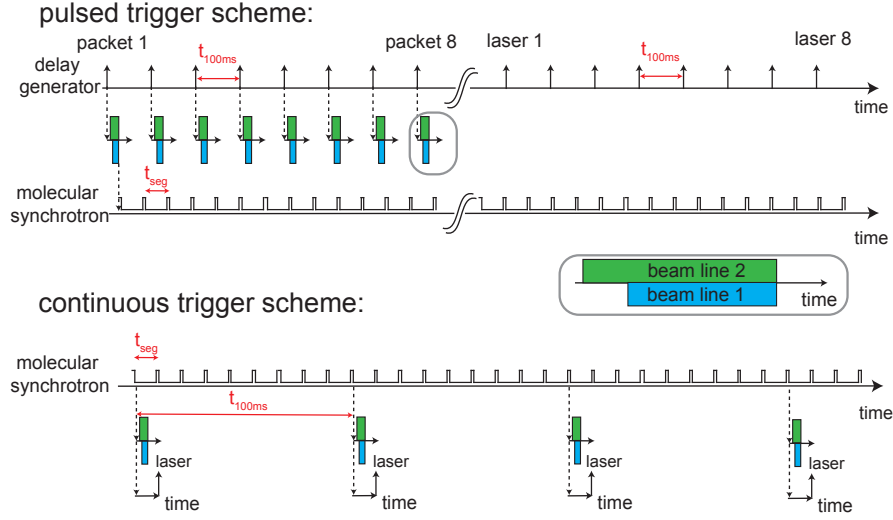$$0.09 \text{ s} < t_{\text{100ms}} < 0.11 \text{ s}. \tag{5.2}$$

Figure 5.3: The two trigger schemes of the molecular synchrotron. Subsequent packets are injected and detected with a time delay t_{100ms} of about 100 ms to assure that the repetition rate of the pulsed dye laser remains approximately 10 Hz (see Equation (5.3)). The upper Panel shows the pulsed triggering scheme for the simultaneous confinement of eight packets. In this sketch we inject, *e.g.*, eight molecular packets into the synchrotron, then wait until each packet passes the desired number of round trips before eight laser pulses are shot to detect them. The switching between confinement and bunching configuration starts after the injection of the first packet. The lower Panel shows the continuous scheme, in which the molecular synchrotron is operated continuously. After the time delay of t_{100ms} a new molecular packet is injected. The time of the laser pulse is changed relative to the injection time. All time axes are not to scale.

The time delay t_{100ms} after a new packet is injected $n_{spacing}$ segments before the stored packet is

$$t_{100ms} = (n_{rt} \cdot 40 - n_{spacing}) \cdot t_{seg}. \tag{5.3}$$

Here, n_{rt} is an integer number and t_{seg} the time that the synchronous molecule needs to pass one full segment. In this thesis a packet makes 7 or 8 round trips before a new one is introduced. The desired trigger pulses are generated with arbitrary wave form generators (Agilent 33220A) and with modified delay clock generators (FHI electronic workshop). A 10 MHz time reference clock is used so that all components have the same time basis (TCXO standard).

In the measurements presented in this thesis two different trigger schemes have been used: a pulsed and a continuous mode. In both modes multiple molecular packets revolve inside the synchrotron with the advantage that each packet revolves the same number of round trips before it is measured. Depending on the experiment one trigger scheme may be advantageous over the other.

Pulsed Trigger Scheme   The upper Panel of Figure 5.3 shows a sketch of the pulsed trigger scheme. Here, a delay generator is the master clock and all timings are defined relative to this. This master clock determines when and how many molecular packets are decelerated and injected into the molecular synchrotron. Each packet is decelerated and injected with a time sequence shown in Figure 3.2. Between each sequence is a time delay of t_{100ms} such that the spacing between packets is exactly $n_{spacing}$ segments. Every packet will stay the desired number of round trips in the synchrotron before the same number of laser pulses are sent in to detect each one of them. The time delay between each of the laser pulses is again t_{100ms}. The advantage of this trigger scheme is that an arbitrarily high number of round trips can be measured. For a large number of packets the loading and detection time is rather long, such that the pulsed trigger scheme is disadvantageous for collision studies.

Continuous Trigger Scheme   The continuous trigger scheme is shown in the lower Panel of Figure 5.3. Here, the molecular synchrotron switches continuously. Packets of molecules are injected with a delay time of t_{100ms} such that the spacing between packets is exactly $n_{spacing}$ segments. The detection laser time is triggered relative to the injection time. This allows the injection of a molecular packet into an empty gap after a previous molecular packet was detected and lost from the synchrotron. The continuous scheme is advantageous for collision studies, because a molecular packet is contained for a fixed number of round trips in the synchrotron, and interacts with counter-propagating packets before it is detected. With counter-propagating packets present a molecular packet with a velocity of 124.3 m/s and a spacing of two segments can stay up to 103 round trips in the synchrotron before it is lost (n is 8 and $n_{packets}$ is 13). The maximum number of round trips is given by

$$n_{rt,max} = n \cdot n_{packets} - 1. \tag{5.4}$$

The disadvantage of the continuous scheme is the fixed maximum number of round trips. If, *e.g.*, the depletion due to collisions is too small and it is desired to increase further the number of round trips, the pulsed trigger scheme has to be used.

5.3 Packets of Neutral Molecules Revolving for over a Mile

Figure 5.4 shows the density of ammonia molecules as a function of time after injection into the synchrotron for a series of selected numbers of round trips. In this measurement thirteen packets are injected ($n_{packets} = 13$) using the pulsed trigger scheme, after which the loading is stopped. These packets trail each other by a distance of three hexapoles ($n_{spacing} = 3$). The first and the last packet are four hexapoles apart. The different peaks correspond to characteristic number of round trips, *e.g.*, for the 640th round trip the molecular packet was confined for 8.15 s, corresponding to a flight length of one kilometer. Even after 1025 round trips, *i.e.*, after the molecules have traveled further than a mile and have passed through a gap 41,000 times, their signal can be clearly recognized. The temporal width of 21 μs corresponds to a packet length of 2.6 mm.
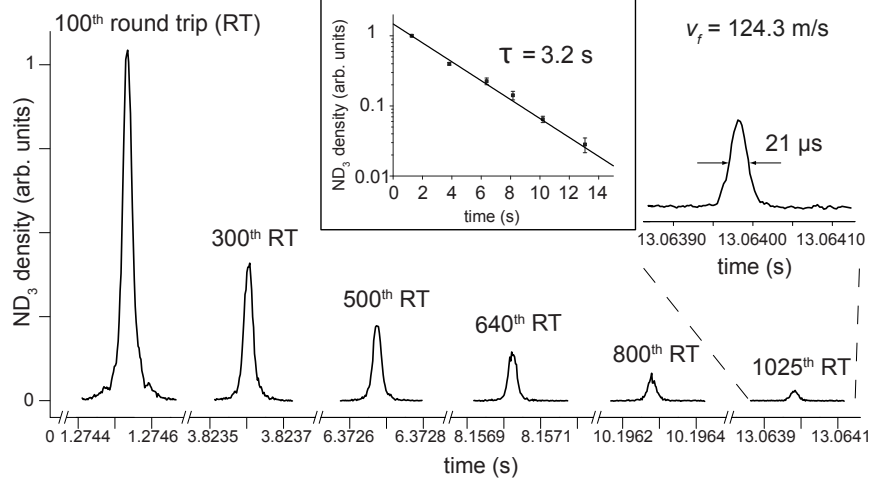
Figure 5.4: Measurements of the density of ND_3 molecules as a function of time (in seconds) for a selected number of round trips. The observed temporal width of 21 μs after 1025 round trips corresponds to a packet length of 2.6 mm after a flight distance of more than a mile. The inset shows the exponential decay of the signal with time.

This measurement explicitly demonstrates the stability of the trajectories of a molecular packet inside a molecular synchrotron.

The density of ammonia molecules is seen to decay exponentially with time at a rate of $0.31\,s^{-1}$ (see inset of Figure 5.4). This is the lowest decay rate that has been observed for neutral ammonia molecules in any trap to date. In all the early electrostatic trapping experiments, $1/e$-lifetimes of only a small fraction of a second were observed. These lifetimes were probably limited by non-adiabatic transitions to non-trappable states near the trap center, as was only realized when substantially longer lifetimes of up to 1.9 seconds were measured in an electrostatic trap with a non-zero electric field at the center [56]. With the present confinement and bunching scheme, the molecules are never close to a zero electric field in the synchrotron either. In addition, we never change the direction – but only the magnitude – of the electric field in the molecular synchrotron, effectively preventing the occurrence of non-adiabatic transitions inside the hexapoles [55]. A major contribution to the observed loss rate is the optical pumping of the ammonia molecules out of the $|J, MK\rangle = |1, -1\rangle$ level by blackbody radiation, calculated to occur at a rate of $0.14\,s^{-1}$ in the room-temperature chamber [69]. The remaining loss-rate of $0.17\,s^{-1}$ is well explained by collisions with background gas at the approximately $5 \cdot 10^{-9}$ mbar pressure in the vacuum chamber.

The longitudinal position spread can be determined from the time-of-flight (TOF) measurements presented in Figure 5.4. Each of the TOF profiles is fitted with a Gaussian
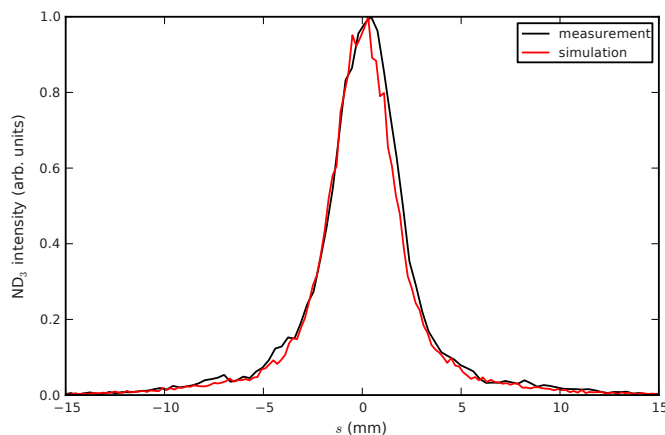
Figure 5.5: The experimentally measured and simulated position spread after 100 round trips. The experimental data and the simulation are from Figure 5.4 and Figure 4.8, respectively.

and from the fitted width the position spread is calculated. The spread is fairly constant over a trapping time of 13 seconds corresponding to 1025 round trips. The averaged position spread is 2.9 mm.

In Figure 5.5 the position spread of the 100th round trip is shown together with the simulated position spread. For the experimental data, the time-of-flight was normalized and the peak maximum was set to zero seconds. To obtain the position spread it was multiplied by the synchronous velocity ($v_f = 124.3$ m/s). The simulation was performed using the input parameters as discussed in Section 4.6. All molecules that made 100 round trips were binned along the longitudinal direction, s, and then normalized.

5.4 A Superior Bunching Scheme

The bunching scheme described in Section 4.4 is different from the longitudinal confinement scheme employed in the two piece molecular synchrotron. To distinguish between the two schemes the bunching of the previous molecular synchrotron is referred to as 'old scheme' and that of the current molecular synchrotron as 'new scheme'. In the old two segment molecular synchrotron, every time the molecular packet enters a gap region a sequence of electric fields are switched to achieve a longitudinal confinement force. Here, the old scheme is described briefly; more details are available in references [23, 25]. Let us assume a molecular packet is flying into a gap region; leaving hexapole 1 behind and entering hexapole 2 (see left Panel of Figure 5.6). To achieve a longitudinal confinement force first hexapole 1 is switched to ground and hexapole 2 is switched to a bunching con-
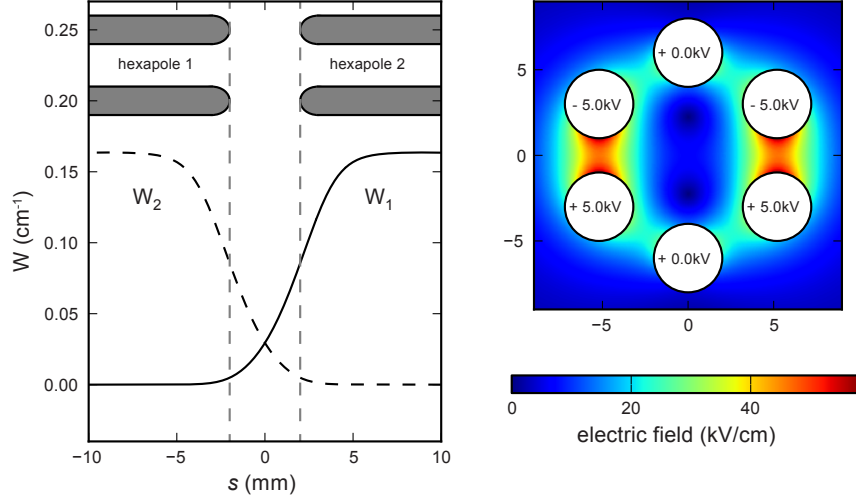
Figure 5.6: Longitudinal bunching principle used in the studies of Heiner and coworkers on a synchrotron consisting of two hexapole half rings. The left Panel shows the potential energy of an ammonia molecule as a function of longitudinal position for two different configurations. The gap between the hexapole segments is 2 mm. When the synchronous molecule enters the gap region along the equilibrium orbit, hexapole 1 is switched to ground while hexapole 2 is switched to the bunching configuration. The molecule experiences the solid potential W_1 and is decelerated. After the molecule passed the middle of the gap the switching scheme is reversed; hexapole 2 is switched to ground while the voltage is applied to hexapole 1 (W_2). The molecular packet is now accelerated along the dashed potential W_2 such that the overall kinetic energy of the synchronous molecule is not changed. The electric field and the voltage configuration of the bunching field is shown in the right Panel.

figuration. In this bunching configuration the top and bottom electrodes are grounded while the middle top electrodes are on positive high voltage and the middle bottom electrodes are on negative high voltage (see right Panel of Figure 5.6). The molecular packet experiences a potential hill in which the fast molecules are more strongly decelerated than the slow molecules. When the synchronous molecule is in the middle of the gap, hexapole 1 is switched to the bunching configuration and hexapole 2 is grounded. The molecular packet now experiences a potential that accelerates the molecular packet; the slow molecules experience longer acceleration than the fast molecules. The field is switched such that the kinetic energy of the synchronous molecule is not changed. Molecules which are in front of, or behind, the synchronous molecule are pushed towards the synchronous molecule. The molecular packet is 'bunched' longitudinally. To compensate for the lack of transverse focusing in the gap, the confinement focusing force is increased for a short time period before and after the gap region (referred to as the 'kicker'). Compared to the bunching scheme described in Section 4.4, the potential well
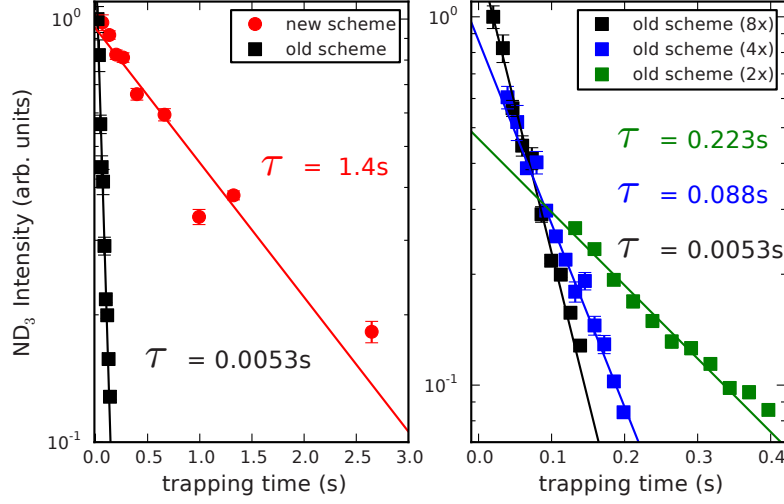
Figure 5.7: Left Panel: Measurements of the density of ND_3 molecules as a function of time inside the 40 segment molecular synchrotron with the two different bunching schemes (logarithmic scale). For both measurements the molecular packet is bunched every fifth hexapole segment (8 times per round trip). The black points refer to the bunching scheme that was used in the previous molecular synchrotron consisting of two half rings ('old scheme') [23]; the red points correspond to the bunching scheme which is described in Section 4.4 ('new scheme'). The exponential fit determines the lifetime of the molecular packet inside the synchrotron. Right Panel: The ammonia decay measurement of the old bunching scheme for three different numbers of bunching per round trip; in black the molecular packet is bunched 8 times, in blue 4 times and in green 2 times per round trip.

of the old bunching scheme is a factor of ten steeper.

To compare both switching schemes the wiring of the synchrotron was changed. Five hexapole segments are wired together (yielding 8-fold symmetry) and only one molecular packet is stored at a time. For both bunching schemes the density of the molecular packet is plotted in the left Panel of Figure 5.7 on a logarithmic scale together with an exponential fit. The new scheme (red circles) results in a lifetime of 1.4 s while the old scheme (black squares) results in a lifetime of 5.3 ms. To explain the fast exponential decay, the right Panel of Figure 5.7 shows the exponential decay of the old scheme when the bunching procedure is applied for several different numbers per round trip made by the ammonia molecules. For the green, blue and black measurement the molecular packets are bunched 2, 4 and 8 times per round trip. When the number of bunching sequences per round trip is increased, the experimental decay becomes faster. The loss is attributed to two different loss processes: (i) The molecules could undergo a spin-flip transition (non-adiabatic transition) to a state that is not low-field seeking

while one hexapole is grounded [56]. (ii) Molecules could be lost due to the lack of transverse focusing while the molecule is bunched. All measurements were normalized such that the injected molecular packet has a fixed amplitude. In the previous molecular synchrotron with two gaps this effect did not dominate the loss mechanism, but for a molecular synchrotron with forty gaps it is essential to use the new bunching scheme. The lower velocity range that is accepted by the new scheme is compensated by the superior stability. In addition, the new bunching scheme is less demanding for the high voltage electronics. The confinement of molecules in a synchrotron requires theoretically only one high voltage switch. To detect and inject multiple packets the number of necessary switches increases strongly (see Section 5.2.1). To conclude, Figure 5.7 clearly demonstrates the superior longitudinal confinement of the new scheme.

5.5 Transverse Motion - Stopbands

Breaking the symmetry of a perfect circular structure causes motional resonances; for a given hexapole voltage configuration certain forward velocities cannot be confined stably (see Section 4.5). By measuring the ammonia density after a fixed number of round trips as a function of velocity and voltage, the resonances are made visible. Both Panels in Figure 5.8 show the ammonia intensity after 100 round trips. The left Panel shows the experimental data, in which each point was averaged 52 times. The right Panel of Figure 5.8 shows the corresponding numerical calculation. The experimental plot has on the horizontal axis 200 voltage steps and on the vertical axis 39 velocity steps. In the simulation the trajectories of 100,000 molecules were calculated for 100 different velocities and 100 different voltage configurations. A small additional random force was added in each segment in order to reproduce the effect of misalignments in the synchrotron.

In both the experiment and the simulation some main features deserve special attention:

- The ND_3 intensity increases when the velocity of the injected packet is larger (see Section 3.3). To keep the equilibrium orbit constant, the voltage difference V_0 needs to be adjusted accordingly. If the inversion splitting is neglected and the hexapole has a perfect harmonic potential, the relation is $v_f \propto \sqrt{V_0}$.

- Under the conditions corresponding to a high velocity and low voltage (top left part in both Panels) no molecules are stably confined, because the centrifugal force is stronger than the restoring force of the hexapole.

- If the velocity of the molecules is too low and the voltage too high (bottom right parts in Figure 5.8) also no molecules are stably stored. The equilibrium orbit for these molecules is small, thus molecules oscillate around the zero electric field region in the center of the hexapole and undergo Majorana transitions [55, 56]. After the transition the ammonia molecules are not in the $|J, MK\rangle = |1, -1\rangle$ state anymore and therefore cannot be detected. To implement the Majorana transition
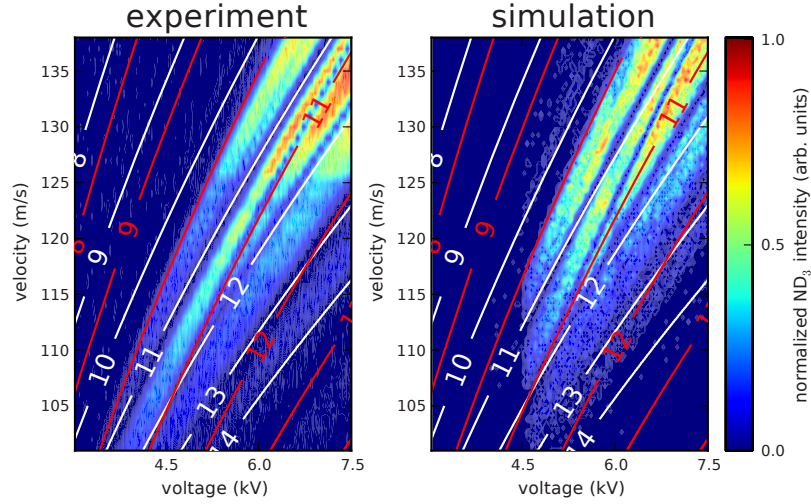
Figure 5.8: Experimental and simulated ammonia intensity after 100 round trips as a function of velocity and voltage. The left Panel shows the experimental data, in which each point is averaged 52 times. 200 different voltages were measured for 39 different velocities (200x39 grid). The right Panel shows the result of the corresponding numerical calculation in which 100,000 molecules fly in the molecular synchrotron for 100 round trips. Here, 100 different voltage configurations and 100 different velocities where taken into account (100x100 grid). On top of both graphs the horizontal and vertical integer tune is plotted as a contour plot. The white curves correspond to the horizontal r tune and the red to the vertical y tune. The tunes were calculated using Equation (4.22) in which the angular frequency was derived using an analytic function of the electric field that was derived by Anderson [52].

in the simulation, an ammonia molecule is assumed to be lost if its potential energy is less than $0.009\,\mathrm{cm}^{-1}$, corresponding to an electric field of $11\,\mathrm{kV/cm}$.

- For certain combinations of the velocity and voltage a large decrease in signal is observed. These so-called 'stop bands' are caused by resonances. The integer tunes for both transverse directions, calculated from the transverse angular frequency and by applying Equation (4.22), are plotted onto the multicolor contour plot. The white curves correspond to the radial tune while the red curve show the vertical tunes.

The stop bands depicted in Figure 5.8 characterize the transverse character of the molecular synchrotron. A perfect 40-fold molecular synchrotron (as explained in Section 4.5) should have no stops bands in the velocity range from $100-140\,\mathrm{m/s}$ with a $6\,\mathrm{kV}$ voltage difference applied to the electrodes. If the individual hexapole segments are mechanically misaligned or if they have a different voltage applied, the symmetry of the synchrotron

is broken and stop bands are induced. In the experiment the integer tunes (white and red curves) fit on top of the contour plot and reproduce the motional resonances. The structure of the stop bands in the simulation is similar to that in the experimental data, but shifted slightly to higher velocities. A possible cause is that the electric field in the simulation does not reproduce the experimental conditions exactly. The slope of a horizontal tune (white curve) is smaller than the vertical tune (red curve), because the vertical frequency in this velocity range is smaller than the horizontal one.

Figure 5.9 shows the progression of the stop bands at a voltage difference of 6 kV for a selected number of round trips. The dashed black and red vertical lines correspond to the velocity of the calculated stop bands. The gray curve represents a velocity scan before the molecular packet is injected (see Section 3.3). Already after one round trip molecules at certain velocities are lost from the synchrotron. At $v = 119 \, \text{m/s}$ the ammonia intensity has a local maximum although the $\nu_r = 12$ tune is exactly at this velocity. The structure on top of the velocity scans changes for the following round trips until the velocity of the stop bands agrees with the theoretically predicted velocities. Figure 5.9 shows that the radial tune ν_r causes more losses than the vertical tune ν_y. This is attributed to the fact that the horizontal potential well is shallower than the one in the vertical direction.

5.6 Longitudinal Motion

The longitudinal potential is best described with the longitudinal angular frequency ω_{syn} which is equal to the velocity spread Δv_s divided by the position spread Δs

$$\omega_{\text{syn}} = \frac{\Delta v_s}{\Delta s}. \tag{5.5}$$

In Figure 5.10 a molecular packet is stored for a selected number of round trips (RT) after which the electric field is switched permanently to the confinement configuration. The packet then spreads out along the longitudinal direction. By measuring the position spread Δs as a function of expansion time t, the forward velocity spread Δv_s can be determined. The relation between the position spread and expansion time is

$$\Delta s(t) = \sqrt{(\Delta s_i)^2 + (\Delta v_s \cdot (t - t_{\text{min}}))^2}. \tag{5.6}$$

Here, Δs_i is the initial position spread and t_{min} the time at which the molecular packet has a minimal position spread. If, *e.g.*, the molecular packet was bunched 10 times per round trip before the expansion, t_{min} is the time the synchronous molecule needs to pass 2 hexapole segments. With 40 bunching sequences per round trip, t_{min} corresponds to the time that has an effective length of half a hexapole segment.

The left Panel of Figure 5.10 shows the longitudinal position spread of a molecular packet after it was stored in the synchrotron for 5 round trips (RT). The discrete measured points correspond to position spreads at different numbers of round trips after the expansion; The black and red squares are measurements where the molecular packet was bunched 2 and 40 times per round trip, respectively. The solid line shows the fit
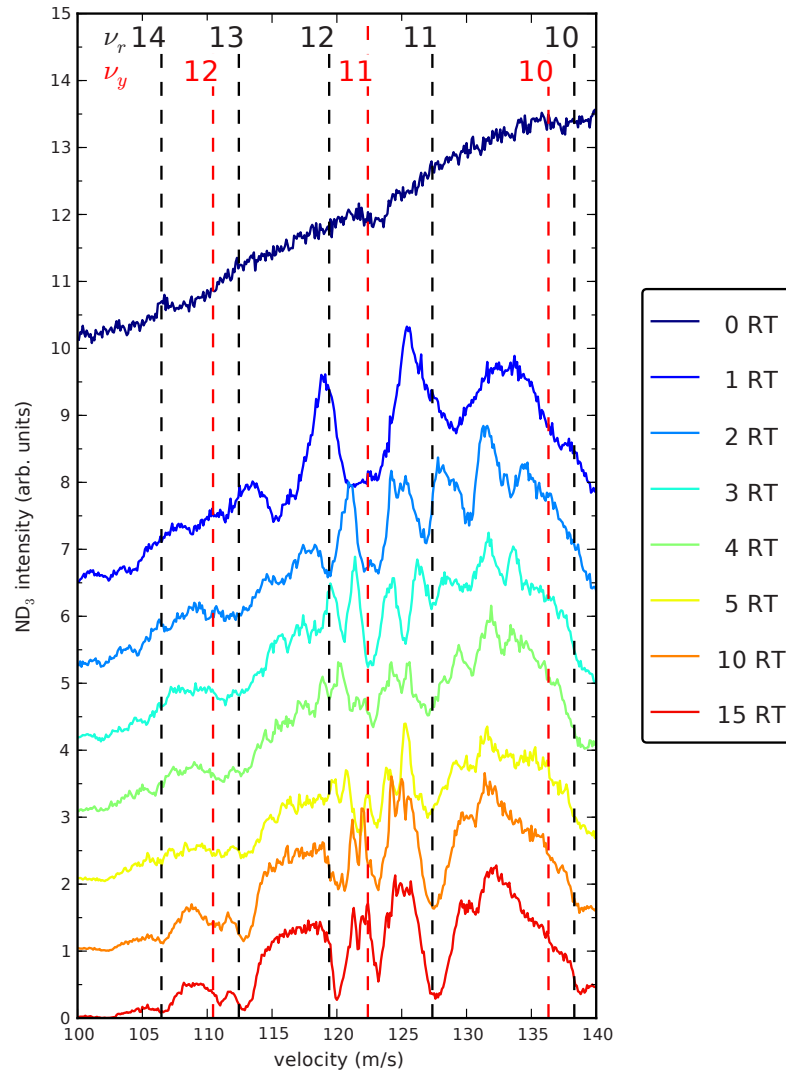
Figure 5.9: The density of ND$_3$ molecules at the detection zone after completing a selected number of round trips as a function of forward velocity. The gray curve shows the ND$_3$ signal before the molecular packet is injected into the synchrotron. At a given voltage difference of 6 kV molecules with certain velocities are not stably confined. After 15 round trips the position of each stop bands is fixed to a certain velocity. The dashed black and red vertical lines show the velocity of the calculated stop bands for the radial and vertical tune, respectively.

Figure 5.10: The longitudinal expansion of an ND$_3$ packet in the molecular synchrotron; The left Panel shows the position spread of the molecular packet after 5 round trips (RT) against the expansion time. The black and red points correspond to a molecular packet with 2 and 40 bunching stage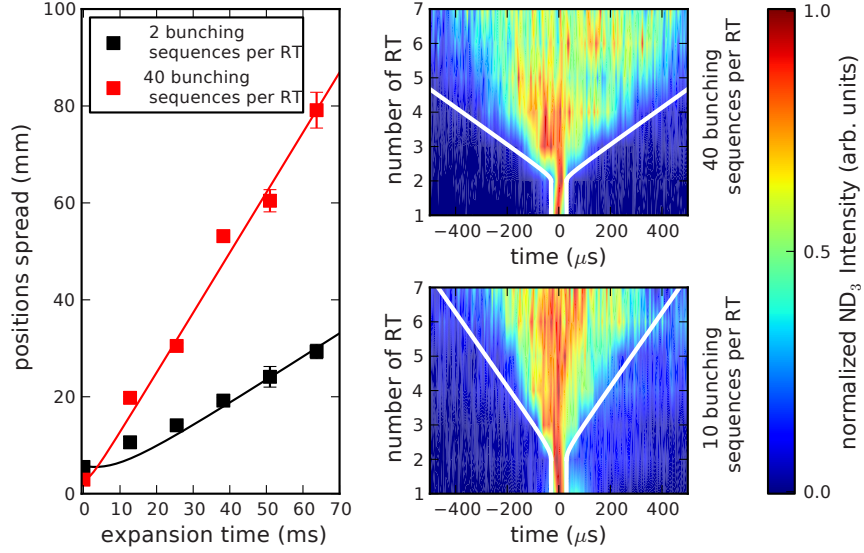s per round trip, respectively. The solid lines show the fit using Equation (5.6). The two right Panels illustrate the expansion; After the second round trip the electric field is kept constant and the packet spreads out. The upper and lower right Panel show the expansion with 40 and 10 bunching sequences per round trip. The solid white line shows the theoretical expansion using Equation (5.6) with $\omega_{\mathrm{syn}}/(2\pi)$ taking a value of 58 and 29 Hz for the upper and lower right Panel, respectively. To achieve the best contrast for the two dimensional plots, each time-of-flight trace (horizontal axis) was normalized.

performed using Equation (5.6). If the packet is bunched 40 times per round trip (red curve), the fitted initial position spread and velocity spread is 2.9 mm and 1.2 m/s, respectively. $\omega_{\mathrm{syn}}/(2\pi)$ is given by Equation (5.5) as 68 Hz. The relation between angular frequency and periodicity of the bunching is

$$\omega_{\mathrm{syn}} \propto \frac{1}{\sqrt{L}}, \tag{5.7}$$

where L is the period length. If the bunching field is switched only twice per round trip (black curve), L is 20 times larger. The frequency should be a factor of 4.5 smaller, around 15 Hz. Indeed measurements taken when the bunching field is switched twice per round trip give a position spread of 5.5 mm and a velocity spread of 0.5 m/s (left Panel), yielding a frequency of 14 Hz.

The two multicolor plots in Figure 5.10 illustrate the expansion directly: In both
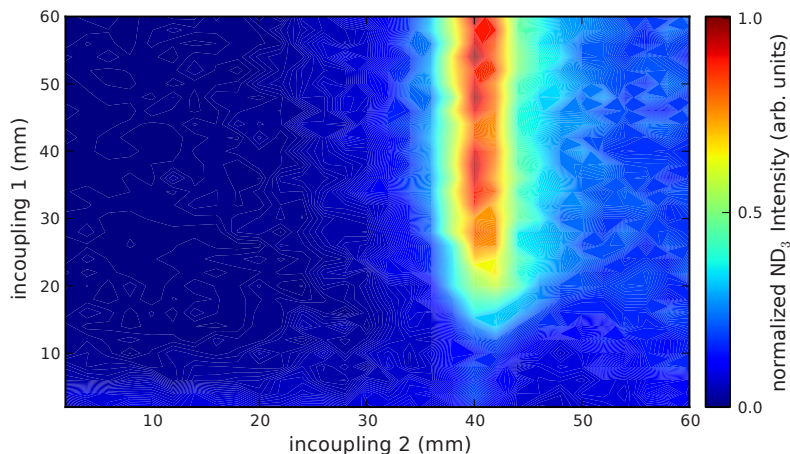
Figure 5.11: The ammonia intensity is shown as a function of how long the injection/detection hexapoles in the individual beam lines are turned off. On the horizontal axis is the effective length of the detection hexapole (incoupling 2). This indicates how long relative to the detection point the red segment in Figure 4.1 is turned off. On the vertical axis is the effective length of the injection segment which is measured relative to incoupling 2 (green hexapoles in Figure 4.1). $n_{spacing}$ is 2.

Panels the ammonia intensity is shown as a function of the number of round trips and relative time of the detection of the synchronous molecule. The molecular packet is confined for two round trips (RT), after which the switching of the electric field is stopped. The molecules experience the confinement field and only spread out in the longitudinal direction. In the upper and lower right Panels the molecular packet is bunched 40 and 10 times per round trip, respectively. The fewer the number of bunching sequences per round trip, the shallower is the potential well and the lower the velocity spread. The white curve in the upper and lower right Panel uses Equation (5.6) and a theoretical frequency of 58 and 29 Hz (see Table 4.1).

5.7 Injection of a Molecular Packet

Storing multiple packets in the synchrotron requires that a packet, that is already stored, is not influenced by the injection of a new packet. The timing when the injection and detection segments are switched off is crucial to the confinement of the packet already inside the synchrotron as well as to the packet that is to be injected. If the hexapole segments are turned off too long, a packet will easily be injected, but a previously stored packet will lack the confining force. If high voltage is applied to the hexapole segments, a molecular packet will not reach the injection point because it is deflected by the electric

68

field. The time when the individual injection and detection hexapoles (green and red hexapoles in Figure 4.1, respectively) are switched off is expressed as an effective length.

Let us assume that a molecular packet is decelerated, bunched and focused transversally. First the injection segments (green hexapoles) need to be turned off (incoupling 1). When the synchronous molecules reaches the gap between the red and the green segments the detection hexapole segments have to be switched off and the incoupling segment on (incoupling 2). When the synchronous molecule reaches the injection point between the two red hexapoles, all hexapole segments are switched to high voltage. The switching procedure is illustrated in the burst sequence of Figure 3.2. In order to determine if a packet is injected properly the measured packet needs to be confined longer than t_{100ms} in the synchrotron. By that time a new packet with the same incoupling sequence is injected (see Section 5.2.3). If the injection is too short, no molecules will enter the synchrotron. If the injection hexapole are off too long, the stored packet will be lost when the new packet is injected. This effect is shown in Figure 5.11, in which a molecular packet is measured after 10 round trips where $n_{spacing}$ has a value of 2. The two dimensional plot shows the ammonia intensity as a function of the effective length of incoupling 1 and 2. The horizontal axis shows the effective length of incoupling 2 relative to the injection of the molecular packet. The vertical axis shows the effective length of incoupling 2 relative to incoupling 1. Only if the effective length of incoupling 2 is 40 mm and incoupling 1 is larger than 30 mm can a molecular packet be injected without losing the packet that was already stored in the synchrotron. If the effective length of incoupling 2 is smaller than 40 mm, no molecules reach the detection zone. If incoupling 2 is larger than 40 mm the molecular packet can only be confined for 7 round trips, before it is lost while injecting a new packet. With a spacing of two hexapole segments between successive packets the effective lengths of incoupling 1 is 60 mm and of incoupling 2 40 mm. The injection can be improved at the cost of the number of stored packets if $n_{spacing}$ is increased to 3.

The buncher in both decelerator beam lines influences the velocity spread of the packet but should not affect the synchronous velocity. If the effective position of the buncher is not exact, the synchronous molecule will change its final velocity. If the buncher is turned on too early, the molecular packet is accelerated, and will reach the injection region earlier. If the buncher is turned on too late, the molecular packet is decelerated and requires more time to reach the injection point. The molecular synchrotron is used to determine both positions by changing the effective buncher position and the effective injection position after a fixed number of round trips. Figure 5.12 shows for both beam lines such a two dimensional scan, performed after 5 round trips. The optimal buncher position is 614.7 mm and 645.4 mm for beam line 1 and 2, respectively. The injection point is 961 mm and 1163 mm behind the skimmer. The tilt in the graph exemplifies the change of the final velocity due to the buncher.
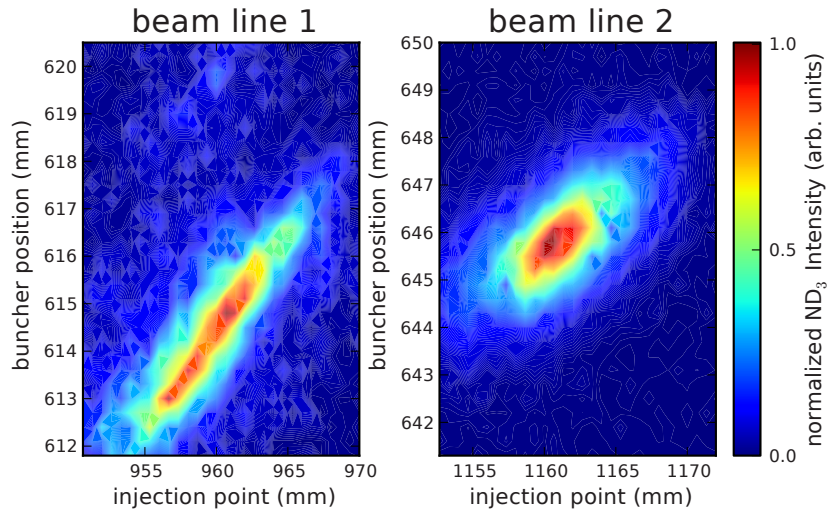
Figure 5.12: The ammonia intensity after 5 round trips as a function of effective position of the buncher (vertical axis) and effective injection point (horizontal axis) for beam line 1 and 2, respectively. Both positions are relative to the skimmer of the individual beam lines.

5.8 Multiple Packets

Figure 5.13 shows a measurement of nineteen co-propagating packets of ammonia molecules with a forward velocity of 120 m/s, loaded from beam line 1. The horizontal axis shows the time relative to the time at which the first injected packet has completed 150 round trips. The last injected packet has been in the ring for 320 ms and has made 24 round trips while the first injected packet has by then already been stored for more than 2 seconds. The loading scheme is set up such that each packet completes 7 round trips plus the length of 2 hexapoles before the next packet is injected. In the measurement the packets are seen to trail each other by 666 μs – precisely the time it takes them to fly through two hexapoles. Only the time period between the first and last injected packet is equal to an effective length of four hexapole segments. The injection of multiple counter-propagating packets will be discussed in Chapter 7
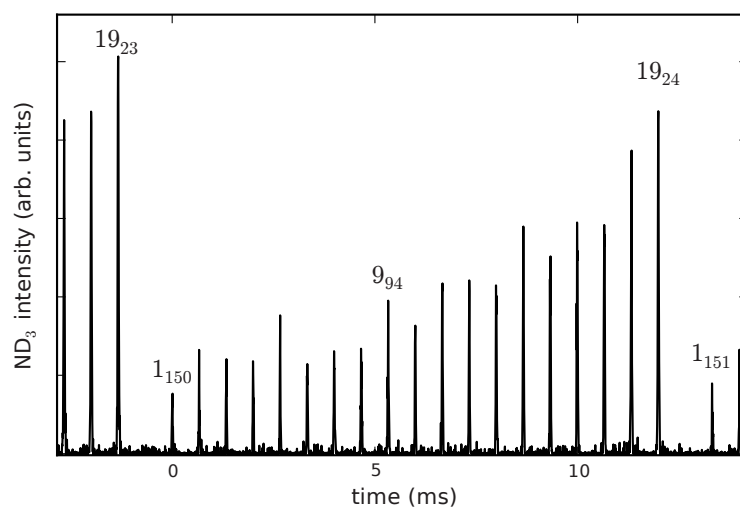
Figure 5.13: Time-of-flight measurement showing 19 packets of ammonia molecules with a forward velocity of $120\,\mathrm{m/s}$ revolving simultaneously in the molecular synchrotron. The horizontal axis shows the time relative to the time at which the first injected packet has completed 150 round trips. Each packet is labeled with two numbers: the main number labels the order of injection whereas the subscript labels the number of completed round trips.
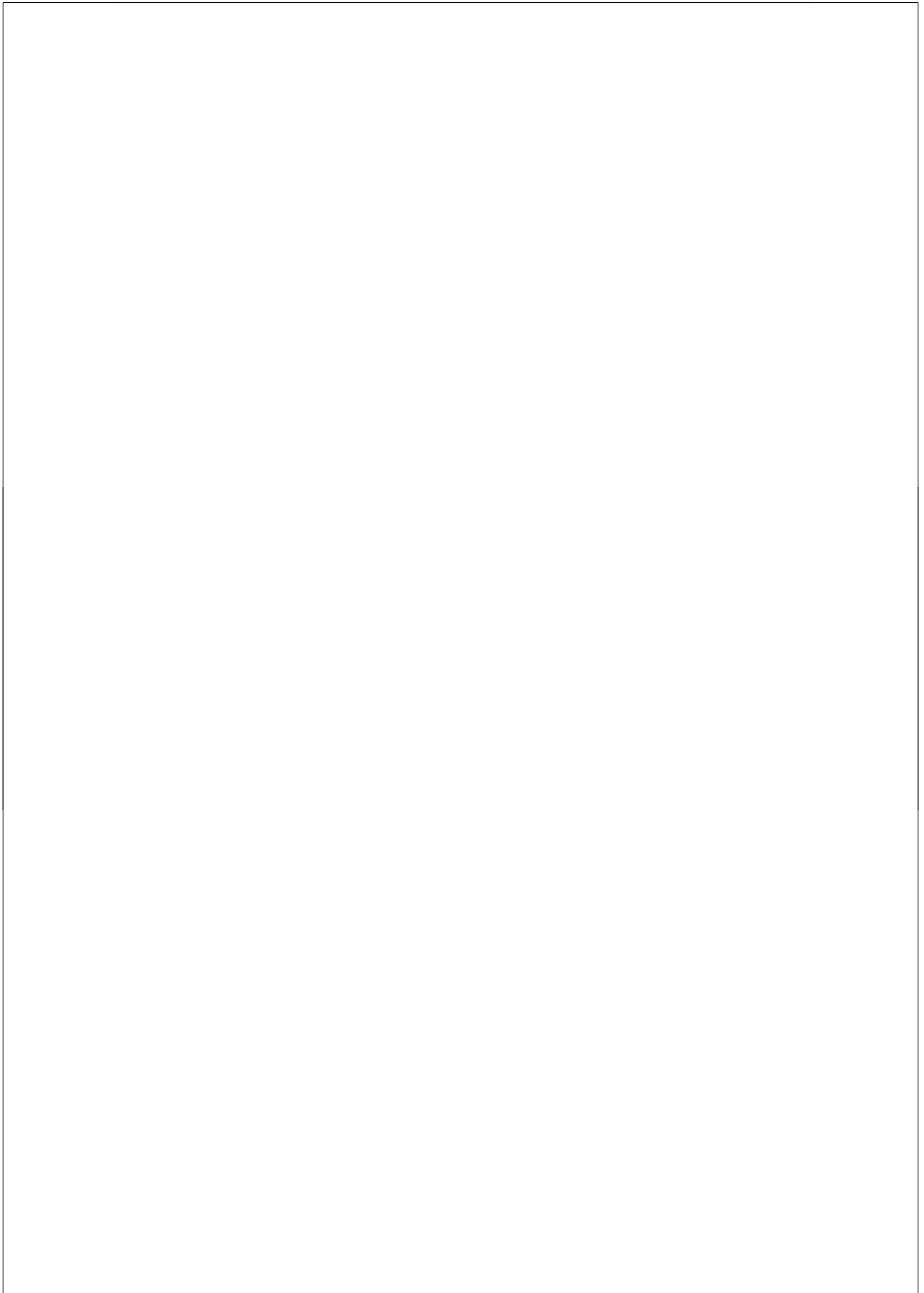
Chapter 6

Excitation Measurements

6.1 Introduction

A full understanding of the molecular synchrotron is essential for its use as a low-energy molecular collider. In the previous Chapter, different experimental techniques were introduced which allowed the detailed characterization of the molecular synchrotron. In particular, the motional frequencies of the trapped molecules were determined using a number of different techniques. This Chapter presents an approach in which these characteristic frequencies, describing the three dimensional potential well of the molecular synchrotron, are measured directly. The technique is based on resonant excitation. A well-known example of such excitation in the real world is the fall of the Broughton suspension bridge on April 12$^{\text{th}}$, 1831, near Manchester (UK) [70]. When 60 soldiers where marching over the small bridge in Broughton it began to vibrate. The lock-step of the soldiers resonantly amplified this vibration until the bridge finally collapsed. To prevent other bridges from collapsing the military introduced a 'breaking step' for troops marching over a bridge. This event is still used in textbooks as an example of forced resonance because it demonstrates that a small force can cause a big response. For more than two decades this principle of resonant excitation has been an established technique in the field of ion trapping, allowing the investigation and manipulation of stored ions [71, 72]. By modulating the confining voltage of the trap with a small additional sinusoidal voltage (on the order of 1% of the confining voltage), particles whose motion is resonant with the external modulation frequency experience a rapid increase in their oscillation amplitude until they are expelled from the trap. By measuring the number of trapped molecules as a function of the frequency of the additional voltage, the characteristic motional frequencies of the trap can be mapped out.

In this Chapter resonant ejection is used to determine the three (longitudinal, vertical and radial) characteristic frequencies of the synchrotron. The first Section explains how the voltages and the trigger scheme are changed in order to shake the potential well. In the second Section the motion of the molecules is described in a mathematical model. In the last Section the experimental results are shown and discussed.

6.2 Setup

The principle of resonant excitation relies on the fact that a periodic small deviation applied at the right frequency increases the amplitude of the motion inside the molecular
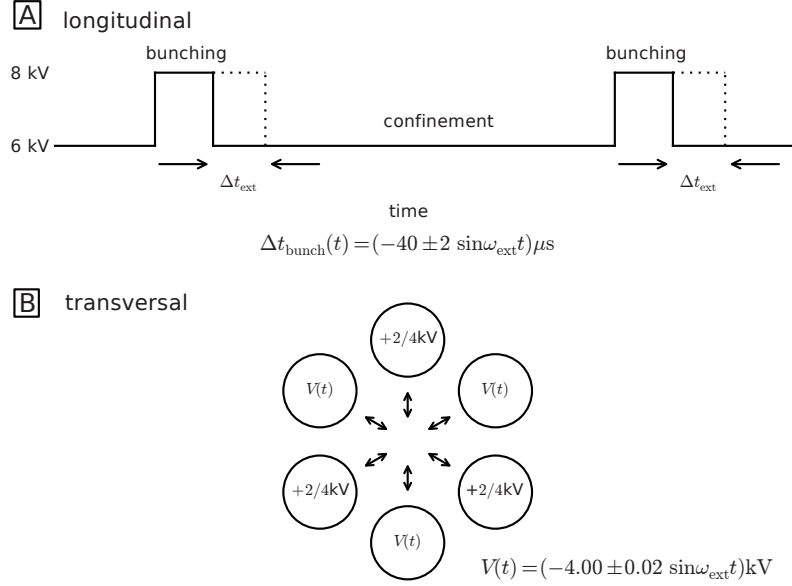
Figure 6.1: Two different schemes to excite the motion of the molecules longitudinally and transversely in the molecular synchrotron. The upper Panel (A) shows the excitation of the potential well in the longitudinal direction. The time duration of the bunching pulse Δt_{bunch} in the switching scheme is prolonged by Δt_{ext} which is itself a function of an external frequency. The lower Panel (B) illustrates the excitation in the transverse direction. In this case, the negative voltage of -4 kV is modulated by a sinusoidal voltage with an amplitude of 20 V. The electric field varies only in the radial direction (indicated with arrows).

synchrotron. This 'shaking' of the potential well can be realized in two different ways, as sketched in Figure 6.1. To excite the longitudinal motion, the average longitudinal confining force is changed as a function of some external frequency ω_{ext}. By prolonging and reducing the time duration of the bunching pulse Δt_{bunch} a small external periodic change of the force is achieved. The time duration of the bunching pulse is given by

$$\Delta t_{\text{bunch,ext}} = \Delta t_{\text{bunch}} + \Delta t_{\text{ext}} \sin\left(\omega_{\text{ext}} t\right). \tag{6.1}$$

Here, Δt_{ext} is the maximum time difference that is applied to the falling edge of the switching process. Schematically this is shown in the top Panel of Figure 6.1.

In the transverse direction, the confining voltage V_0 of each hexapole segment is instead modulated with a small sinusoidal voltage with an external frequency.

$$V_{0,\text{ext}} = V_0 + \Delta V_{\text{ext}} \sin\left(\omega_{\text{ext}} t\right). \tag{6.2}$$

Here, ΔV_{ext} is the maximum voltage with which the negative electrodes are modulated. The shaking in the transverse direction is sketched in the lower Panel of Figure 6.1.

6.3 Mathematical Description

Molecules that are trapped inside the synchrotron will oscillate radially, vertically and longitudinally around the synchronous molecule. Let us first consider the motion in the radial direction. With no external AC field present, the time-dependent radial position $r(t)$ can be written, to a first approximation, as

$$r(t) = r_{\text{equi}} + r_0 \cos{(\omega_r t)}, \qquad (6.3)$$

in which r_{equi} is the equilibrium orbit, r_0 is the maximum oscillation amplitude and ω_r is the radial betatron oscillation frequency. The corresponding radial velocity $v_r(t)$ is

$$v_r(t) = -r_0 \omega_r \sin{(\omega_r t)}. \qquad (6.4)$$

If the electric field is now modulated by an external frequency ω_{ext} , the molecule experiences a time-dependent force $f(r,t)$ which can be approximated by

$$f(r,t) = -k_0(1 + \delta \sin{(\omega_{\text{ext}} t)})r(t). \qquad (6.5)$$

Here, k_0 is the force constant of the hexapole field and δ describes the amplitude of the external oscillation. In our experiments, δ is normally below 1%. In order to amplify the oscillation, the force needs to be applied in the same direction as the velocity of the trapped molecules. A molecule is lost from the potential well if the energy of the particle continuously increases, in other words if there is work done on the particle. The work done on the molecule by the external frequency in the radial direction, $W_r(t)$, can be approximated by

$$\begin{aligned}
W_r(t) &= \int_0^{r(t)} f(r,t)\mathrm{d}r = \int_0^t f(r,t)\frac{\mathrm{d}r}{\mathrm{d}t}\mathrm{d}t \\
&= \int_0^t f(r,t)v_r(t)\mathrm{d}t.
\end{aligned} \qquad (6.6)$$

Only the additional ω_{ext}-dependent term in the force of Equation (6.5) can amplify the radial motion. Equations (6.3) to (6.6) can now be combined to give

$$\begin{aligned}
W_r(t) &= \delta \int_0^t (-k_0 \sin{(\omega_{\text{ext}} t)}) \left(r_{\text{equi}} + r_0 \cos{(\omega_r t)} \right) \left(-r_0 \omega_r \sin{(\omega_r t)} \right)\mathrm{d}t \\
&= \delta \omega_r k_0 r_{\text{equi}} \int_0^t r_0 \sin{(\omega_r t)} \sin{(\omega_{\text{ext}} t)}\mathrm{d}t \\
&\quad + \delta \omega_r k_0 \int_0^t r_0^2 \sin{(\omega_r t)} \cos{(\omega_r t)} \sin{(\omega_{\text{ext}} t)}\mathrm{d}t.
\end{aligned} \qquad (6.7)$$

The integrals can be simplified such that the radial part of the work can be written as

$$\begin{aligned}
W_r(t) &= \delta \omega_r k_0 r_{\text{equi}} \underbrace{\int_0^t \frac{r_0}{2} \left[\cos{((\omega_r - \omega_{\text{ext}}) t)} - \cos{((\omega_r + \omega_{\text{ext}}) t)} \right] \mathrm{d}t}_{I} \\
&\quad + \delta \omega_r k_0 \underbrace{\int_0^t \left(\frac{r_0}{2}\right)^2 \left[\cos{((2\omega_r - \omega_{\text{ext}}) t)} - \cos{((2\omega_r + \omega_{\text{ext}}) t)} \right] \mathrm{d}t}_{II} .
\end{aligned} \qquad (6.8)$$

Both integrals become zero unless $\omega_{\text{ext}} = \omega_r$ (integral I) or $\omega_{\text{ext}} = 2\omega_r$ (integral II). Within this model the position of the resonances can be determined quite accurately, but the prediction of the strength of both resonances is more difficult. In a first approximation, if we take the maximum amplitude to be time-independent, the ratio between the first fundamental and second harmonic excitation would be given by $r_{\text{equi}}/(r_0/2)^2$. However, this approximation neglects the fact that at a resonance, the maximum amplitude r_0 changes and becomes time-dependent. In this case, the two integrals cannot be solved analytically and a relation between fundamental and second harmonic resonance cannot be given.

If a molecule oscillates in the vertical direction, the same derivation and argumentation can be used, except that the equilibrium orbit in the y direction is zero. Therefore, a resonance should not occur at the fundamental vertical frequency but should be present if the excitation frequency is $2\omega_y$.

To shake the potential well in the longitudinal direction, the bunching pulse is changed as sketched in the upper Panel of Figure 6.1. The synchronous molecule experiences an asymmetric change in the longitudinal force. Therefore, both the fundamental and the second harmonic frequency should be detectable, despite the equilibrium orbit taking a value of zero.

Inside the synchrotron the motions of the molecule in the longitudinal and two transverse directions are not independent. The conservation of angular momentum couples individual motions to each other. If, *e.g.*, a molecules oscillates in the forward direction, then conservation of angular momentum demands that the oscillation amplitude in the radial direction increases, conserving the magnitude of the impulse. Therefore, the oscillation amplitude in the radial direction increases. Furthermore, the transverse confining forces are a function of the position in the segment, *i.e.*, towards the gaps the transverse forces are smaller than in the middle of the hexapole. As the molecules pass through these hexapoles at a more or less constant speed, the transverse motion is modulated with the 'so-called' segment frequency f_{seg}.

$$f_{\text{seg}} = \frac{v_f}{L_{\text{seg}}} = \frac{\omega_{\text{seg}}}{2\pi}. \tag{6.9}$$

Here, ω_{seg} is the angular segment frequency, v_f the synchronous velocity and L_{seg} is the distance the synchronous molecules flies in a hexapole segment. At $124.3\,\text{m/s}$ f_{seg} is $3138\,\text{Hz}$. This frequency is also likely to show up in the excitation scan.

6.4 Shaking the Moving Well

Figure 6.2 illustrates the excitation measurements performed after 100 round trips. The top Panel shows the transverse and the bottom Panel the longitudinal excitation. The black curves in both Panels correspond to the experimental data, while the gray curves are the result of trajectory calculations. As explained in Section 6.3, the ammonia density as a function of external frequency is almost constant in the frequency spectra. Only at certain frequencies does the signal decrease significantly, corresponding to fundamental
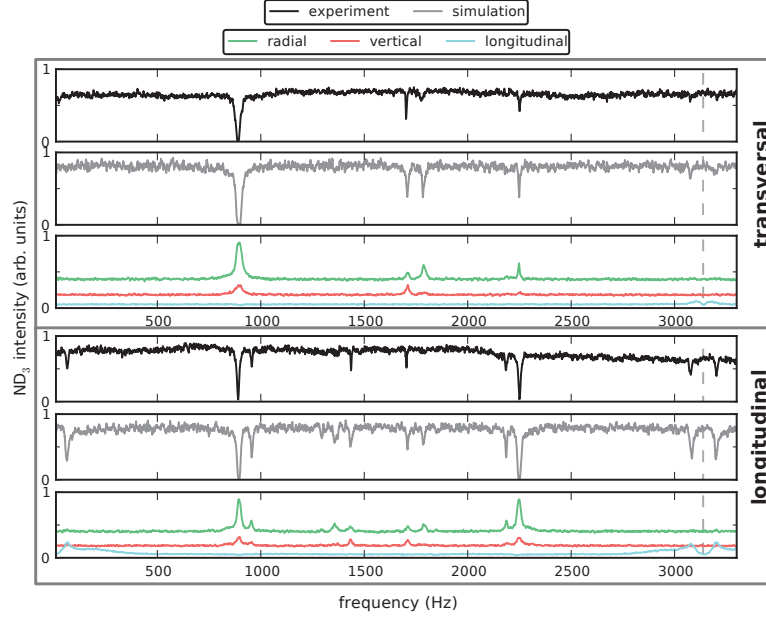
Figure 6.2: The top Panel shows the ND_3 intensity as a function of frequency at which the transverse potential is modulated (black curve). Underneath the simulated spectrum is shown in gray. The light green, light red and light blue spectra show the losses in the radial, transverse and longitudinal direction, respectively. The dashed gray vertical line indicates the segment frequency f_{seg}. For the transverse frequency scan the assignment of the resonances is shown in the left side of Table 6.1. The lower Panel shows the excitation measurement in the longitudinal direction. Underneath the simulated and loss spectra are shown. For the experimental longitudinal frequency scan the assignment of the resonances is shown in the right side of Table 6.1

resonances, overtones and combination of these two. A list of the resonances, together with their assignment, is shown in Table 6.1. In both simulation and experiment a molecular packet of ammonia molecules with a forward velocity of $124.3\,\mathrm{m/s}$ was confined inside the molecular synchrotron, and a small sinusoidal excitation was applied. In the transverse direction this excitation was obtained by modulating the confining voltage by 0.3%, corresponding to $\Delta V_{ext} = 20\,\mathrm{V}$. For the longitudinal excitation Δt_{ext} was set to $2\,\mu\mathrm{s}$. In order to match the simulation and the experiment, the excitation strength in the simulation was increased: in the transverse direction the restoring force was modulated by 0.6% and in the longitudinal direction Δt_{ext} was set to $5\,\mu\mathrm{s}$. This is attributed to the fact that in the simulation the effect of misalignments is not correctly implemented. The increased amplitude of the additional force is justifiable because it only changes the relative intensity of the resonances; their position is not affected. In both simulations

transverse measurement		longitudinal measurement	
frequency	assignment	frequency	assignment
-	-	64 Hz	ω_{syn}
890 Hz	ω_r	890 Hz	ω_r
-	-	955 Hz	$\omega_r + \omega_{\mathrm{syn}}$
-	-	1437 Hz	$\omega_{\mathrm{seg}} - 2\,\omega_y$
1701 Hz	$2\omega_y$	1704 Hz	$2\,\omega_y$
1780 Hz	$2\omega_r$	-	-
-	-	2184 Hz	$\omega_{\mathrm{seg}} - (\omega_r + \omega_{\mathrm{syn}})$
2251 Hz	$\omega_{\mathrm{seg}} - \omega_r$	2250 Hz	$\omega_{\mathrm{seg}} - \omega_r$
-	-	3075 Hz	$\omega_{\mathrm{seg}} - \omega_{\mathrm{syn}}$
-	-	3204 Hz	$\omega_{\mathrm{seg}} + \omega_{\mathrm{syn}}$

Table 6.1: The detected resonances (in Hz) from Figure 6.2 together with their assigned angular frequency for the transverse and longitudinal frequency scan.

the trajectories of 1500 molecules at each excitation frequency were calculated. In this program it was checked, in which direction an excited molecule was expelled from the synchrotron. In light green, light red and light blue the simulated losses in the radial, vertical and longitudinal direction are shown in both Panels, respectively.

Let us first focus on the transverse frequency scan. Here, four resonances are detected. The strongest depletion is at 890 Hz and corresponds to the characteristic radial frequency. No depletion of signal is found at the fundamental vertical frequency of 850 Hz but a relatively strong resonance is observed at 1701 Hz, which corresponds to the second harmonic in the vertical direction. The peak next to it (at 1780 Hz) is much weaker and results from the second harmonic of the radial frequency. The last peak at 2251 Hz results from a coupling of the radial frequency with the segment frequency f_{seg}.

The simulated spectrum shows all the expected characteristic resonances. Only for the second harmonic of the radial resonance is the simulation much stronger than in the experiment. As mentioned before, the strength of the second harmonic resonance compared to the fundamental is influenced by the spatial width of the molecular packet. It might be that the simulation does not reproduce the actual phase-fish of the experiment. The loss spectrum in all three directions nicely confirms the assignment of the peaks.

The longitudinal excitation is shown in the lower Panel of Figure 6.2. Compared to the excitation in the transverse direction, this experimental frequency spectrum shows mostly the same resonances but also some new features. All detected resonances are listed and assigned in Table 6.1. The new resonances occur primarily due to the coupling of the synchrotron and the segment frequency to the other characteristic frequencies. The fundamental synchrotron frequency is observable at 65 Hz. Its second harmonic frequency is not visible. The strongest resonance occurs at the radial frequency of 890 Hz which implies a strong coupling between the longitudinal and radial motion. The coupling to the segment frequency must also be strong, as all frequencies that are coupled to it have the same strength as in the uncoupled case. For example the
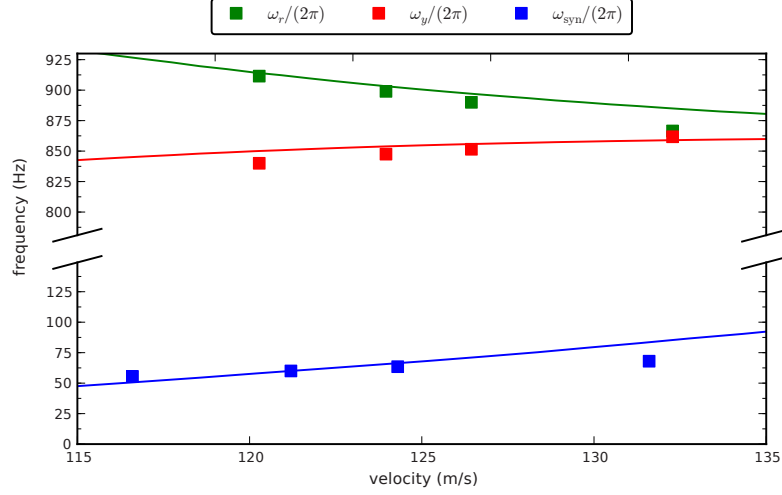
Figure 6.3: The characteristic trap frequencies as a function of the velocity of the molecular packet. The squares are experimental data determined by excitation measurements performed at different velocities. The theoretical velocity-dependent frequencies are drawn as solid lines. The blue, red and green points and lines correspond to the longitudinal, vertical and radial frequency, respectively.

depletion of ammonia signal at $890\,\mathrm{Hz}$ (ω_r) is similar to the dip at $2250\,\mathrm{Hz}$ ($\omega_{\mathrm{seg}} - \omega_r$). The depletion at $955\,\mathrm{Hz}$ is due to the coupling of the synchrotron motion with the radial frequency. This depletion is observed only at a frequency of ($\omega_r + \omega_{\mathrm{syn}}$) and not at a frequency of ($\omega_r - \omega_{\mathrm{syn}}$). We attribute this asymmetric coupling due to peculiarities in the formulas describing the Coriolis force. An exact model for this phenomena is currently lacking.

The result of the trajectory simulation is shown underneath the experimental data. Here, all resonances are reproduced and can be nicely assigned with the help of the loss measurements shown in the light colors underneath. The relative strengths of some resonances could not be reproduced entirely. As before, the discrepancy is attributed to the fact that the phase-space distribution of the simulation does not exactly reproduce that of the experiment.

By changing the velocity of the injected packet at a constant voltage, the equilibrium orbit of the molecular packet changes. This changes all three characteristic frequencies accordingly. The results of such experimental measurements are shown in Figure 6.3, in which the measurement in Figure 6.2 was repeated for four different velocities at a constant voltage configuration of $6\,\mathrm{kV}$. As mentioned in Chapters 4 and 5, at a constant voltage only certain velocities are stable confined (see Figure 5.9). The radial, vertical and longitudinal characteristic frequencies are sketched as green, red, and blue squares. The theoretical prediction of the characteristic frequency as a function of forward velocity

was done by analyzing the electric field around the equilibrium orbit. For the longitudinal frequencies all three spatial dimensions were considered (the same field that produced the simulation). For the radial and vertical directions a two dimensional model was used (the same fields that predicted the stop bands in Section 5.5). The theoretical prediction is shown in Figure 6.3 as a solid line following the same color labeling as for the resonances.

As demonstrated by the experimental results presented in this Chapter, the excitation of the molecular motion is a powerful tool to characterize the molecular synchrotron in a single measurement. A small change in the confinement voltage or in the longitudinal triggering scheme as a function of an external frequency results in a periodic change in the force that is applied to the molecules. If the external frequency is equal to a fixed combination of the characteristic frequencies, the amplitude of the motion is increased which may lead to loss of molecules from the synchrotron. The measured characteristic frequencies are in good agreement with the frequencies derived in the previous Chapter.

Chapter 7

Towards Collisions

7.1 Introduction

As mentioned in Chapter 1, the study of molecular collisions in the low-energy regime is a sensitive method to determine the potential energy surface (PES) between the two collision partners. In most cases the obtained experimental data provides a cross section (*e.g.* the elastic, the inelastic and/or the total collision cross section), or the angular distribution of the scattered products. The comparison between the experimental results and theoretical predictions is of special interest, as it highlights the understanding of the physical model of the collision system. So far, studying collisions with two Stark-decelerated beams has not been tried in a classical crossed beam experiment, because the required densities of the final packets for a successful collision are too low.[2]

The main advantage of the repeated interaction of counter-propagating packets in a molecular synchrotron is that the collision signal accumulates as the molecules revolve in the synchrotron. The more molecular packets that are stored inside the synchrotron, the higher the possibility to detect a bi-molecular collision. The total cross section can be determined by measuring the pseudo first order rate constant for the loss of ND_3 molecules from the synchrotron with and without the propagating packets. When operating the synchrotron with counter-propagating packets, the signal intensity will decrease due to collisions (dependent on the storage time) compared to the case where packets are confined only in one direction. From the ratio of the two measurements as a function of storage time, a bi-molecular total collision cross section can be determined. The use of a molecular synchrotron to study collisions also has some limitations; the main one being that no information is available after the collision.

The focus of this Chapter is on the current status of the state-of-the-art molecular synchrotron. It describes the capability of the experimental apparatus to detect collisions between counter-propagating packets of molecules. As a straightforward experiment, the first Section illustrates the collision between ND_3 molecules stored in the synchrotron and xenon gas. The second Section treats the collision of counter-propagating packets: First the simultaneous confinement of 26 packets of deuterated ammonia is shown, in which 13 packets propagate clockwise and 13 packets propagate anti-clockwise. Afterwards the measurement scheme is described and the first results together with the data analysis of

---

[2]Recently, M. Kirste and coworkers determined a density of about 10^8 molecules/cm^3 in Stark-decelerated beam of OH radicals [21]. In the molecular synchrotron the expected number of molecules is in the order of 10^6 to 10^7 molecules/cm^3 [73].

the bi-molecular collisions are presented.

7.2 Collisions with Xenon

In this Section, packets of ND_3 molecules with a fixed velocity and velocity spread collide with room temperature xenon atoms. It serves as an example which illustrates how the storage time of a molecular packet is influenced by collisions. As mentioned in Section 5.3 there are two major decay mechanisms by which molecules that are stably confined inside the molecular synchrotron can be lost. One is the excitation from the trapped $|J, MK\rangle = |1, -1\rangle$ state to a different rotational or vibrational state by black body radiation. The second decay mechanism results from collisions with the background gas in the vacuum chamber. In this Section the second phenomena is used to determine the total collision cross section of ammonia molecules with xenon atoms. The background gas consists of different components but the major part are xenon atoms that are used to cool the molecules in the supersonic expansion. They enter the synchrotron chamber together with the undecelerated molecular beam. The xenon density and therefore the collision decay rate is manipulated by leaking in additional xenon through a leak valve into the synchrotron vacuum chamber. The top Panel of Figure 7.1 shows the logarithmic ND_3 intensity as a function of storage time of the molecular packet for eleven different pressures in the vacuum chamber. The ammonia molecules have a velocity of $124.3\,\mathrm{m/s}$ and are confined with a confinement voltage of $6\,\mathrm{kV}$. The vacuum chamber and, in a first approximation, the xenon atoms are at room temperature. The linear fit of each trace is plotted as a solid line. The higher the pressure inside the vacuum chamber the stronger is the exponential decay. The dark blue points in Figure 7.1 are the background measurement at $5.76 \cdot 10^{-9}\,\mathrm{mbar}$ in which no additional xenon was leaked into the chamber; the slope of this decay is used in the following as a reference measurement. All other decays rates are calculated relative to this reference and are plotted as a function of xenon density in the lower Panel of Figure 7.1. The main part of the error arises from the limited (absolute) precision of the pressure measurement of the background gas. The pressure was determined with two active cold cathode transmitters (Pfeiffer Vacuum - IKR 251 [74]).

The total decay rate k_{coll} is the sum of the two decay rates

$$k_{\mathrm{coll}} = k_{\mathrm{bb}} + k_{\mathrm{bg}}, \tag{7.1}$$

where k_{bb} is the decay rate due to the black body radiation and k_{bg} the decay rate due to the collisions with the background gas. Using the decay with the lowest pressure as a reference allows us to neglect the effect of the black-body radiation. If a molecular packet of ND_3 molecules interacts for a length of $\mathrm{d}x$ with a xenon gas with a density of $[Xe]$, the change in the ammonia density can be expressed as

$$\mathrm{d}\,[ND_3] = -\,[Xe] \cdot \sigma_{\mathrm{tot}} \cdot [ND_3] \cdot \mathrm{d}x. \tag{7.2}$$

Here, the xenon density is time independent. Introducing the relative velocity

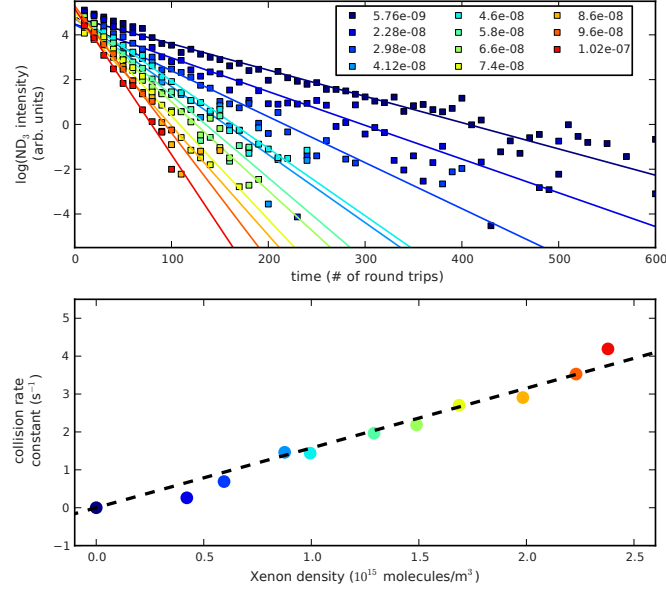$$v_{\mathrm{rel}} = \frac{\mathrm{d}x}{\mathrm{d}t} \tag{7.3}$$

Figure 7.1: The top Panel shows the logarithmic ND_3 intensity as a function of completed round trips for eleven different pressures of xenon inside the vacuum chamber (values in the legend are given in mbar). The chamber and xenon atoms were at room temperature; the velocity of the molecular packet was $124.3\,\mathrm{m/s}$. The pressure was regulated by leaking in pure xenon with a leak valve into the vacuum chamber. The linear fits of each trace are shown as solid lines. The bottom Panel shows the resulting pseudo first order collision rate constant as a function of xenon density. The dashed line shows a linear fit.

Equation (7.2) can be written as

$$\frac{\mathrm{d}\,[ND_3]}{\mathrm{d}t} = -\,[Xe] \cdot \sigma_{\mathrm{tot}} \cdot v_{\mathrm{rel}} \cdot [ND_3] = -k_{\mathrm{bg}}\,[ND_3]\,, \tag{7.4}$$

using the pseudo first order background collision rate

$$k_{\mathrm{bg}} = [Xe] \cdot \sigma_{\mathrm{tot}} \cdot v_{\mathrm{rel}}. \tag{7.5}$$

Here, σ_{tot} is the total collision cross section and $\mathrm{d}t$ the interaction time. After the separation of variables and integrating both sides, the ammonia density as a function of time can be written as

$$[ND_3]\,(t) = [ND_3]_0\,\mathrm{e}^{-k_{\mathrm{bg}}t}, \tag{7.6}$$

in which $[ND_3]_0$ is the ammonia density at $t = 0\,\mathrm{s}$. The slope of the linear fit in the lower Panel of Figure 7.1 is $1.58 \cdot 10^{-15}\,\mathrm{m^3/s}$. With a relative velocity of $124.3\,\mathrm{m/s}$ the
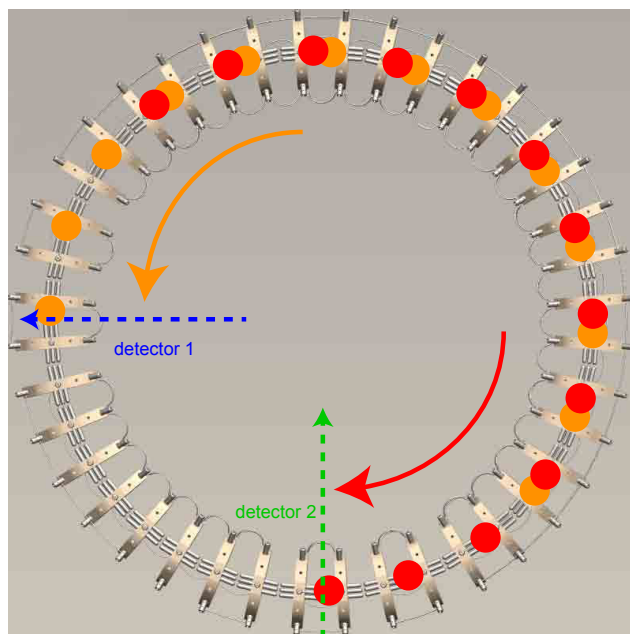
Figure 7.2: A photo realistic image of the molecular synchrotron to illustrate the confinement of 26 packets. 13 packets from decelerator 1 propagate counter clockwise (orange circles) and 13 packets from decelerator 2 propagate clockwise (red colors). In each direction the distance between neighboring packets is two hexapole segments. The first and the last packet are separated by 16 hexapole segments. At two detection points the molecular packets are injected and detected simultaneously. The dashed blue and green arrow indicates the laser which ionizes the molecules at the first and second detection zone, respectively.

measurements give a total collision cross section of $1300\,\mathrm{\AA}^2$. However, it should be noted that this number has a very high inaccuracy due to the uncertainty of the absolute xenon pressure.

7.3 Collisions between Counter-Propagating Packets

In collision studies involving counter-propagating packets of molecules, losses in the number of stored molecules due to (in)elastic collisions accumulate over the interaction events. Let us consider n packets of molecules revolving clockwise and n packets revolving anti-clockwise, all with the same speed. After m round trips, each packet of molecules will have interacted $2 \cdot n \cdot m$ times with counter-propagating packets. Section 5.2.3 states that in the current molecular synchrotron a maximum of 26 molecular packets can be confined simultaneously; 13 molecular packets moving clockwise and 13 packets moving
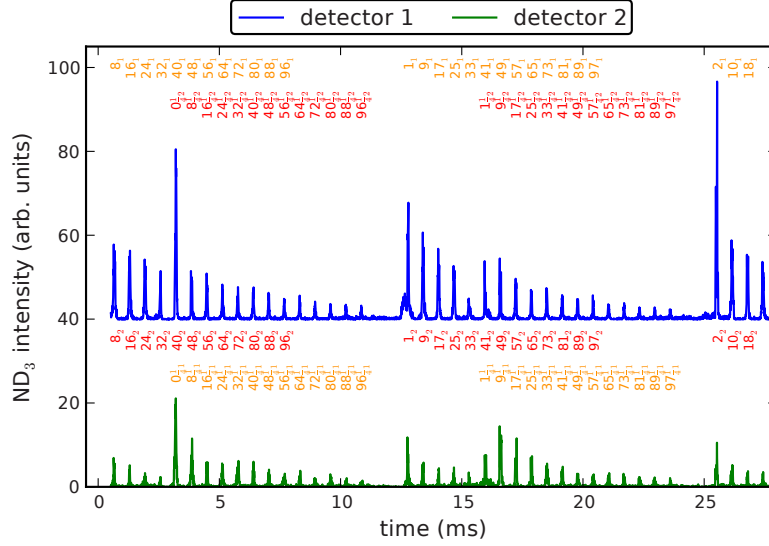
Figure 7.3: A time-of-flight measurement of ammonia molecules in the molecular synchrotron when both beam lines operate using the continuous trigger scheme (discussed in Section 5.2.3). The signal recorded at detector 1 and 2 is shown in blue and green, respectively. $t = 0$ ms corresponds to the time when a new molecular packet is injected. The 26 (2x13) molecular packets are each labeled with two numbers. The main number indicates how many round trips the packet revolved inside the molecular synchrotron before it was detected; the subscript indicates the beam line it was injected from. The color labeling follows Figure 7.2.

counter-clockwise. The sensitivity to a collision after 100 round trips will be therefore about 10^3 times higher than measuring the collision in a single collision event.

Figure 7.2 shows how the packets are confined. Here, the 13 orange circles indicate packets from decelerator 1 which revolve anti-clockwise. The 13 packets from decelerator 2 propagate clockwise and are shown as red circles. The distance between neighboring packets traveling in the same direction is two hexapole segments. Only for the first and the last injected packet is the distance 16 hexapole segments. A time-of-flight measurement of such a case is shown in Figure 7.3 using the continuous trigger scheme. The ammonia intensity as a function of time is shown in blue and green for the detector of beam line 1 and 2, respectively. The injection of all packets is performed under the same conditions. Here, the packets have a forward velocity of 124.3 m/s. At $t = 0$ ms a new molecular packet is injected. Above each detected packet a label defines how many round trips this packet was confined in the synchrotron before it was detected (main number) and from which decelerator beam line it was injected (subscript). The pattern of the upper and lower time-of-flight profile is similar for both detectors and is described here considering the first detection zone. A series of molecular packets is detected with

a periodicity of 12.7 ms (corresponding to the time the synchronous molecules require to complete one round trip). As can be seen from the labeling of the time-of-flights and Figure 7.2, the clockwise and anti-clockwise packets partially overlap each other when being detected. The first five and the last five detected packets originate from beam line 1 and 2, respectively. The eight packets in the middle of the series are from beam line 1 and 2 together. The time difference between adjacent peaks is $636 \,\mu$s - the time it takes the molecules to fly through two hexapoles. The time difference between the last detected packet of beam line 2 and the first detected packet of beam line 1 corresponds to a spacing of 4 segments. If a new injected packet traveled ten segments in the molecular synchrotron, when it reaches the detection zone, it overlaps with the packet from the other beam line that was confined for 40 round trips. This effect can be seen at 3.2 ms, where the ND_3 intensity due to the packet from beam line 2 increases significantly.

Measurement Scheme of a Molecular Collider   After the successful confinement of multiple counter-propagating packets, the next step is to use the molecular synchrotron as a molecular collider. First, the necessary mathematical descriptions are presented. Let us analyze how the ammonia intensity changes a function of time if counter-propagating packets are present. By substituting the xenon density in Equation (7.4) with $[ND_3]$, the change of the ammonia density can be rewritten as

$$\frac{\mathrm{d}\,[ND_3]}{\mathrm{d}t} = -k_{ND3}\,[ND_3]^2 \,.$$

(7.7)

Here, k_{ND3} is the decay rate due to bi-molecular collisions. Separating the variables and integrating both sides the density of the ammonia molecules as a function of time can be written as

$$[ND_3]\,(t) = \frac{[ND_3]_0}{1 + k_{ND3} \cdot t \cdot [ND_3]_0} \,.$$

(7.8)

To understand the difficulty of colliding two Stark-decelerated molecules, let us calculate the probability of a successful collision of an ammonia molecule with a Stark-decelerated molecular packet of ND_3 with a density of 10^6 molecules/cm^3 and a width of 2 mm. If we assume a total cross section for ND_3-ND_3 collisions of 500 Å^2, the probability of a collision is $P = \sigma_{\mathrm{tot}} \cdot \mathrm{d}x \cdot [ND_3] = 1 \cdot 10^{-8}$. As described above the molecular synchrotron can enhance this signal by a factor of 10^4, such that the observation of such a collision in the molecular synchrotron is within reach.

Because of the low probability of a collision, the expected change of the decay rate due to bi-molecular collisions in the molecular synchrotron is expected to be small. In order to detect this extra loss, the synchrotron is toggled between three different modes.

- First, the ammonia density is measured without counter-propagating packets (WO)

- Secondly, the ammonia density is measured with counter-propagating packets (W)

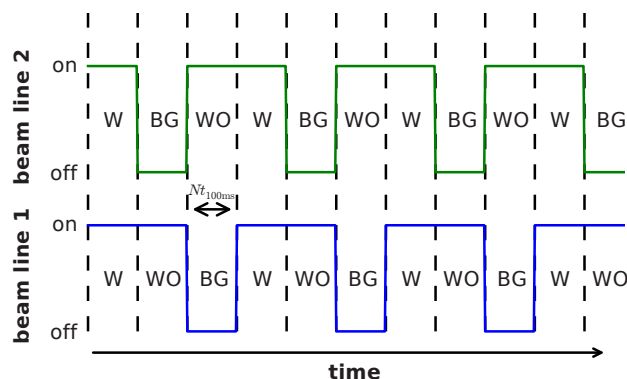- Thirdly, the background ND_3 in the vacuum chamber is determined (BG)

Figure 7.4: The trigger scheme to investigate collisions between counter-propagating packets. To measure the collisions as sensitively as possible the synchrotron is switched between three configurations: beam lines 1 and 2, only beam line 1 or only beam line 2 inject packets into the synchrotron. Additionally, the assignment for each beam line to the collision signal (W, WO and BG) is shown. If a molecule is detected in the W configuration, counter-propagating packets are present. WO stands for 'without' counter-propagating packets. In the background measurement (BG) no molecules from this beam line are injected; only counter-propagating beam revolve in the synchrotron. The time between each configuration is a integer multiple of $t_{100\text{ms}}$.

The measurement without counter-propagating packets is used as a reference to include the effects of the black body radiation and the collisions with the background gas. The normalized collision signal is

$$C_{\text{total}} = \frac{(\text{WO} - \text{BG}) - (\text{W} - \text{BG})}{(\text{WO} - \text{BG})}. \tag{7.9}$$

If C_{total} is clearly greater than zero, bi-molecular collisions occur. From the increase of C_{total} as a function of the number of round trips, a bi-molecular collision rate can be determined.

The main advantage of this toggle mode is that drifts in the supersonic expansion and the detection are compensated. The toggle scheme is sketched in Figure 7.4. As a function of time it shows when the beam lines inject packets of molecules. In one toggle mode only beam line 1 operates, in the second mode only beam line 2 injects packets, while in the last mode the synchrotron confines clockwise and anti-clockwise revolving packets simultaneously. Every time the synchrotron starts a new toggle-mode 1.3 seconds are required to load all packets. The detected molecules in this time period cannot be used for the collision analysis. To assure the continuous operation of the synchrotron the time duration of the toggle mode is a multiple of $t_{100\text{ms}}$. This multiple is chosen such that the ratio of the loading time and the time of one mode is minimal, while also keeping the time of one mode sufficiently short that drifts on relative short time scales are also compensated.
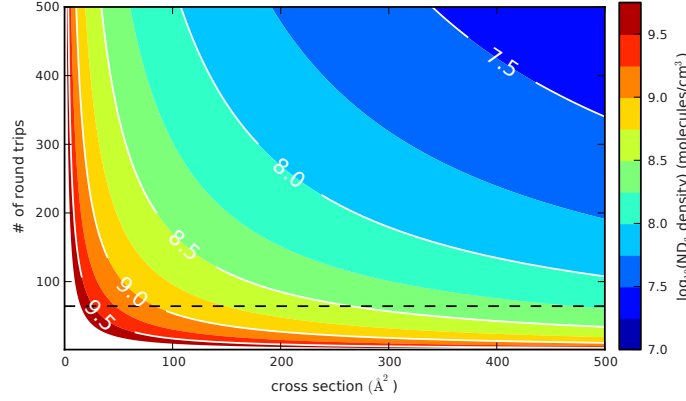
Figure 7.5: The required ND_3 density that is necessary to detect collisions as a function of cross section and number of round trips. In this contour plot 500,000 single simulated measurements are analyzed using a signal-to-noise ratio of 1.2, which will be presented in the next Section for the $64\frac{1}{4}$ round trip (dashed horizontal line). The calculation behind this simulation assumes that a collision signal above the standard error of 3σ can be detected.

Sensitivity of Molecular Collisions   The sensitivity of bi-molecular collisions is highly dependent on the density of the molecular packets. As mentioned above, the density of Stark-decelerated molecules is not well known but is estimated to be on the order of $10^6 - 10^7$ molecules/cm^3. If we assume that the total collision cross section is a few hundred Å^2, is it possible to estimate how many round trips are necessary to measure bi-molecular collisions? In other words: With the current signal-to-noise, how many round trips do the molecular packets have to revolve in the current molecular synchrotron before the value of Equation (7.9) is larger than its single standard deviation? Including the error, Equation (7.9) can be written as

$$C_{\text{total}} \;=\; \frac{(\text{WO} - \text{W}) \pm \sqrt{\Delta\text{WO}^2 + \Delta\text{W}^2 + 2 \cdot \Delta\text{BG}^2}}{(\text{WO} - \text{BG}) \pm \sqrt{\Delta\text{WO}^2 + \Delta\text{BG}^2}} \tag{7.10}$$

$$=\; \frac{x \pm \Delta x}{y \pm \Delta y} \tag{7.11}$$

$$=\; \frac{x}{y} \pm \sqrt{\left(\frac{\Delta x}{y}\right)^2 + \left(\frac{x\Delta y}{y^2}\right)^2}. \tag{7.12}$$

with

$$x = \text{WO} - \text{W}, \qquad \Delta x = \sqrt{\Delta\text{WO}^2 + \Delta\text{W}^2 + 2 \cdot \Delta\text{BG}^2},$$
$$y = \text{WO} - \text{BG} \quad \text{and} \quad \Delta y = \sqrt{\Delta\text{WO}^2 + \Delta\text{BG}^2}.$$

The interaction time t_{interact} a molecular packet with a width of Δs_{width} experiences while it flies through 13 counter-propagating packets is

$$t_{\text{interact}} = \frac{t_{n\text{RT}}}{2 \cdot \pi \cdot (R_{\text{ring}} + r'_{\text{equi}})} \cdot 13 \cdot \Delta s_{\text{width}}. \tag{7.13}$$

Here, $t_{n\text{RT}}$ is the confinement time of a molecular packet and $2 \cdot \pi \cdot (R_{\text{ring}} + r'_{\text{equi}})$ the total circumference. The second order decay rate constant of the bi-molecular collisions is defined as

$$k_{\text{ND3}} = \sigma_{\text{tot}} \cdot v_{\text{rel}}. \tag{7.14}$$

Because C_{total} in Equation (7.9) is normalized, the relative error, δC_{total}, is equal to the absolute error, ΔC_{total}. Bi-molecular collisions are detectable at the threshold where the relative error δC_{total} is equal to the loss of ND_3 via collisions.

$$\Delta C_{\text{total}} = 1 - \frac{[\text{ND}_3](t)}{[\text{ND}_3]_0} = 1 - \frac{1}{1 + k \cdot t \cdot [\text{ND}_3]_0}. \tag{7.15}$$

From Equation (7.15) one can calculate the required ND_3 intensity to detect bi-molecular collisions

$$[\text{ND}_3](t) = \frac{\Delta C_{\text{total}}}{(1 - \Delta C_{\text{total}}) \cdot k_{\text{ND3}} \cdot t_{\text{interact}}}. \tag{7.16}$$

Using a signal-to-noise ratio equal to 1.2 (the measurement where this value is obtained will be presented in the next Section), one can simulate the three toggle modes. The absolute error is determined by simulating 500,000 single events and calculating the corresponding errors. With a repetition rate of $10\,\text{Hz}$ this measurement would take about 14 hours. The average loss is assumed to be 10^{-4}. If the derived error is larger than the standard error of 3σ one can use Equation (7.16) to determine the necessary density as a function of cross section and number of round trips. The result is shown in Figure 7.5, where the required ND_3 density is shown as a function of total collision cross section (horizontal axis) and number of round trips (vertical axis). A signal-to-noise ratio of 1.2 was used, which will be presented in the next Section for the $64\frac{1}{4}$ round trip (dashed horizontal line). To detect a decay due to bi-molecular collisions in 64 round trips would require an ammonia density of $3.5 \cdot 10^8$ molecules/cm^3 assuming a total cross section of $300\,\text{Å}^2$.

A First Collision Test   In order to use the determined collision signal of Equation (7.9) for analysis, the ND_3 intensity has to be assigned correctly to one of the two injection beam lines. At certain numbers of round trips this is not possible; particularly when the counter-propagating packets overlap in the detection zone. For example the 40th round trip cannot be used, because it overlaps with the quarter round trip from the other beam line. For this reason, only round trips 0 to 39 and 64 1/4 to 103 1/4 can be used for the collision analysis. In the first series of round trips the molecules are detected at the same point where they were injected. In the latter series, the detection and the injection point are different (exactly one quarter round trip further). Dependent on which number
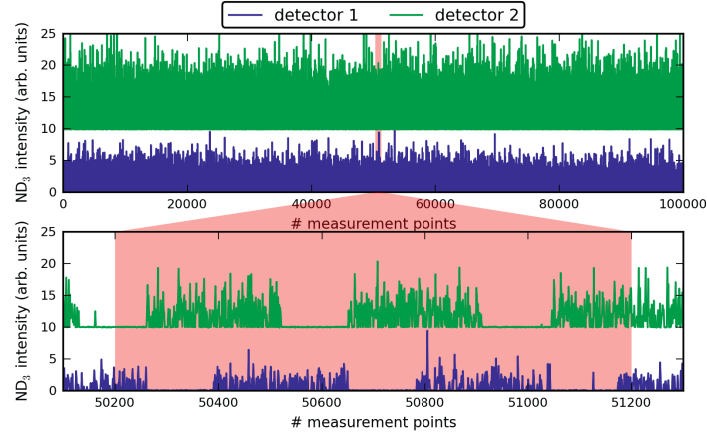
Figure 7.6: An example measurement to determine collisions between counter-propagating packets of ND$_3$ molecules. The top Panel shows a 100 000 single shot measurement in which a packet of molecules traveled $64\frac{1}{4}$ round trips while the trigger scheme described in Figure 7.4 was applied. The lower Panel shows an zoom-in of the of the Panel above. The switching trigger scheme is directly visible.

of round trip is investigated in the toggle mode the assignment of the detector 1 and 2 changes.

Figure 7.6 shows a toggle measurement in which ammonia molecules were confined for $64\frac{1}{4}$ round trips in the molecular synchrotron. The upper Panel shows the ND$_3$ intensity for all 100 000 single measurements. The total measurement time was 2.8 hours. The signal of detector 1 and 2 is shown in blue and green, respectively. The lower Panel shows an inset of the two data traces in which the toggle mode in clearly visible. The signal-to-noise ratio of the upper trace is 1.2. The result of the data analysis for beam line 1 and 2 of Figure 7.6 is shown in upper and lower Panel of Figure 7.7, respectively. The horizontal axis indicates the number of toggle cycles while the vertical axis shows the averaged ND$_3$ signal for the three different modes. The red data trace shows the averaged ammonia signal without collisions and the black trace with counter-propagating packets. The green measurement is a background measurement. In the analysis the first nine points of each cycle for which the loading of the molecular synchrotron was not yet completed were neglected. The total averaged signal and the corresponding variances over all cycles is shown for each trace as a dashed and dotted line, respectively. Additionally they are also listed in Table 7.1. This example illustrates that the noise in the experiment is currently too large to detect collisions.

Future Improvement of the Molecular Synchrotron   The result of the Paragraph above leads directly to the question of what improvements can be made to the molecular synchrotron in order to be able to detect collisions of counter-propagating packets. Every
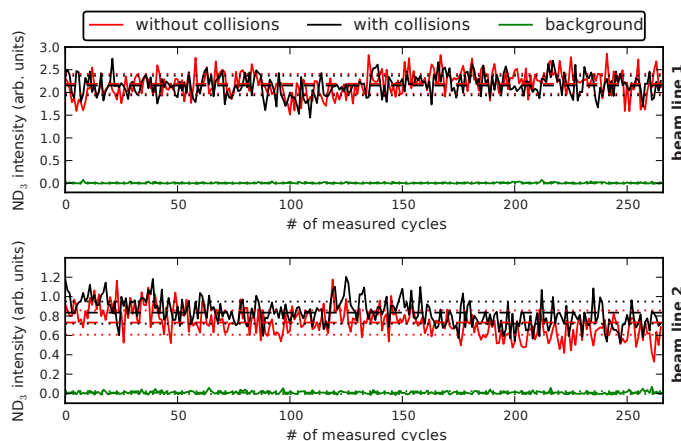
Figure 7.7: In this figure the averaged ND_3 signal is shown a function of measurement cycles using the data of Figure 7.6. The top and the bottom Panel show the analyzed result for beam line 1 and beam line 2, respectively. In each Panel the data with collisions, without collisions and with background are shown in red, black and green, respectively. The dotted lines show the corresponding statistical error $(1 \cdot \sigma)$.

	beam line 1	beam line 2
W	(2.15 ± 0.22)	(0.83 ± 0.12)
WO	(2.19 ± 0.22)	(0.73 ± 0.13)
BG	(0.01 ± 0.02)	(0.01 ± 0.02)

Table 7.1: Result of the statistical analysis of Figure 7.7 for the two beam lines.

improvement that increases the lifetime of a molecular packet automatically improves the signal-to-noise ratio. One obvious way to increase the lifetime is to cool the molecular synchrotron to liquid nitrogen temperature. By this, the loss due to the black body radiation is reduced by a factor of 22; the decay rate of the black body process drops from $0.14 \, \text{s}^{-1}$ at room temperature to $0.0063 \, \text{s}^{-1}$ at $77 \, \text{K}$ [69]. A beneficial side effect is that the cooling leads to a lower pressure in the vacuum chamber. A device that shields the molecules from the black body radiation would at the same time function as a cold finger. Background gas will stick on the cold surface, decreasing the density of the background gas. The lifetime of the molecules confined in the synchrotron would increase significantly. Although this idea is straightforward, its implementation is not. It is mechanically and electronically highly demanding to operate a cooled molecular synchrotron. The ground potential of a cooling shield would be only a few millimeters away from electrodes or wires that are on high voltage. This may cause additional discharges that might make it impossible to operate the molecular synchrotron. Petrik
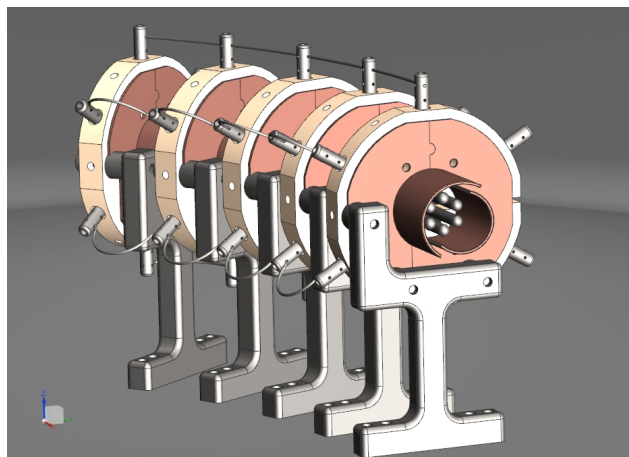
Figure 7.8: A photo realistic image of five selected hexapole segments together with the copper shield. Each shield consists of two cylindrical half tubes which encase the electrodes. A copper plate on each side of the aluminum oxide disc cools the center part of a hexapole segment. The distance between the copper shields and the electrodes is 2.5 mm.

Bischoff and Peter Geng, two technicians from the Fritz Haber Institute, designed, built and successfully tested such a two hexapole segment of the molecular synchrotron. A photo realistic image of the test setup consisting of five hexapole segments together with the copper shields can be seen in Figure 7.8. On each side of the aluminum oxide disc a copper plate cools the entire holder. The electrodes are covered by two copper half tubes. The shape is made such that there is no direct path between the molecules in the synchrotron and the vacuum chamber (to minimize the black body radiation), but so that there is still a gap left through which the background gas can be pumped out. To date the setup was cooled down to 150 K and a voltage difference of 8 kV was applied; but so far not at the same time.

An enhancement of ND_3 signal could also be achieved by making the potential well in the synchrotron deeper. Especially, a higher transverse trapping frequencies (ω_r and ω_y) will increase the density of the trapped packet and, by this, increase the probability of collisions. A higher longitudinal trapping frequency will not automatically lead to a higher collision signal but will increase the signal-to-noise ratio. Chapter 8 will describe and analyze such a new design.

Another way to improve the sensitivity would be to implement velocity map imaging (VMI) [75]. By applying the correct extraction voltages on the detection electrodes one could separate the clockwise and anti-clockwise revolving packets in the time-of-flight tube. The two separated packets would collide with a position sensitive micro channel plate (MCP). By placing a phosphor screen and a camera behind the MCP, the detected ions can be made visible. This technique leads to a background reduction;

significantly increasing the signal-to-noise of the experiment. A beneficial side effect of the implementation of a VMI technique would be that counter-propagating packets between round trip 40 and 64 could be separated and their signal could be used for the collision analysis.
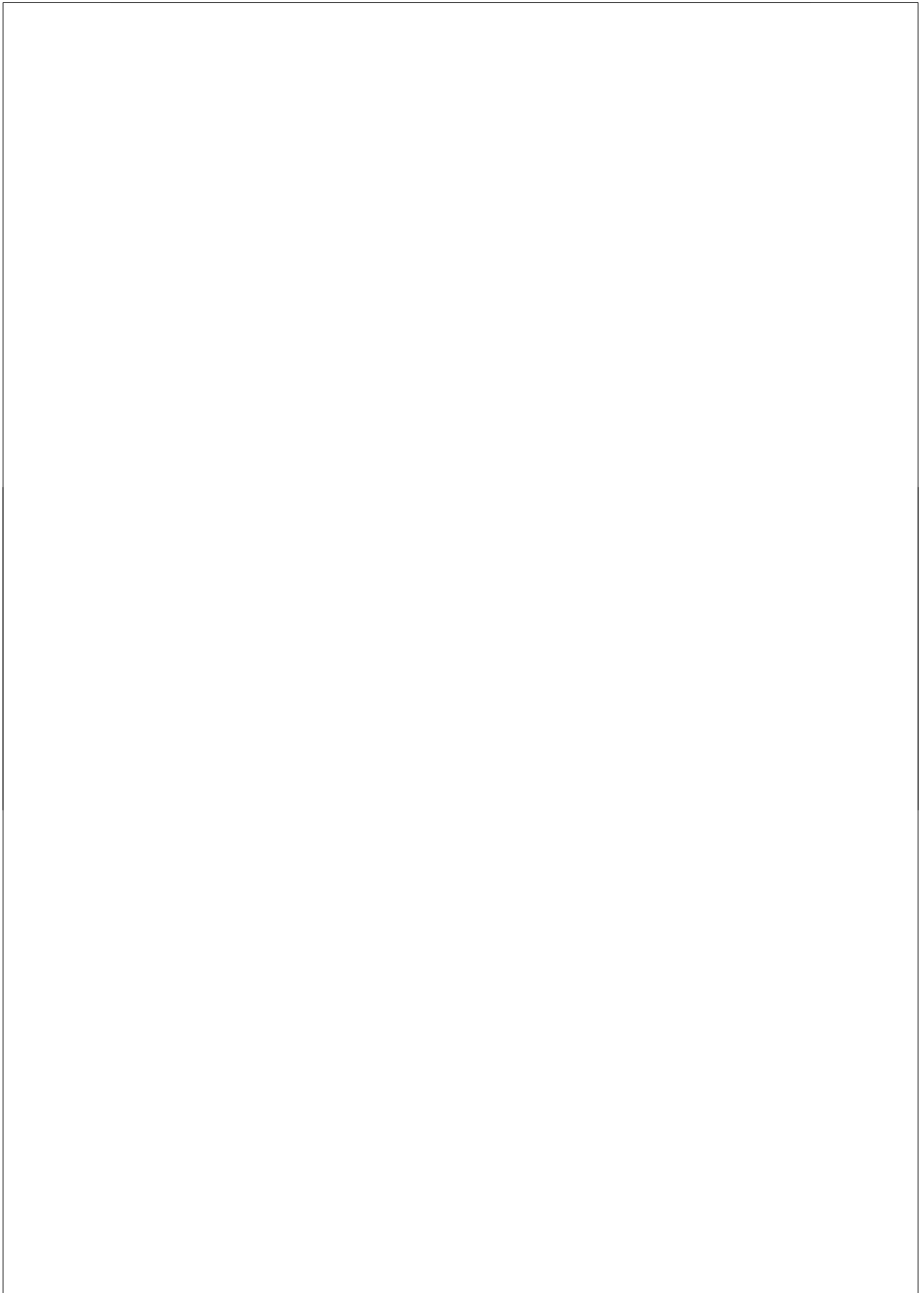
Chapter 8

Outlook on an Improved Molecular Synchrotron

8.1 Introduction

As discussed in the introduction, the molecular synchrotron described in this thesis is the third generation storage ring for neutral molecules built in our lab. It has naturally evolved out of earlier work on a synchrotron composed of two half rings [23], which itself evolved out of work on a storage ring made from a straight hexapole that was bent into a circle [24]. The designs of all three types relied on the hexapole geometry that was then adapted to confine molecules in two or three directions. This Chapter will describe a different approach: Rather than starting with a certain geometry it might be advantageous to start with the 'design' of the electric field. The effect of the centrifugal distortion and the relatively weak confining force in the longitudinal direction should be included in the design of the field. The exact shape of the electrodes follows from the derived electric field. It is our hope to find a new geometry that is simpler to construct and that requires simpler electronics.

This Chapter uses the theory of the paper "On deflection fields, weak-focusing and strong-focusing storage rings for polar molecules" by de Nijs and Bethlem [76]. They use the expansion coefficients of a multipole expansion to describe analytically the transverse force that a molecule experiences in the storage ring. This Chapter aims to use their theoretical approach to determine the best expansion coefficients for the next version of the molecular synchrotron. The theory incorporated in this Section is partially reproduced from [76]. Subsequently, the expansion coefficients are linked to the transverse trapping frequencies. Afterwards the derived frequencies are compared with characteristic frequencies of the 40-piece molecular synchrotron. At the end of the Chapter the longitudinal confinement and the possibility to realize a new design are discussed.

8.2 Mathematical Description

If we assume that the radius of a new molecular synchrotron R_{ring} is large compared to the size of the electrode structure r_0, we can expand the electric field in terms of polar coordinates. As in Chapter 4, r' and y define the radial and vertical directions, respectively. Using $r = \sqrt{(r'^2 + y^2)}$ and $\theta = \arctan{(y/r')}$ the electrostatic potential Φ

can be represented by a multipole expansion [77, 78, 76].

$$\Phi(r',y) = \Phi_0 \left(\sum_{n=1}^{\infty} \frac{a_n}{n} \left(\frac{r}{r_0} \right)^n \cos(n\theta) + \sum_{n=1}^{\infty} \frac{b_n}{n} \left(\frac{r}{r_0} \right)^n \sin(n\theta) \right). \tag{8.1}$$

Here, Φ_0 is the applied voltage, while a_n and b_n are dimensionless constants. The first, second and third term of Equation (8.1) ($n = 1, 2$ and 3) describe the dipole, the quadrupole and the hexapole field, respectively. Now suitable coefficients need to be obtained to make a new improved version of a molecular synchrotron. For a good confinement three electric fields types are necessary: The quadrupole term is required to compensate the centrifugal force. The hexapole term acts as a focusing force. Furthermore, the dipole term is needed to bunch molecules in the longitudinal direction as well as to avoid losses due to Majorana transitions. The required field can be created by using either a_n or b_n terms, but it seems easier to inject and detect molecules in an electrode configurations based on b_n terms. Consequently, we choose to set all $a_n = 0$, and retain only b_1, b_2 and b_3.

The first three terms of Equation (8.1) are

$$\Phi(r',y) = \Phi_0 \left(b_1 \frac{y}{r_0} + b_2 \frac{r'y}{r_0^2} + \frac{b_3}{3} \frac{(3yr'^2 - y^3)}{r_0^3} \right). \tag{8.2}$$

The electric field can be calculated via

$$\vec{E} = -\vec{\nabla}\Phi. \tag{8.3}$$

The magnitude of the electric fields is

$$E(r',y) = \sqrt{\left(\frac{\partial \Phi}{\partial r'} \right)^2 + \left(\frac{\partial \Phi}{\partial y} \right)^2}. \tag{8.4}$$

At the equilibrium orbit ($r' = 0$ and $y = 0$) the magnitude becomes

$$E_0 = \frac{\Phi_0}{r_0} b_1. \tag{8.5}$$

In a first approximation the Stark energy, *e.g.*, of ammonia molecules, increases linearly with the magnitude of the electric field

$$W = -\mu_{\text{eff}} \cdot E, \tag{8.6}$$

where μ_{eff} is the effective dipole moment of the molecule in the electric field at the equilibrium orbit. This molecule experiences a force

$$\vec{F}(\vec{r}) = -\vec{\nabla}W(E) = \mu_{\text{eff}} \vec{\nabla}E. \tag{8.7}$$

Combining Equation (8.2) and Equation (8.7) the two transverse components of the forces can be calculated. For $r < r_0$ we can expand the result as a series and neglect higher order terms. The force in the radial direction is

$$F_{\text{Stark},r'} = \mu_{\text{eff}} E_0 \left[\frac{b_2}{b_1} \frac{1}{r_0} + 2 \frac{b_3}{b_1} \frac{r'}{r_0^2} - \left(\frac{1}{2} \left(\frac{b_2}{b_1} \right)^3 - 2 \frac{b_2}{b_1} \frac{b_3}{b_1} \right) \frac{y^2}{r_0^3} + \dots \right], \qquad (8.8)$$

and the force in the vertical direction is

$$F_{\text{Stark},y} = \mu_{\text{eff}} E_0 \left[\left(\left(\frac{b_2}{b_1} \right)^2 - 2 \frac{b_3}{b_1} \right) \frac{y}{r_0^2} - \left(\left(\frac{b_2}{b_1} \right)^3 - 4 \frac{b_2}{b_1} \frac{b_3}{b_1} \right) \frac{r'y}{r_0^3} + \dots \right]. \qquad (8.9)$$

In analogy to cyclotrons [66], de Nijs and Bethlem introduce a so-called field index n

$$n(r) = -\frac{\partial F_{\text{Stark}} / F_{\text{Stark}}}{\partial r / r} = -\frac{r}{F_{\text{Stark}}} \frac{\partial F_{\text{Stark}}}{\partial r} \qquad (8.10)$$

using the force

$$F_{\text{Stark}} = \sqrt{F_{\text{Stark,r'}}^2 + F_{\text{Stark,y}}^2}. \qquad (8.11)$$

At $r = R_{\text{ring}}$ the field index can be written as

$$n(r = R_{\text{ring}}) = -2 \frac{b_3}{b_2} \frac{R_{\text{ring}}}{r_0}. \qquad (8.12)$$

To restrict the values of b_1, b_2 and b_3 two conditions need to be fulfilled to obtain a stable confinement. First, the force at the equilibrium orbit has to be zero. Secondly, for small r' and y the force has to increase linearly with increasing distance. The total force in the radial direction is the sum of the force of Equation (8.8) and the centrifugal force of the revolving molecule.

$$
\begin{aligned}
F_{r'} &= F_{\text{centri}} + F_{\text{Stark},r'} \\
&= \frac{mv_\phi^2}{R_{\text{ring}} + r'} + \mu_{\text{eff}} E_0 \left(\frac{b_2}{b_1} \frac{1}{r_0} + 2 \frac{b_3}{b_1} \frac{r'}{r_0^2} \right) \\
&= \frac{mv_\phi^2}{R_{\text{ring}}} \left(1 - \frac{r'}{R_{\text{ring}}} \right) + \mu_{\text{eff}} E_0 \left(\frac{b_2}{b_1} \frac{1}{r_0} + 2 \frac{b_3}{b_1} \frac{r'}{r_0^2} \right) \\
&= \left(\frac{mv_\phi^2}{R_{\text{ring}}} + \mu_{\text{eff}} E_0 \frac{b_2}{b_1} \frac{1}{r_0} \right) - \left(\frac{mv_\phi^2}{R_{\text{ring}}^2} - 2\mu_{\text{eff}} E_0 \frac{b_3}{b_1} \frac{1}{r_0^2} \right) r'.
\end{aligned}
\qquad (8.13)
$$

Here, v_ϕ is the longitudinal velocity. In the vertical direction Equation (8.9) simplifies to

$$F_{\text{Stark},y} = \mu_{\text{eff}} E_0 \left(\left(\frac{b_2}{b_1} \right)^2 - 2 \frac{b_3}{b_1} \right) \frac{1}{r_0^2} y. \qquad (8.14)$$

For $r' = 0$ and $y = 0$ both force components have to become zero (first condition). For Equation (8.13), this is only the case, if

$$\frac{b_2}{b_1} = -\frac{m v_\phi^2}{\mu_{\text{eff}} E_0} \frac{r_0}{R_{\text{ring}}}. \tag{8.15}$$

The second stability condition requires that the force can be expressed as $F = -k \cdot x$. The radial and vertical force become

$$F_{r'} = -k_{r'} r' = -\left(\frac{m v_\phi^2}{R_{\text{ring}}^2} - 2\mu_{\text{eff}} E_0 \frac{b_3}{b_1} \frac{1}{r_0^2} \right) r' \tag{8.16}$$

and

$$F_y \equiv -k_y y = \mu_{\text{eff}} E_0 \left(\left(\frac{b_2}{b_1} \right)^2 - 2\frac{b_3}{b_1} \right) \frac{1}{r_0^2} y, \tag{8.17}$$

respectively. The angular frequencies in both directions are

$$\omega_{r'} = \sqrt{\frac{k_{r'}}{m}} = \sqrt{\frac{v_\phi^2}{R_{\text{ring}}^2} - 2\frac{\mu_{\text{eff}} E_0}{m} \frac{b_3}{b_1} \frac{1}{r_0^2}}$$
$$= \Omega_{\text{cycl}} \sqrt{1 - n} \tag{8.18}$$

and

$$\omega_y = \sqrt{\frac{k_y}{m}} = \sqrt{-\frac{\mu_{\text{eff}} E_0}{m} \left[\left(\frac{b_2}{b_1} \right)^2 - 2\frac{b_3}{b_1} \right] \frac{1}{r_0^2}}$$
$$= \Omega_{\text{cycl}} \sqrt{n - \frac{m v_\phi^2}{\mu_{\text{eff}} E_0}}. \tag{8.19}$$

Here, $\Omega_{\text{cycl}} = v_\phi / R_{\text{ring}}$ is cyclotron frequency.

A molecule is only confined if the characteristic frequencies in both directions are real. This means that

$$\frac{m v_\phi^2}{\mu_{\text{eff}} E_0} < n < 1. \tag{8.20}$$

Low-field seeking states have a negative effective dipole moment and thus can always be stored in a molecular synchrotron, if n is chosen correctly and if Equation (8.15) is fulfilled, *i.e.*, as long as the ring is sufficiently large.

8.3 Describing the Current Molecular Synchrotron

For a synchrotron of a given radius R_{ring} and aperture r_0, Equations (8.15), (8.18) and (8.19) link the expansion coefficients to the velocity that is confined and to the trap

frequencies. Let us first calculate the betatron frequencies for the current synchrotron. To use Equations (8.18) and (8.19), we need to know the expansion coefficients of the hexapole field used in the current setup when it is expanded around the equilibrium orbit. These are found by writing the electrostatic potential as:

$$
\begin{aligned}
\Phi(r', y) &= \Phi_0 \left[b_3^* \frac{3r^{*\prime 2}y^* - y^{*3}}{3r_0^3} \right] \\
&= \Phi_0 \left[b_3^* \frac{3(r' + r'_{\text{equi}})^2 y - y^3}{3r_0^3} \right] \\
&= \Phi_0 \left[b_3^* \left(\frac{r'_{\text{equi}}}{r_0} \right)^2 \left(\frac{y}{r_0} \right) + 2b_3^* \left(\frac{r'_{\text{equi}}}{r_0} \right) \left(\frac{r'x}{r_0^2} \right) + b_3^* \left(\frac{3r'^2 y - y^3}{3r_0^3} \right) \right] \\
&= \Phi_0 \left[b_1 \left(\frac{r'}{r_0} \right) + b_2 \left(\frac{r'y}{r_0^2} \right) + b_3 \left(\frac{3r'^2 y - y^3}{3r_0^3} \right) \right],
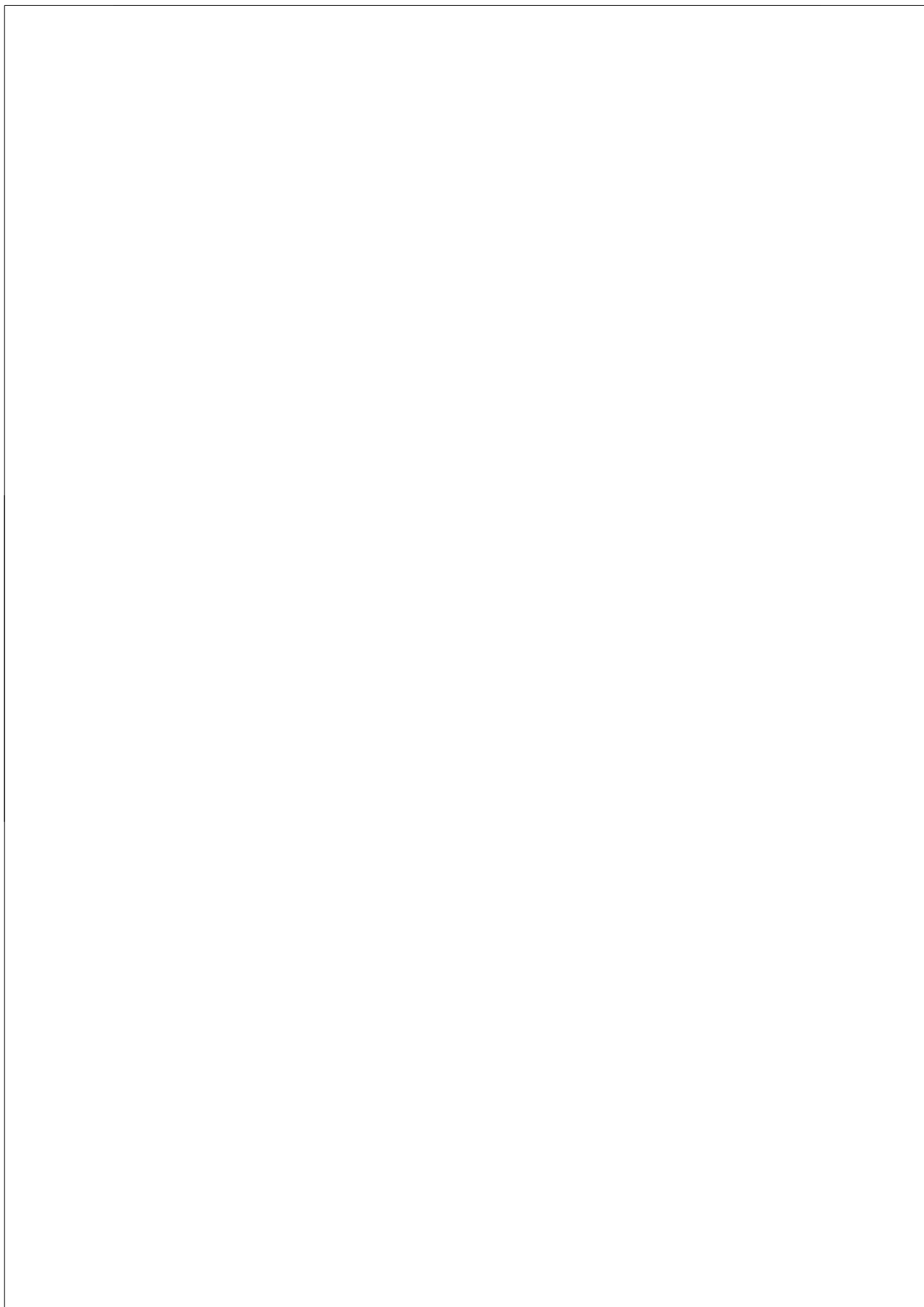\end{aligned}
\tag{8.21}
$$

where $r^{*\prime}$ and b_3^* are defined with respect to the geometric center of the hexapoles, while r', b_1, b_2 and b_3 are defined with respect to the equilibrium radius with

$$
r^{*\prime} = r' + r'_{\text{equi}}.
\tag{8.22}
$$

Assuming a voltage difference of $6\,\text{kV}$ between adjacent rods of the hexapole, *i.e.*, $b_3^* \Phi_0 = 9\,\text{kV}$, a velocity, $v_\phi = 124.3\,\text{m/s}$, $r_0 = 3.54\,\text{mm}$, $R_{\text{ring}} = 250\,\text{mm}$ and an effective dipole moment, $\mu_{\text{eff}} = 0.124\,\text{cm}^{-1}/(\text{kV/cm})$, we find $b_1 \Phi_0 = 3.0\,\text{kV}$, $b_2 \Phi_0 = 10.4\,\text{kV}$, $b_3 \Phi_0 = 9\,\text{kV}$, $r'_{\text{equi}} = 2.0\,\text{mm}$, $n = -124$, $\omega_r/(2\pi) = 880\,\text{Hz}$ and $\omega_y/(2\pi) = 870\,\text{Hz}$, in good agreement with the values found in Chapter 5 and 6.

8.4 An Approach for a New Electrode Design

This Chapter linked the expansion coefficients to the important parameters in the synchrotron. The next step is to systematically vary the coefficients and look for a combination that results in a synchrotron of similar size that can store molecules with similar velocities but that has a larger acceptance, that is easier to construct, or that requires simpler electronics. Somewhat disappointingly an, admittedly rather brief, survey of the parameter space did not result in such a combination. In fact, it appears that a hexapole geometry, approximated by circular rods, is most favorable in terms of acceptance, construction and required electronics. Further research is needed to confirm this conclusion.

Bibliography

[1] E. S. Shuman, J. F. Barry, and D. DeMille, *Laser cooling of a diatomic molecule*, Nature, **467**, 820–823 (2010).

[2] J. M. Doyle, B. Friedrich, J. Kim, and D. Patterson, *Buffer-gas loading of atoms and molecules into a magnetic trap*, Physical Review A, **52**, R2515–R2518 (1995).

[3] S. Y. T. van de Meerakker, H. L. Bethlem, N. Vanhaecke, and G. Meijer, *Manipulation and Control of Molecular Beams*, Chemical Reviews, **112**, 4828–4878 (2012).

[4] D. H. Levy, *The Spectroscopy of Very Cold Gases*, Science, **214**, 545–553 (1981).

[5] H. L. Bethlem, G. Berden, and G. Meijer, *Decelerating Neutral Dipolar Molecules*, Physical Review Letters, **83**, 1558–1561 (1999).

[6] H. L. Bethlem, G. Berden, F. M. H. Crompvoets, R. T. Jongma, A. J. A. van Roij, and G. Meijer, *Electrostatic trapping of ammonia molecules*, Nature, **406**, 491–494 (2000).

[7] N. Vanhaecke, U. Meier, M. Andrist, B. H. Meier, and F. Merkt, *Multistage Zeeman deceleration of hydrogen atoms*, Physical Review A, **75**, 031402 (2007).

[8] E. Narevicius, A. Libson, C. G. Parthey, I. Chavez, J. Narevicius, U. Even, and M. G. Raizen, *Stopping supersonic oxygen with a series of pulsed electromagnetic coils: A molecular coilgun*, Physical Review A, **77**, 051401 (2008).

[9] R. Krems, B. Friedrich, and W. C. Stwalley, *Cold Molecules: Theory, Experiment, Applications*, CRC Press, first edition (2009), ISBN 9781420059038.

[10] I. W. M. Smith, *Low Temperatures and Cold Molecules*, Imperial College Press (2008), ISBN 9781848162099.

[11] J. van Veldhoven, J. Küpper, H. L. Bethlem, B. Sartakov, A. J. A. van Roij, and G. Meijer, *Decelerated molecular beams for high-resolution spectroscopy*, European Physical Journal D, **31**, 337–349 (2004).

[12] E. R. Hudson, H. J. Lewandowski, B. C. Sawyer, and J. Ye, *Cold Molecule Spectroscopy for Constraining the Evolution of the Fine Structure Constant*, Physical Review Letters, **96**, 143004 (2006).

[13] H. L. Bethlem, M. Kajita, B. Sartakov, G. Meijer, and W. Ubachs, *Prospects for precision measurements on ammonia molecules in a fountain*, European Physical Journal - Special Topics, **163**, 55–69 (2008).

[14] M. R. Tarbutt, J. J. Hudson, B. E. Sauer, and E. A. Hinds, *Prospects for measuring the electric dipole moment of the electron using electrically trapped polar molecules*, Faraday Discussion, **142**, 37–56 (2009).

[15] N. Balakrishnan, A. Dalgarno, and R. C. Forrey, *Vibrational relaxation of CO by collisions with ^4He at ultracold temperatures*, Journal of Chemical Physics, **113**, 621–626 (2000).

[16] R. V. Krems, *Molecules near absolute zero and external field control of atomic and molecular dynamics*, International Reviews in Physical Chemistry, **24**, 99–118 (2005).

[17] R. V. Krems, *Cold controlled chemistry*, Physical Chemistry Chemical Physics, **10**, 4079–4092 (2008).

[18] J. J. Gilijamse, S. Hoekstra, S. Y. T. van de Meerakker, G. C. Groenenboom, and G. Meijer, *Near-Threshold Inelastic Collisions Using Molecular Beams with a Tunable Velocity*, Science, **313**, 1617–1620 (2006).

[19] L. Scharfenberg, J. Kłos, P. J. Dagdigian, M. H. Alexander, G. Meijer, and S. Y. T. van de Meerakker, *State-to-state inelastic scattering of Stark-decelerated OH radicals with Ar atoms*, Physical Chemistry Chemical Physics, **12**, 10660–10670 (2010).

[20] M. Kirste, L. Scharfenberg, J. Kłos, F. Lique, M. H. Alexander, G. Meijer, and S. Y. T. van de Meerakker, *Low-energy inelastic collisions of OH radicals with He atoms and D_2 molecules*, Physical Review A, **82**, 042717 (2010).

[21] M. Kirste, X. Wang, H. C. Schewe, G. Meijer, K. Liu, A. van der Avoird, L. M. Janssen, K. B. Gubbels, G. C. Groenenboom, and S. Y. van de Meerakker, *Quantum-state resolved bi-molecular collisions of velocity-controlled OH with NO radicals*, Science (accepted).

[22] F. M. H. Crompvoets, *A Storage Ring For Neutral Molecules*, Ph.D. thesis, Radboud Universiteit Nijmegen (2005).

[23] C. E. Heiner, D. Carty, G. Meijer, and H. L. Bethlem, *A Molecular Synchrotron*, Nature Physics, **3**, 115–118 (2007).

[24] F. M. H. Crompvoets, H. L. Bethlem, R. T. Jongma, and G. Meijer, *A prototype storage ring for neutral molecules*, Nature, **411**, 174–176 (2001).

[25] C. E. Heiner, H. L. Bethlem, and G. Meijer, *A synchrotron for neutral molecules*, Chemical Physics Letters, **473**, 1–9 (2009).

[26] C. E. Heiner, *A Molecular Synchrotron*, Ph.D. thesis, Radboud Universiteit Nijmegen (2009).

[27] M. Appl, *Ammonia: Principles and Industrial Practice*, Wiley-VCH Verlag GmbH (1999), ISBN 978-3527295933.

[28] G. Herzberg, *Molecular Spectra and Molecular Structure: Infrared and Raman Spectra of Polyatomic Molecules*, Krieger Pub Co (1991), ISBN 9780894642692.

[29] W. Demtröder, *Molecular Physics: Theoretical Principles and Experimental Methods*, Wiley-VCH (2006), ISBN 3527405666.

[30] Š. Urban, R. D'Cunha, K. N. Rao, and D. Papoušek, *The $\Delta k = \pm 2$ "forbidden band" and inversion-rotation energy levels of ammonia*, Canadian Journal of Physics, **62**, 1775–1791 (1984).

[31] L. Fusina, G. D. Lonardo, and J. Johns, *The ν_2 and ν_4 bands of $^{14}ND_3$*, Journal of Molecular Spectroscopy, **118**, 397–423 (1986).

[32] D. M. Dennison and G. E. Uhlenbeck, *The Two-Minima Problem and the Ammonia Molecule*, Physical Review, **41**, 313–321 (1932).

[33] N. Rosen and P. M. Morse, *On the Vibrations of Polyatomic Molecules*, Physical Review, **42**, 210–217 (1932).

[34] J. D. Swalen and J. A. Ibers, *Potential Function for the Inversion of Ammonia*, Journal of Chemical Physics, **36**, 1914–1918 (1962).

[35] K. Shimoda, Y. Ueda, and J. Iwahori, *Infrared laser stark spectroscopy of ammonia*, Applied Physics A, **21**, 181–189 (1980).

[36] S. R. Gandhi and R. B. Bernstein, *Focusing and state selection of NH_3 and OCS by the electrostatic hexapole via first- and second-order Stark effects*, Journal of Chemical Physics, **87**, 6457–6467 (1987).

[37] G. Scoles, *Atomic and Molecular Beam Methods: Volume 1*, Oxford University Press, USA (1988), ISBN 0195042808.

[38] W. Gerlach and O. Stern, *Der experimentelle Nachweis der Richtungsquantelung im Magnetfeld*, Zeitschrift für Physik A Hadrons and Nuclei, **9**, 349–352 (1922).

[39] J. P. Gordon, H. J. Zeiger, and C. H. Townes, *Molecular Microwave Oscillator and New Hyperfine Structure in the Microwave Spectrum of NH_3*, Physical Review, **95**, 282–284 (1954).

[40] J. P. Gordon, H. J. Zeiger, and C. H. Townes, *The Maser – New Type of Microwave Amplifier, Frequency Standard, and Spectrometer*, Physical Review, **99**, 1264–1274 (1955).

[41] W. Demtröder and H.-J. Foth, *Molekülspektroskopie in kalten Düsenstrahlen*, Physikalische Blätter, **3**, 7–13 (1987).

[42] W. Ketterle, *Nobel lecture: When atoms behave as waves: Bose-Einstein condensation and the atom laser*, Reviews of Modern Physics, **74**, 1131–1151 (2002).

[43] B. Sartakov, *The population of rotational levels of $v_2 = 0, a/s$ states of X^1A_1' of $^{14}ND_3$ at T=293K* (2011), private communication.

[44] H. L. Bethlem, *Deceleration and Trapping of Polar Molecules using Time-Varying Electric Fields*, Ph.D. thesis, Radboud Universiteit Nijmegen (2002).

[45] S. Y. T. van de Meerakker, *Deceleration and Electrostatic Trapping of OH-Radicals*, Ph.D. thesis, Radboud Universiteit Nijmegen (2006).

[46] H. L. Bethlem, F. M. H. Crompvoets, R. T. Jongma, S. Y. T. van de Meerakker, and G. Meijer, *Deceleration and trapping of ammonia using time-varying electric fields*, Physical Review A, **65**, 053416 (2002).

[47] S. Y. T. van de Meerakker, N. Vanhaecke, H. L. Bethlem, and G. Meijer, *Transverse stability in a Stark decelerator*, Physical Review A, **73**, 023401 (2006).

[48] L. Scharfenberg, H. Haak, G. Meijer, and S. Y. T. van de Meerakker, *Operation of a Stark decelerator with optimum acceptance*, Physical Review A, **79**, 023410 (2009).

[49] A. Osterwalder, S. A. Meek, G. Hammer, H. Haak, and G. Meijer, *Deceleration of neutral molecules in macroscopic traveling traps*, Physical Review A, **81**, 051401 (2010).

[50] C. E. Heiner, H. L. Bethlem, and G. Meijer, *Molecular beams with a tunable velocity*, Physical Chemistry Chemical Physics, **8**, 2666–2676 (2006).

[51] H. G. Bennewitz, W. Paul, and C. Schlier, *Fokussierung polarer Moleküle*, Zeitschrift für Physik A Hadrons and Nuclei, **141**, 6–15 (1955).

[52] R. Anderson, *Tracks of Symmetric Top Molecules in Hexapole Electric Fields*, Journal of Physical Chemistry A, **101**, 7664–7673 (1997).

[53] D. Gerlich, *Inhomogenuous RF Fields: A Versatile Tool of the Study of Processes with slow Ions*, Wiley-Interscience (1992), ISBN 0471532584.

[54] P. C. Zieger, S. Y. T. van de Meerakker, C. E. Heiner, H. L. Bethlem, A. J. A. van Roij, and G. Meijer, *Multiple Packets of Neutral Molecules Revolving for over a Mile*, Physical Review Letters, **105**, 173001 (2010).

[55] T. E. Wall, S. K. Tokunaga, E. A. Hinds, and M. R. Tarbutt, *Nonadiabatic transitions in a Stark decelerator*, Physical Review A, **81**, 033414 (2010).

[56] M. Kirste, B. G. Sartakov, M. Schnell, and G. Meijer, *Nonadiabatic transitions in electrostatically trapped ammonia molecules*, Physical Review A, **79**, 051401 (2009).

[57] U. Hoppe, H. Junkes, C. Tschentscher, and J. Küpper, *Cold molecules data aquisition – KouDA* (2003–2012).

[58] M. N. R. Ashfold, R. N. Dixon, N. Little, R. J. Stickland, and C. M. Western, *The $\tilde{B}^1E''$ state of ammonia: Sub-Doppler spectroscopy at vacuum ultraviolet energies*, Journal of Chemical Physics, **89**, 1754–1761 (1988).

[59] Spectra-Physics, *Quanta-Ray PRO-Series Pulsed Nd:YAG Lasers* (2002).

[60] W. C. Wiley and I. H. McLaren, *Time-of-Flight Mass Spectrometer with Improved Resolution*, Review of Scientific Instruments, **26**, 1150–1157 (1955).

[61] T. E. Adams, B. H. Rockney, R. J. S. Morrison, and E. R. Grant, *Convenient fast pulsed molecular beam valve*, Review of Scientific Instruments, **52**, 1469–1472 (1981).

[62] W. R. Gentry and C. F. Giese, *Ten-microsecond pulsed molecular beam source and a fast ionization detector*, Review of Scientific Instruments, **49**, 595–600 (1978).

[63] J. H. Blokland, *Comparison of the Jordan and General Valve* (2011), private communication.

[64] D. A. Dahl, *Simion 3D Version 8.0* (1995).

[65] F. M. H. Crompvoets, H. L. Bethlem, and G. Meijer, *A Storage Ring for Neutral Molecules*, volume 52 of *Advances In Atomic, Molecular, and Optical Physics*, 209–287, Academic Press (2005).

[66] M. Conte and W. W. MacKay, *An Introduction to the Physics of Particle Accelerators*, second edition (2008), ISBN 109812779612.

[67] C. E. Heiner, G. Meijer, and H. L. Bethlem, *Motional resonances in a molecular synchrotron*, Physical Review A, **78**, 030702 (2008).

[68] Behlke Power Electronics GmbH, *Fast High Voltage Transistor Switches HTS-GSM* (2010).

[69] S. Hoekstra, J. J. Gilijamse, B. Sartakov, N. Vanhaecke, L. Scharfenberg, S. Y. T. van de Meerakker, and G. Meijer, *Optical pumping of trapped neutral molecules by blackbody radiation*, Physical Review Letters, **98**, 133001 (2007).

[70] R. Taylor and R. Phillips, *The philosophical magazine or annals of chemistry, mathematics, astronomy, natural history and general science* (1831).

[71] F. Vedel, M. Vedel, and R. E. March, *New Schemes for resonant ejection in r.f. quadrupolar ion traps*, International Journal of Mass Spectrometry and Ion Processes, **99**, 125–138 (1990).

[72] R. E. March, *Quadrupole ion traps*, Mass Spectrometry Reviews, **28**, 961–989 (2009).

[73] J. H. Blokland, *Determination of the ND₃ density in a Stark decelerated molecular beam* (2011), private communication.

[74] Pfeiffer Vacuum, *IKR251* (1999).

[75] A. T. J. B. Eppink and D. H. Parker, *Velocity map imaging of ions and electrons using electrostatic lenses: Application in photoelectron and photofragment ion imaging of molecular oxygen*, Review of Scientific Instruments, **68**, 3477–3484 (1997).

[76] A. J. de Nijs and H. L. Bethlem, *On deflection fields, weak-focusing and strong-focusing storage rings for polar molecules*, Physical Chemistry Chemical Physics, **13**, 19052–19058 (2011).

[77] J. Kalnins, G. Lambertson, and H. Gould, *Improved alternating gradient transport and focusing of neutral molecules*, Review of Scientific Instruments, **73**, 2557–2565 (2002).

[78] H. L. Bethlem, J. van Veldhoven, M. Schnell, and G. Meijer, *Trapping polar molecules in an ac trap*, Physical Review A, **74**, 063403 (2006).

Samenvatting

In dit proefschrift worden experimenten beschreven aan een synchrotron voor polaire moleculen. Sterke elektrische velden (typisch zo'n $50 \, \text{kV/cm}$) worden gebruikt om meerdere pakketjes ammoniak moleculen bij elkaar te houden terwijl zij ronddraaien in een ring. Het ultieme doel van dit onderzoek is om tegen elkaar in draaiende pakketjes met elkaar te laten botsen. Om dit doel te bereiken is het nodig om een compleet begrip te hebben van de dynamica van de moleculen in het synchrotron. Dit proefschrift laat zien dat de bewegingen van moleculen in het synchrotron in detail gestuurd en gecontroleerd kunnen worden.

Het voordeel van een synchrotron boven een opstelling die gebruik maakt van gekruiste molecuulbundels is dat pakketjes die linksom en rechtsom in het synchrotron circuleren elkaar vele malen tegenkomen. De kans op botsingen neemt hiermee toe met een factor gegeven door het product van het aantal pakketjes en het aantal rondjes dat deze pakketjes opgesloten blijven. Een botsing leidt in het algemeen tot verlies van moleculen uit de ring. Dit verlies kan worden gemeten als functie van de botsingsenergie – de relatieve snelheid van de tegen elkaar in draaiende pakketjes moleculen – wat nieuwe inzichten biedt in de fysica van koude botsingen.

In hoofdstuk 2 en 3, worden de twee Stark afremmers beschreven die gebruikt worden om de pakketjes moleculen in één quantum-toestand en met een goed gedefinieerde snelheid en snelheidsspreiding te prepareren. Alle metingen die in dit proefschrift besproken worden zijn uitgevoerd met gedeutereerd ammoniak, ND_3, maar het synchrotron kan in principe ook gebruikt worden voor andere moleculen. De twee bundellijnen zijn loodrecht op elkaar geplaatst, met de synchrotron in het kruispunt, zodat moleculen in beide richtingen in het synchrotron kunnen worden geïnjecteerd.

In hoofdstuk 4 wordt uitgelegd hoe de moleculen in het synchrotron worden opgesloten. Het synchrotron bestaat uit 40 rechte hexapolen die opgesteld staan in een cirkel met een diameter van een halve meter. De hexapolen maken een hoek van 9 graden met elkaar, met een onderlinge afstand van 2 mm. Terwijl de moleculen in het synchrotron circuleren ondervinden zij in alle richtingen een kracht die hen bij elkaar houdt. In de transversale richting wordt deze kracht geleverd door het hexapool veld. De benodigde kracht in de longitudinale richting wordt geleverd door *synchroon* met de voorwaartse beweging van de moleculen de voltages die op de hexapolen zijn aangesloten te moduleren.

In hoofdstuk 5 worden metingen getoond die laten zien hoe pakketjes ND_3 moleculen met een voorwaartse snelheid van $124{,}3 \, \text{m/s}$ langer dan 13 seconden opgesloten worden in het synchrotron. In deze tijd maken zij 1025 rondjes en passeren zij 41,000 keer de opening tussen twee hexapolen, illustratief voor de unieke stabiliteit van het synchrotron. Metingen worden getoond die de driedimensionale put karakteriseren.

In hoofdstuk 6 worden metingen getoond waarbij een externe wisselspanning wordt

gebruikt om de beweging in de driedimensionale put aan te drijven. Als de frequentie van de spanningsbron in resonantie is met de beweging van moleculen in het synchrotron resulteert dit in een afname van de stabiliteit van de banen en tot het verlies van moleculen uit het synchrotron. Het gemeten verlies als functie van de aangelegde frequentie leidt tot een beter begrip van de dynamica van de opgesloten moleculen.

In hoofdstuk 7 wordt getoond dat meerdere pakketjes moleculen tegelijkertijd kunnen worden opgesloten in het synchrotron. In totaal 26 pakketjes werden simultaan opgesloten; 13 pakketjes die linksom in het synchrotron circuleren en 13 pakketjes rechtsom. De dichtheid in deze experimenten was te klein om botsingen te observeren, echter met een nieuw ontwerp (beschreven in hoofdstuk 8) en/of andere verbeteringen, zou het mogelijk moeten zijn om botsingen waar te nemen in het synchrotron.

In conclusie, een synchrotron voor polaire molecule bestaande uit 40 rechte hexapolen is gepresenteerd, samen met een simpel maar efficiënt schakelschema om de moleculen in de longitudinale richting bij elkaar te houden. In totaal 26 pakketjes moleculen werden tegelijkertijd opgesloten in deze synchrotron; 13 pakketjes die linksom in het synchrotron ronddraaien en 13 pakketjes rechtsom. Deze metingen illustreren tot in welk detail moleculbundels kunnen worden gecontroleerd en gemanipuleerd, en zij openen nieuwe wegen voor het bestuderen van moleculen. Het synchrotron is compleet gekarakteriseerd en, met verbeteringen, klaar om gebruikt te worden als arena voor botsingen tussen koude moleculen – mogelijk opent dit een nieuw hoofdstuk in het botsingsonderzoek.

Summary

In this thesis, a synchrotron for neutral molecules was presented. High electric fields (typically around $50\,kV/cm$) were used to confine multiple packets of ammonia molecules in tight bunches along a circular path. The ultimate goal is to use the device as a novel molecular collider, requiring a full understanding of the motion of the particles inside the synchrotron. This thesis has showed how molecules are manipulated and what level of control is achieved inside the synchrotron. The advantage of a synchrotron as a collider for molecules is that clockwise and counter clockwise revolving packets would be forced to interact repeatedly. In this controlled environment the probability of bi-molecular collisions of state-selected molecules increases significantly; collisions that are difficult to detect by direct collision of two Stark-decelerated molecular beams. After a collision a molecule is – most likely – not confined anymore. This depletion can then be measured as a function of collision energy (relative velocity of the two packets) and give new insights into the research field of molecular physics.

Chapters 2 and 3 describe the two Stark decelerator beam lines that were used to manipulate and separate in space and time a beam of molecules in one single quantum state. This packet of state-selected molecules with a tunable velocity can be injected ideally into the synchrotron. All measurements were performed using deuterated ammonia, ND_3, but in general could also have been done with other Stark deceleratable molecules. The two beam lines were oriented perpendicular to each other with the synchrotron in the intersection such that counter-propagating packets can be injected. Chapter 4 explains how the control over the molecules in the synchrotron is achieved. The synchrotron consists of 40 small straight hexapole segments and has a diameter of half a meter. Each hexapole spans an angle of 9 degrees of the ring, with a constant gap of 2 mm between adjacent hexapoles. As the confined molecular packet revolves inside the synchrotron it is confined in a three dimensional moving trap. In the transverse direction the molecules are pushed towards the molecular beam axis by the hexapole field. By switching the electric field 'synchronously' with the motion of the molecular packet to a higher electric potential, the molecular packet experiences an additional longitudinal force. The force is caused by the fringe fields of the electric potential in the gap region. By this means, the longitudinal spreading out of the molecular packet is countered and a three dimensional potential well is achieved.

The level of control over polar molecules that can be achieved using electric fields is exemplified in Chapter 5 where a packet of neutral polar ND_3 molecules with a forward velocity of $124.3\,m/s$ is confined inside this synchrotron for over 13 seconds. At this point the ammonia molecules revolved over 1000 round trips and have then passed 41,000 times through a gap, remaining confined in a compact packet throughout. This explicitly demonstrates the overall stability of the molecular synchrotron. The three dimensional

potential well is completely characterized using a variety of different experiments. A different approach to describe the potential well is shown in Chapter 6, where the motion of the molecules inside the synchrotron is resonantly excited with an additional sinusoidal force. This excitation led to a depletion of molecules at certain characteristic resonant frequencies. This frequency dependent pattern gives a new insight into how the molecules are confined in the synchrotron. The ability to store multiple counter-propagating revolving packets inside the synchrotron is shown in Chapter 7. In total 26 packets are simultaneously confined: 13 packets of molecules revolving clockwise and 13 packets of molecules revolving counter-clockwise, each in a tight packet. The density of the ammonia molecule is not sufficient to detect in a prototype experiment the effect of bi-molecular collisions. With a new design (described in Chapter 8) and other improvements, the effect of bi-molecular collisions is in close range.

In conclusion, a synchrotron for neutral molecules consisting of 40 straight hexapoles together with a simple bunching scheme is presented. Up to 26 counter-propagating packets of ammonia molecules, 13 packets of molecules stored clockwise and 13 packets counter-clockwise, have simultaneously been stored in this structure. These measurements epitomize the level of control that can now be achieved over molecular beams and sets the stage for novel experiments to come. This synchrotron was completely analyzed and, with further improvements, is ready to determine collisions of state-selected molecules as a function of collision energy – potentially opening a new Chapter in collision studies of molecules.

Acknowledgments

Normally, when you have a thesis for the first time in front of you, you have a glance on the cover before you thumb through the book in the search of interesting figures. Before you put the thesis away you usually stop at the *Acknowledgments*. If you know the author personally, you are interested if he/she acknowledged, or at least mentioned, you. If you do not know him/her personally, the *Acknowledgments* can give you a non-scientific and private perspective on the author. In these last pages of my thesis, I want to use the opportunity to thank the people who were directly involved in the project of the molecular synchrotron and those who made my last years at the Fritz-Haber-Institut special and enjoyable.

Zuallererst möchte ich mich bei meinem Doktorvater Gerard Meijer bedanken. Gerard, vielen Dank, dass du mir das Vertrauen entgegengebracht hast, das Projekt des molekularen Synchrotrons zu übernehmen. Durch deine eigene Begeisterung an dem Projekt und deine Leitung in der Abteilung hast du für mich eine exzellente wissenschaftliche Umgebung geschaffen, in der ich gern täglich gearbeitet habe. Weiterhin möchte ich mich bei meinem wissenschaftlichen Betreuer (Co-Promotor) Rick Bethlem bedanken! Rick, trotz der räumlichen Distanz zwischen Amsterdam und Berlin hast du eine angenehme und erfolgreiche Betreuung der Doktorarbeit erreicht. Vielen Dank dafür! Vor allem in der finalen Phase der Doktorarbeit hast du mich durch das viele Korrekturlesen sehr unterstützt. Ebenfalls möchte ich mich bei Bas van de Meerakker, meinem zweitem wissenschaftlichen Betreuer (Co-Promotor), bedanken, bei dem ich bereits als Diplomand eine gute Betreuung genießen durfte. Bas, vielen Dank, dass du gerade in der Anfangszeit die direkte Betreuung übernommen hast und mir bei den vielen täglichen Laborproblemen stets motiviert und kreativ zu Hilfe standest. Allen dreien sei nochmals herzlich für die rechte Mischung aus unabhängigem wissenschaftlichen Arbeiten und einer guten Betreuung gedankt! The members of the manuscript committee, David Parker, Andreas Osterwalder, and Nicolas Vanhaecke, I would like to thank for carefully reading the manuscript and their helpful comments.

Meiner Vorgängerin Cynthia Heiner möchte ich für ihre Hilfe während meiner Anfangszeit als Doktorand und für ihre Doktorarbeit danken. Deine *rote* Bibel war unersetzlich und war stets – in ständiger Benutzung – aufgeschlagen neben meinem Laborbuch zu finden. In meinem letzten Jahr am Fritz-Haber-Institut hatte ich das Vergnügen mit Chris Eyles zusammenzuarbeiten. Chris, it was a real pleasure working with you! I just want to say that your scientific skills and your cheerful nature were highly appreciated (especially the proof-reading skills). Thanks a lot! I also wish my successor, Aernout van der Poel, all the best for his thesis. I am sure, you will use the synchrotron (which is

now located at the Vrije Universiteit Amsterdam, the Netherlands) to make beautiful experiments.

Auch von technischer Seite habe ich viel Unterstützung von Kollegen erhalten, bei denen ich mich nun bedanken will. Ein ganz besonderer Dank gebührt André van Roij für das Design und den Aufbau des molekularen Synchrotrons sowie den beiden Stark-Abbremsern. André, deine Hingabe und die nötige Präzision haben die Realisierung des Synchrotrons ermöglicht. Für Unterstützung bei elektronischen Fragestellungen bedanke ich mich bei den engagierten Mitarbeitern des Elektroniklabors des Fritz-Haber-Instituts. Speziell erwähnt seien Torsten Vetter, Viktor Platschkowski und Georg Heine. Es war sehr schön zu wissen, dass man bei jeglichen elektronischen Problemen eine kompetente Anlaufstation hatte. Vielen Dank auch an die Feinwerktechnik unter der Leitung von Herrn Schwäricke. Ebenfalls möchte ich mich bei Sandy Gewinner für die Hilfe bei Laserproblemen aller Art bedanken. Uwe Hoppe danke ich für die Programmierung von KouDA und für die Implementierung der Extraprogramme, die den Messverlauf sehr erleichtert haben. Bei den kleinen mechanischen Problemen konnte man Georg Hammer, Petrick Bischoff und Manfred Erdmann ansprechen, die mir stets ohne Verzug weitergeholfen haben. Vielen Dank dafür!

Auch bei den Kollegen, die nicht direkt in mein Projekt involviert waren, möchte ich mich herzlichst bedanken. Gern würde ich alle Kollegen aus der Abteilung und bei jedem eine lustige Anekdote aufzählen, die das gute Gesamtklima exemplarisch beschreibt. Hier beschränke ich mich jedoch auf einige wenige: Speziell erwähnt seien Andrea Braaker und Inga von Dölln für ihr permanentes Engagement für ein gutes Arbeitsklima. Mit vielen Mitdoktoranden und Postdocs hatte ich eine tolle und spannende Zeit. Meinen Bürokollegen Fabian Grätz, Christian Schewe, Frank Filsinger, Dagmar Kreikemeyer und Philipp Grüne sowie meinen Laborkollegen Stephan Putzke, Janneke Blokland, Marko Härtelt und Isabel Gonzalez Florez danke ich besonders für das gesellige Miteinander und die entspannte Atmosphäre. Auch hier will ich eine kleine Laboranekdote in die Danksagung einfügen: Der für mich bedeutendste Tag meiner Doktorarbeit war wohl im März 2009. Mehrere Monate hatte ich verzweifelt versucht der Ursache auf den Grund zu kommen, warum die Moleküle im Synchrotron nicht gespeichert werden können, sondern immer schon nach wenigen Umdrehungen verloren gehen. Stephan Putzke, mein direkter Labornachbar, war ebenfalls seit mehreren Monaten darum bemüht, drei Peaks in seinen Flugzeitprofilen zu entdecken, die für die AG-Abbremsung für Benzonitril stehen sollten. Als wir so vor uns hin optimierten, erhielt ich auf einmal das Signal, das Stephan eigentlich sehen wollte: Drei Peaks in meiner Flugzeitmessung. Das erste Anzeichen für das stabile Bunching im Synchrotron und es fiel mir ein Stein vom Herzen.

Schöne Momente habe ich während der letzten Jahre nicht nur in der Experimentierhalle erfahren, sondern auch in dem kleinen Seminarraum. Dort wurde während der Mittagspause an einem Kicker hart aber freundlich um den Sieg gekämpft. Dass bei einer Niederlage ohne eigenem Tor unter dem Kickertisch hindurch gekrabbelt werden musste, hat bei allen Teilnehmern den nötigen Ehrgeiz erzeugt gut zu spielen. Allen Teilnehmern

sei herzlich für die schöne gemeinsame Zeit gedankt.

 Auch meiner Familie, meiner Freundin Katrin und meinen Freunden danke ich! Durch euch schöpft man Freude und Kraft!

Amsterdam, im Oktober 2012

Peter Zieger
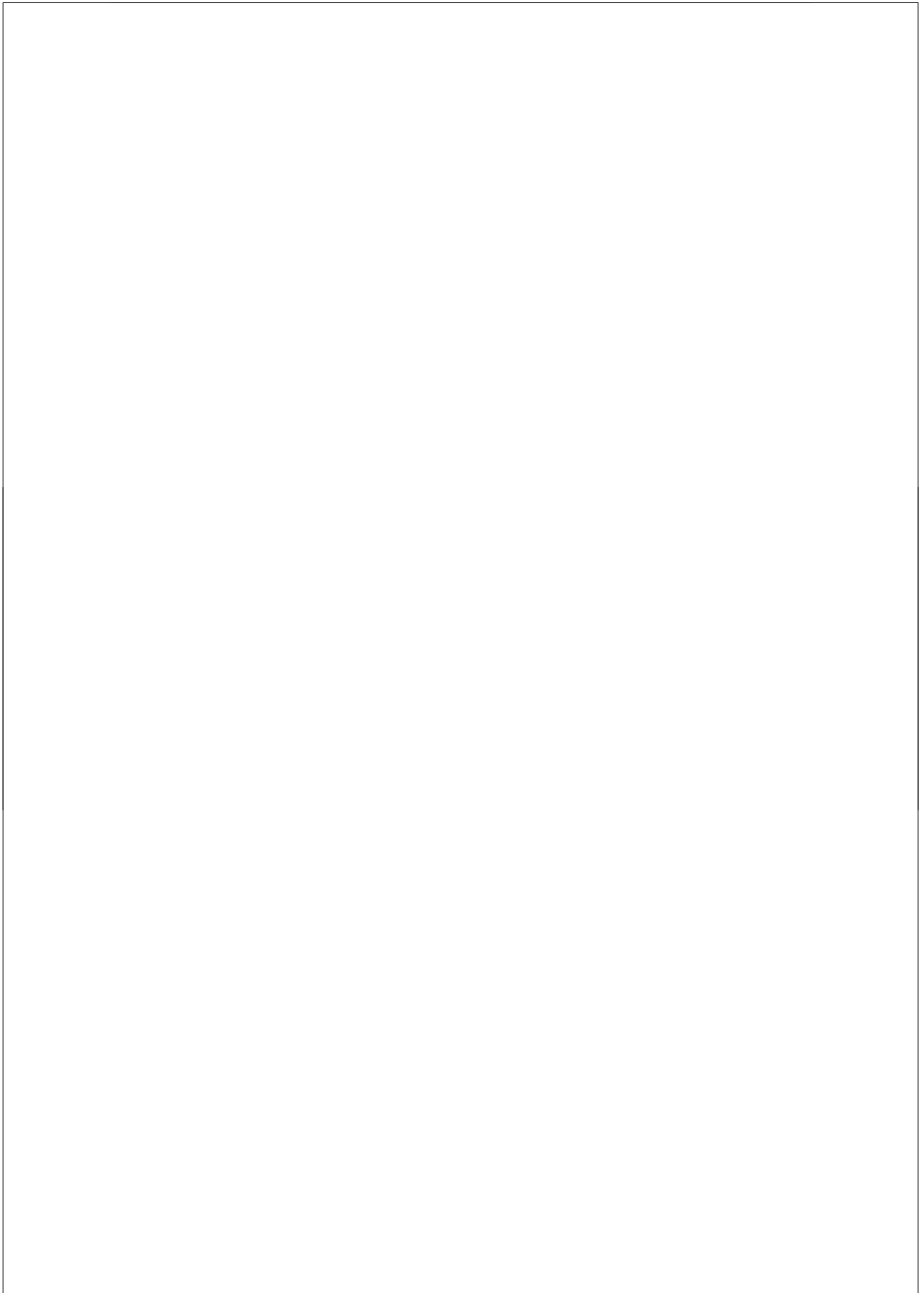
Curriculum Vitae

Peter Christian Zieger
Born April 4th, 1982 in Leipzig, Germany

2001   Abitur at the Georg-Büchner-Oberschule, Berlin, Germany

2001 − 2003   Studies of physics at the Freie Universität Berlin, Berlin, Germany

2003 − 2004   Erasmus scholar at the Università di Bologna, Bologna, Italy

2004 − 2008   Studies of physics at the Freie Universität Berlin, Berlin, Germany

2006 − 2007   Research for the diploma thesis under the supervision of Prof. Dr. Gerard J. M. Meijer at the Department of Experimental Physics at the Freie Universität Berlin, Berlin, Germany.

                Subject of diploma thesis: *Production and Focusing of Metastable NH Radicals*

2008 − 2012   PhD student in the group of Prof. Dr. Gerard J. M. Meijer at the Fritz-Haber-Institut der Max-Planck-Gesellschaft, Berlin, Germany

                Subject of PhD thesis: *A Synchrotron for Polar Molecules*